

Biaxial Tension Testing of 8-in. (200-mm) Diameter TR-XTREME™ Ductile Iron pipe

Shih-Hung Chiu

Qinglai Zhang

Shakhzod Takhirov

Kenichi Soga



Berkeley
CENTER FOR
Smart Infrastructure

CSI Report 2023/01
Center for Smart Infrastructure (CSI)
Department of Civil and Environmental Engineering
University of California, Berkeley May 2023

EXECUTIVE SUMMARY

This report describes the experimental and numerical results of the biaxial tension tests (combined bending and tension force) performed on 8-inch diameter TR-XTREME™ ductile iron pipe manufactured by U.S. Pipe. The purpose of the testing is to evaluate the load capacity, joint opening characteristics, and the failure mechanism of the TR-XTREME™ restrained joint under biaxial tension force, which is designed to be used in areas of seismic activity. The two biaxial tension tests were performed for different orientations of the locking segments at the bell joint connection. The data obtained from distributed fiber optic sensors are used to validate the three-dimensional (3D) finite element (FE) model. The model can be used as a reference model for future related pipeline tests and optimizing pipeline design and installation.

Keywords: *Ductile iron pipe, water pipelines, biaxial tension, fiber optic, finite element analysis.*

ACKNOWLEDGMENTS

The East Bay Municipal Utility District (EBMUD) provided the funding for this project, and U.S. Pipe supplied the pipes used for the experiment. Completing the work would not be possible without the support of Llyr Griffith, John Kochan, and Phillip Wong of the University of California, Berkeley. Active involvement and guidance from Jeff Mason of U.S. Pipe and David Katzev of EBMUD are greatly appreciated.

DISCLAIMER

Any opinions, findings, conclusions, or recommendations expressed in this report are those of the author(s) and do not necessarily reflect those of the University of California, Berkeley.

CONTENTS

EXECUTIVE SUMMARY	II
ACKNOWLEDGMENTS.....	III
DISCLAIMER.....	IV
CONTENTS	V
LIST OF FIGURES	VII
LIST OF TABLES	IX
1. Introduction.....	10
2. Test Setup	13
2.1 Experimental Setup	13
2.2 Specimen List	14
2.3 Test Procedure.....	15
3. Instrumentation	16
3.1 Conventional Instruments	16
3.2 Distributed Fiber Optic Sensors.....	18
4. Test Results.....	21
4.1 Calculation Approach.....	21
4.2 Experimental Data Analysis.....	21
4.2.1 Joint Moment and Deflection.....	22
4.2.2 Axial Force and Joint Opening	23
4.2.3 Axial Strains.....	24
4.2.4 Hoop Strains.....	31
4.3 Failure Modes.....	37
5. Finite Element Analysis	39
5.1 Overview of Numerical Model	39
5.2 Determination of Pipe Parameters.....	40
5.3 Overview of FEM Results	40
5.3.1 Push down stage.....	40
5.3.2 Pull stage.....	41
5.3.3 Failure mechanism	43
5.4 FEM Results of Specimen 1	45
5.4.1 Overview.....	45
5.4.2 Bell Deformation.....	47
5.4.3 Spigot Deformation	48
5.4.4 Strain Comparison between FE Analysis and Experimental Results.....	48
5.5 FEM Results of Specimen 2	51

5.5.1	Overview	51
5.5.2	Bell Deformation.....	52
5.5.3	Strain Comparison between FE Analysis and Experimental Results.....	53
6.	<i>Conclusion.....</i>	56
7.	<i>Reference.....</i>	57
	<i>Appendix A: Distributed Fiber Optic Sensing.....</i>	58
	<i>Appendix B: Distributed Fiber Optic Sensors Result</i>	60
(a)	Specimen 1	60
(b)	Specimen 2.....	66
	<i>Appendix C: Comparison of FEM simulation results and experimental results</i>	72
(c)	Specimen 1	72
(d)	Specimen 2.....	74

LIST OF FIGURES

Figure 1-1 Mechanism of TR-XTREME™ joint (U.S. Pipe, 2020)	10
Figure 1-2 Recommended installation positions (U.S. Pipe, 2020).....	11
Figure 1-3 Sketch of testing setup and procedure.....	12
Figure 1-4 Cross-section of the joint regarding each stage.....	12
Figure 2-1 Sketch of the experimental setup	13
Figure 2-2 Overview of the experimental setup	14
Figure 2-3 Orientation of locking segments	14
Figure 3-1 Instrumentation plan of conventional instruments	17
Figure 3-2 DFOS instrumentation plan.....	19
Figure 4-1 Moment vs. Rotation (Deflection angle).....	22
Figure 4-2 Sketch of the bell after Push Down stage.....	23
Figure 4-3 Axial force vs. average joint opening	24
Figure 4-4 Stress distribution of the cross-section of the bell under the Pull stage.....	24
Figure 4-5 Axial strain vs. rotation (defelction) of Specimen 1	25
Figure 4-6 Axial strain vs. rotation (deflection) of Specimen 2	26
Figure 4-7 Strain development of bell pipe in the longitudinal direction under 8.36-degree deflection. (a) Specimen 1; (b) Specimen 2.....	27
Figure 4-8 Strain development of spigot in the longitudinal direction under 8.36-degree deflection condition. (a) Specimen 1; (b) Specimen 2.....	28
Figure 4-9 Strain development of bell pipe in longitudinal direction under 140 kips axial force loading condition. (a) Specimen 1; (b) Specimen 2.....	30
Figure 4-10 Strain development of spigot in longitudinal direction under 140 kips axial force loading condition. (a) Specimen 1; (b) Specimen 2.....	31
Figure 4-11 Hoop strain vs. rotation of Specimen 1	32
Figure 4-12 Hoop strain vs. the rotation of Specimen 2	32
Figure 4-13 Strain distribution in the circumferential direction of Specimen 1 under 8.3-degree deflection condition. (a) sensor on the bell pipe (b) sensor at the mid location of the bell (c) sensor on top of the locking segments on the bell (d) sensor on the spigot.....	33
Figure 4-14 Strain distribution in circumferential direction under Specimen 2 under 8.3-degree deflection condition. (a) sensor on the bell pipe (b) sensor at the mid location of the bell (c) sensor on top of the locking segments on the bell (d) sensor on the spigot.....	34
Figure 4-15 Joint deformed mechanism in Push Down stage.....	35
Figure 4-16 Strain distribution in the circumferential direction of Specimen 1 under 140 kips loading condition. (a) sensor on the bell pipe (b) sensor at the mid location of the bell (c) sensor on top of the locking segments on the bell (d) sensor on the spigot.....	36
Figure 4-17 Strain distribution in the circumferential direction of Specimen 2 under 140 kips loading condition. (a) sensor on the bell pipe (b) sensor at the mid location of the bell (c) sensor on top of the locking segments on the bell (d) sensor on the spigot.....	37
Figure 4-18 Failure of Bell of Specimen 1 (left) and 2 (right)	38
Figure 5-1 3-D FE model mesh for biaxial tension condition	39
Figure 5-2 Initial position of the bell and spigot.....	40
Figure 5-3 Bending moment vs. joint deflection	41
Figure 5-4 Push down stage.....	41
Figure 5-5 Axial force vs. average joint opening	42

Figure 5-6 Stress distribution of bell-spigot joint	43
Figure 5-7 Failure mode – Specimen 1	43
Figure 5-8 Failure mechanism – Specimen 1	44
Figure 5-9 Failure mode – Specimen 2.....	45
Figure 5-10 Plastic strain distribution– Specimen 2.....	45
Figure 5-11 Axial force vs. average joint opening – Specimen 1.....	46
Figure 5-12 The stress contours of the deformed joint at push down stage – Specimen 1.....	46
Figure 5-13 The stress contours of the deformed joint at pull stage – Specimen 1.....	47
Figure 5-14 The stress contours of bell cross-section: (a) initial stage (b) push down stage (c) pull stage- Specimen 1	47
Figure 5-15 The stress contours of spigot cross-section: (a) initial stage (b) push down stage (c) pull stage – Specimen 1	48
Figure 5-16 The deformation of the weld bead – Specimen 1.....	48
Figure 5-17 Comparison of hoop strains (a) Actuator push down (b) Pull to 2.2 inches – Specimen 1.....	49
Figure 5-18 Comparison of axial strains (a) Actuator push down (b) Pull to 2.2 inches – Specimen 1.....	50
Figure 5-19 Hoop stress at push down stage and pull stage – Specimen 1	51
Figure 5-20 Axial force vs. average joint opening – Specimen 2.....	51
Figure 5-21 The stress contours of the deformed joint at push down stage – Specimen 2.....	52
Figure 5-22 The stress contours of the deformed joint at pull stage – Specimen 2.....	52
Figure 5-23 The stress contours of bell cross-section: (a) initial stage (b) push down stage (c) pull stage – Specimen 2.....	53
Figure 5-24 Comparison of hoop strains (a) actuator push down (b) pull to 2.2 inches – Specimen 2.....	54
Figure 5-25 Comparison of axial strains (a) actuator push down (b) pull to 2.2 inches – Specimen 2.....	55
Figure 5-26 Hoop stress at push down stage and pull stage – Specimen 2	55

LIST OF TABLES

Table 2-1 Test log	15
Table 2-2 Testing procedure	15
Table 3-1 Conventional instrumentation local names	17
Table 3-2 Schematic illustration of the selected strain sensor cable (Wu et al., 2015)	18
Table 3-3 DFOS local names	20
Table 3-4 Location of longitudinal fiber optic cables.....	20
Table 4-1 Summary of the tests	23
Table 5-1 Ductile Iron Pipe properties.....	40

1. Introduction

This report summarizes the experimental and finite element (FE) modeling results of the biaxial tension tests performed on 8-inch diameter TR-XTREME™ earthquake-resistant ductile iron pipe specimens manufactured by U.S. Pipe. The pipe is designed to maintain full water service after seismic events to achieve the seismic resiliency of the pipeline systems. The pipe is equipped with a single-restrained bell joint connection, providing 2.9-inch extension capability and 5-degree deflection contraction capacity. The schematic of the bell joint is shown in Figure 1-1. The spigot is designed to be inserted into the bell, passing through a water-prevent rubber gasket, and is equipped with a weld bead to bear against the locking segments, used as a locking mechanism while pulling. The single slot is used for holding the locking segments. Three white stripes on the spigot are used to indicate the installation position. The manufacturer recommends three installation positions: collapsed, midpoint, and extended location, as shown in Figure 1-2. The Option-B-Midpoint installation was used as the start position of the experiments.

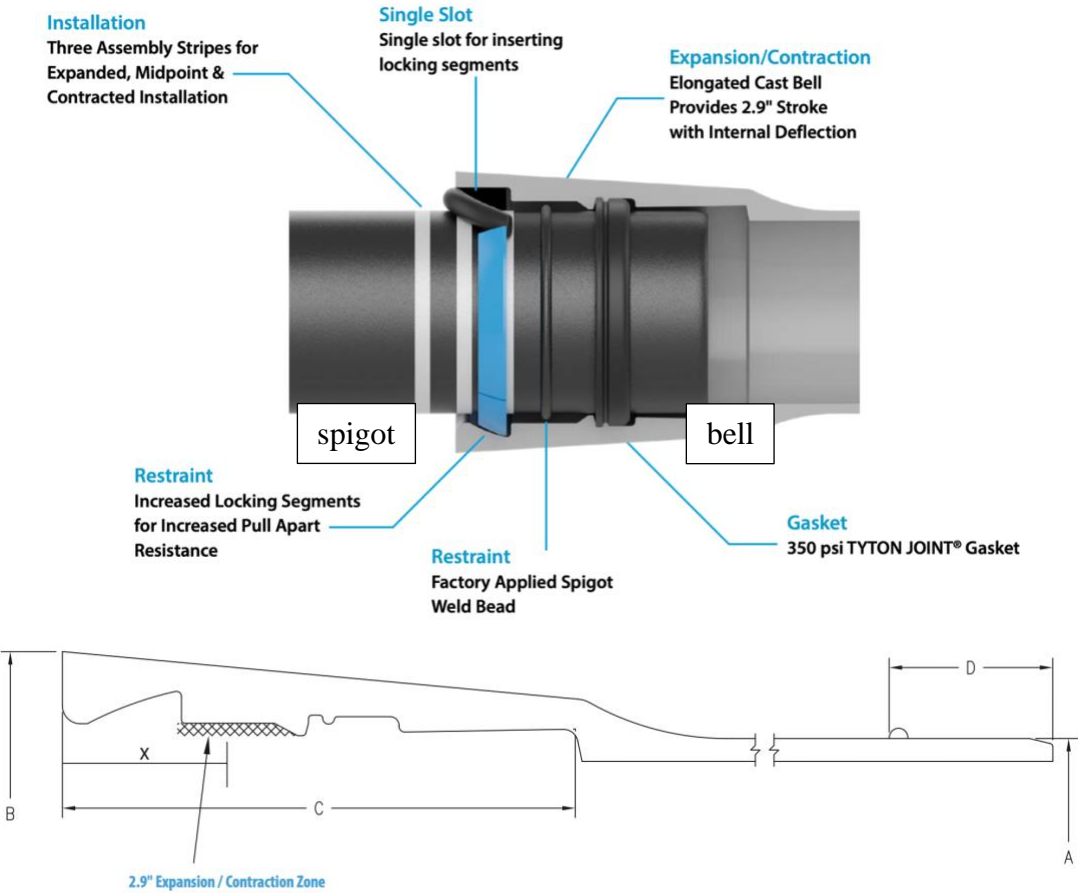
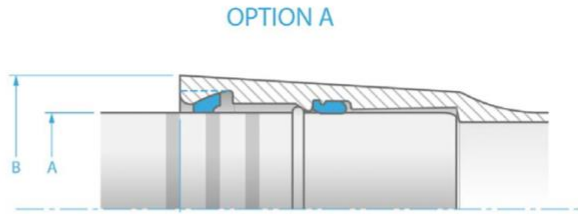
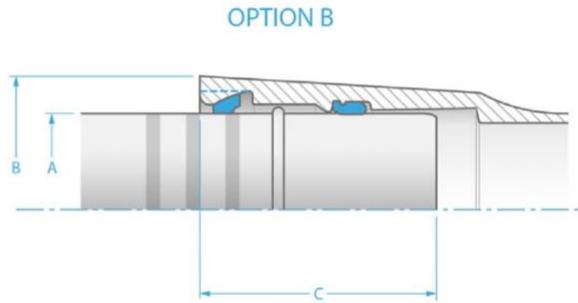


Figure 1-1 Mechanism of TR-XTREME™ joint (U.S. Pipe, 2020)

Option A-Collapsed – Correct assembly is determined when the front edge of the assembly stripe furthest from the spigot tip lines up with the face of the pipe bell as viewed from above, leaving only one assembly stripe shown.



Option B-Midpoint – Correct assembly is determined when the front edge of the middle assembly stripe lines up with the face of the pipe bell as viewed from above, leaving two assembly stripes shown.



Option C-Extended (Restrained) - Correct assembly is determined when the front edge of the assembly stripe closest to the spigot tip lines up with the face of the pipe bell as viewed from above, leaving three assembly stripes shown. This is the proper assembly when immediate joint restraint is required.

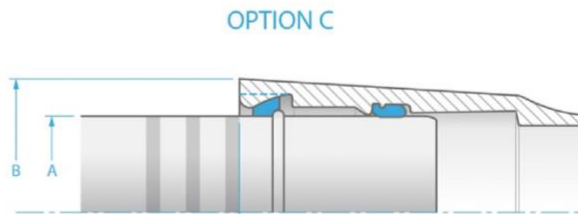


Figure 1-2 Recommended installation positions (U.S. Pipe, 2020)

Two 8-inch diameter TR-XTREME™ pipes with two different orientations of locking segments (the single slot located at 9 o'clock and 12 o'clock, respectively) were used for the biaxial tension tests. A vertical force was first applied to the pipes to push them to an 8-degree deflection contraction. Then, a axial force was applied in tension until severe pipe damage or water leakage occurred, as shown in Figure 1-3. Figure 1-4 is the cross-section of the joint that demonstrates the behavior of the bell and spigot regarding each stage. The testing objectives are (1) to evaluate the mechanical behavior and capacity of the pipe under combined bending and tension forces and (2) to discuss the effect of the different locking segments' locations on the joint performance.

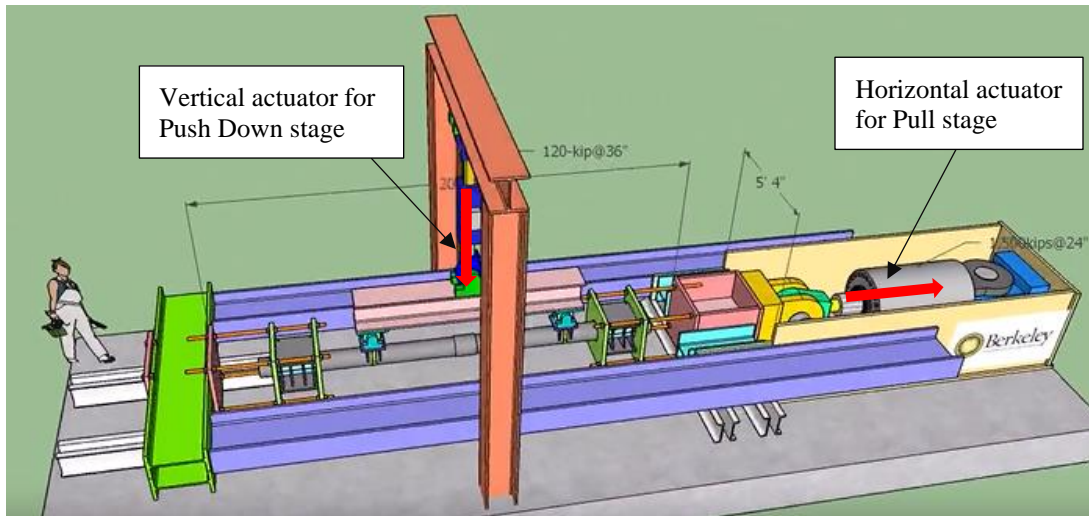
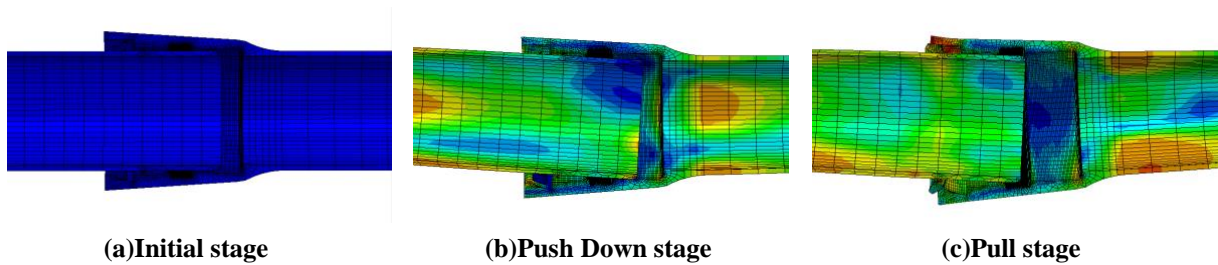


Figure 1-3 Sketch of testing setup and procedure



(a)Initial stage

(b)Push Down stage

(c)Pull stage

Figure 1-4 Cross-section of the joint regarding each stage

In this study, distributed fiber optic sensors (DFOS) were utilized to measure the continuous strain development of the pipeline in the longitudinal and circumferential directions to understand the actual deformation of the jointed pipes under combined bending and tension forces. A series of FE analysis was conducted to simulate the behavior of the pipes by utilizing an elastoplastic material model in ABAQUS ([ABAQUS 2020](#)). The data from DFOS were then used to validate the predicted results from the FE models. The validated FE models can be used for future parametric studies for improved pipe design, if necessary.

2. Test Setup

2.1 Experimental Setup

The experimental setup was developed at the Center for Smart Infrastructure (CSI) at UC Berkeley. The sketch of the entire setup is shown in Figure 2-1. The overview of the actual fully assembled setup of the biaxial tension test is shown in Figure 2-2. Two special jackets were designed and manufactured to hold the pipeline ends in place. Two hydraulic actuators with a capacity of 1,500 kips at 24-inch displacement were used for the experiments. One of the actuators was connected to the jacket at the spigot end for tensile force application purposes. The other actuator was used to apply vertical loads. The actuator applied a force on the steel spreader beam, and the beam transferred the force to the bell pipe and spigot via two loading saddles placed on the pipes.

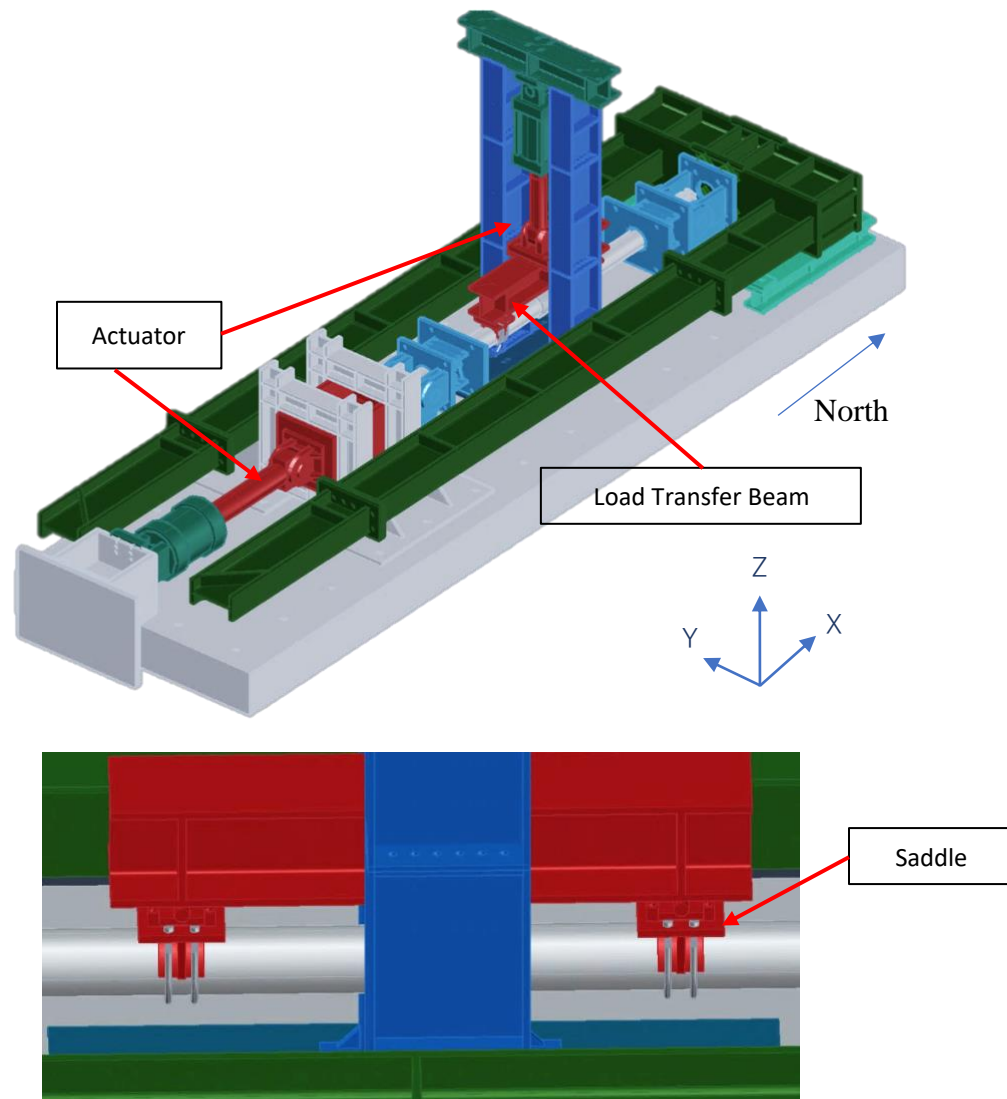


Figure 2-1 Sketch of the experimental setup

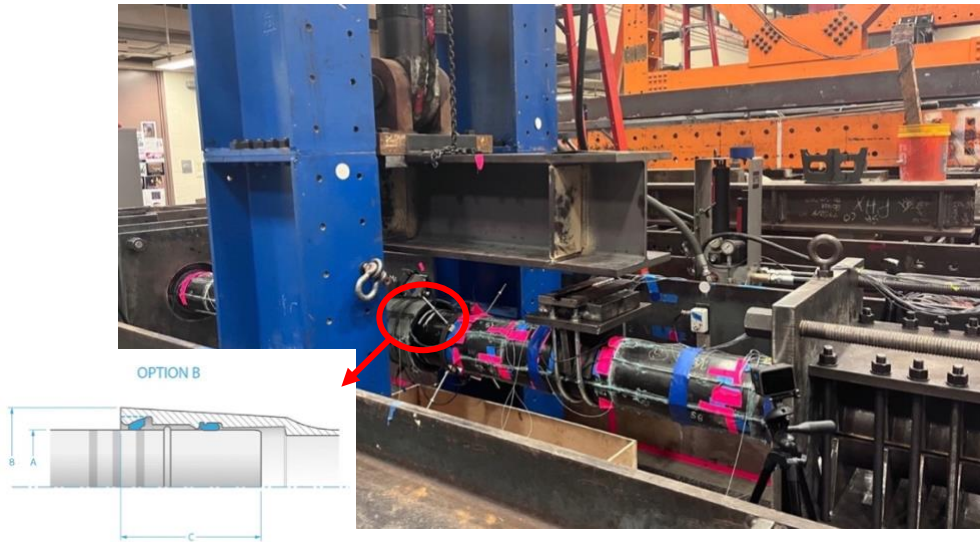


Figure 2-2 Overview of the experimental setup

The 8-inch diameter TR-XTREME™ pipes used in the experiments were manufactured by U.S. Pipe. Three assembly locations were recommended by the manufacturer, collapsed, midpoint, and extended. The midpoint location (i.e., two white stripes on the spigot are visible) was used as the initial location for the experiments, meaning that the locking segments were not in contact with the weld bead on the spigot, and the spigot was allowed to slide in and out of the bell under vertical loading conditions.

2.2 Specimen List

Two biaxial tension tests were conducted with the same experimental setup but different orientations of the locking segments, as shown in Figure 2-3. For the first test, the single slot was located in the 9 o'clock direction (i.e., at the west side), where the three pieces of the locking segments were placed at the top, east, and bottom sides, respectively. For the second test, the single slot was rotated in the 12 o'clock direction (i.e., at the top side), where the corresponding locking segment locations are west, east, and bottom sides. A rubber gasket was palced at the single slot for both of the specimens. The test log is presented in Table 3-2.

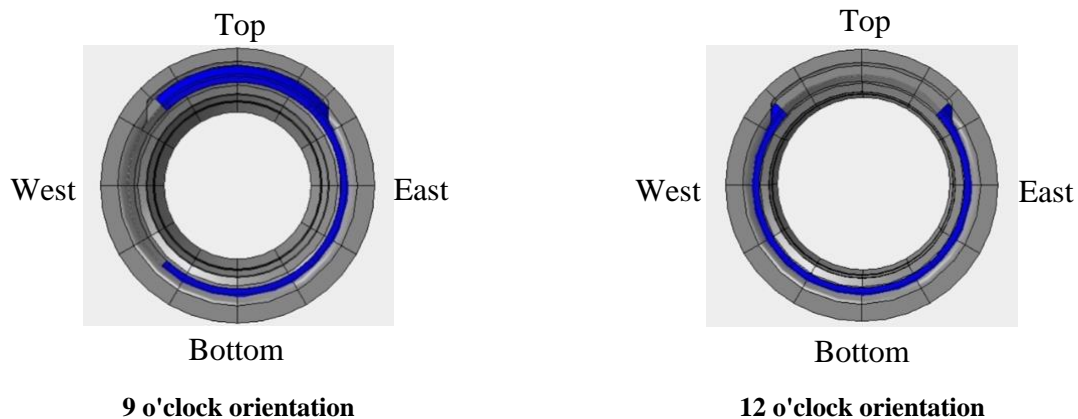


Figure 2-3 Orientation of locking segments

Table 2-1 Test log

Test No	Specimen	Test date	Locking segments orientation
1	Specimen 1	9/01/2022	9 o'clock
2	Specimen 2	9/28/2022	12 o'clock

2.3 Test Procedure

The testing procedure included four stages; (i) Self-Weight Moving Down, (ii) Actuator Pushing Down, (iii) Water Pressurization, and (iv) Pull. The loading and boundary conditions varied from each stage. During the first stage (self-weight moving down), the bell-pipe side was restrained only to allow z-direction rotation (i.e., perpendicular to the floor); however, axial movement and z-direction deflection were allowed on the spigot side, meaning that the spigot could slide in and out of the bell. The horizontal actuator was not connected to the hydraulic system, and no external forces were applied during this stage. The bell was moving down due to the self-weight of the pipes, which introduced deflections to the specimen. Once the system achieved static force equilibrium, the actuator was pinned to the hydraulic system to restrain the spigot from further horizontal movement.

Then, a vertical force was applied to further push down the bell until reaching an 8-degree deflection (4 degrees on both ends). The vertical actuator applied the force to the loading beam, and the loading beam transferred the load to the pipelines via the loading saddles. The saddles were placed 33.5 inches away from the mid-point, where the mid-point of the setup was defined to be 3.25 inches away from the bell face. Next, the internal water was pressurized to 50 psi.

Finally, the spigot were pulled until severe pipe damage and water leakage was observed. The vertical actuator was held to restrain the pipeline from moving upward but allowed it to move downward during the pulling stage.

The entire procedure of the testing is summarized in Table 2-2.

Table 2-2 Testing procedure

Test procedure	Loading condition	Boundary condition
Self-weight moving down	Gravity force	Allow z-direction deflection on both ends and x-direction movement on the spigot end.
Actuator pushing down	Vertical actuator force	Allow z-direction deflection on both ends.
Water pressurization	Internal water pressure	Allow z-direction deflection on both ends. Restrain the bell from moving upward.
Pull	Horizontal axial force	Allow z-direction deflection on both ends. Restrain the bell from moving upward.

3. Instrumentation

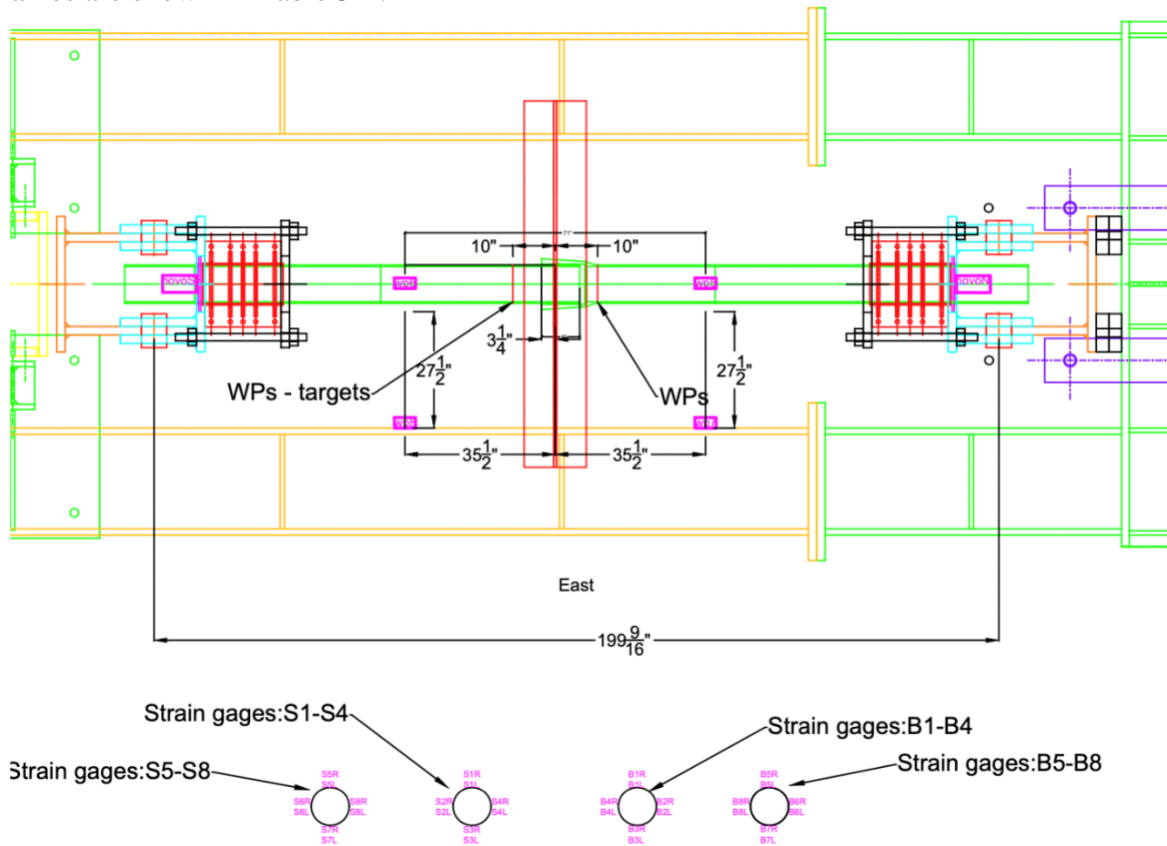
The instrumentation consisted of conventional instruments (strain gauges, string pots) and distributed fiber optic sensors.

3.1 Conventional Instruments

Four strain gauges plane were used; two on the bell pipe and another two on the spigot. Each strain gauge plane consisted of four strain gauge sets. Strain gauge sets were placed at the position of the top, west, bottom, and east sides (i.e., 12, 3, 6, 9 o'clock) on the bell pipe and spigot. Each set of strain gauges included two strain gauges in the perpendicular directions measuring axial and circumferential strains.

Four wire pots were placed on the bell pipe at 45 degrees apart from the quarter points around the circumference and were fixed to the spigot to measure the joint opening. Another four wire pots were used to measure the pipe displacement during the experiment. They were individually mounted to the bell pipe and spigot on the east and bottom sides. The wire pots installed on the bottom sides were used to monitor the vertical displacement, and the ones on the east side aimed to measure the horizontal movement.

The locations of the instruments are shown in Figure 3-1, and the local instrumentation names are shown in Table 3-1.



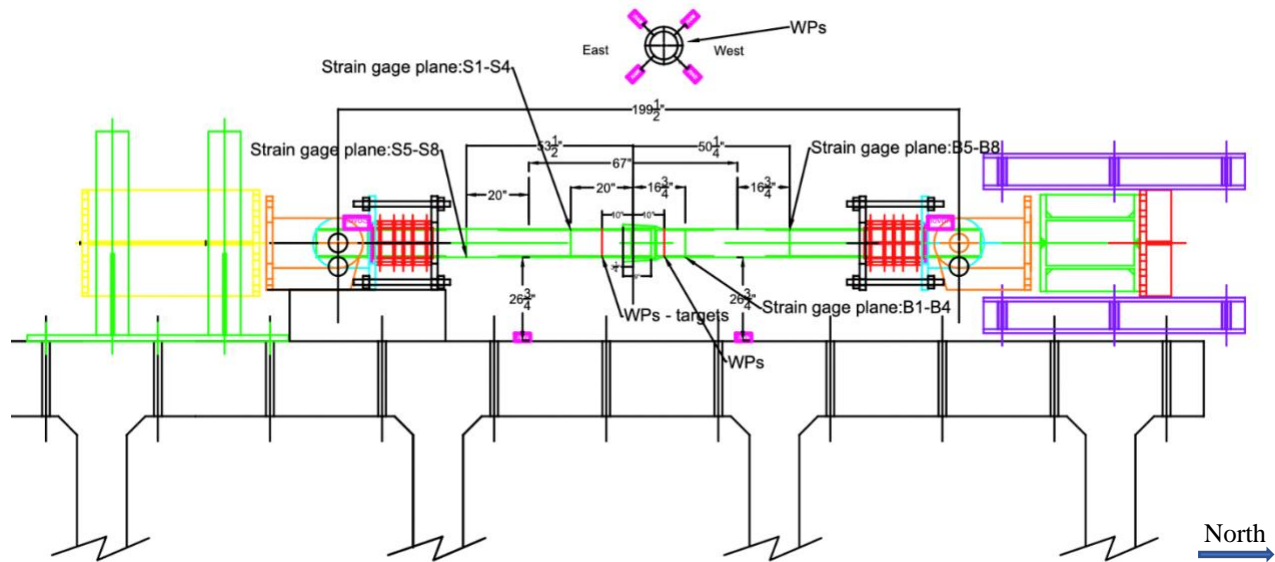


Figure 3-1 Instrumentation plan of conventional instruments

Table 3-1 Conventional instrumentation local names


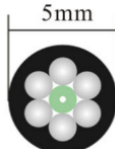
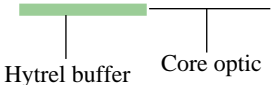
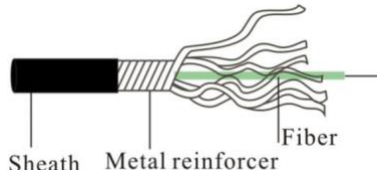
Instrument	Location	Local Instrument Name
String Pot	Parallel to Axial Direction, North of Bell, Top-west	wp1
	Parallel to Axial Direction, North of Bell, West-bottom	wp4
	Parallel to Axial Direction, North of Bell, Bottom-east	wp2
	Parallel to Axial Direction, North of Bell, East-top	wp3
	Perpendicular to Axial Direction, North of Bell, Bottom	wp5
	Perpendicular to Axial Direction, North of Bell, East	wp7
	Perpendicular to Axial Direction, South of Bell, Bottom	wp6
	Perpendicular to Axial Direction, South of Bell, East	wp8
Strain Gauge	Top of Bell-side Pipe (North), Axial Strain	B5L
	West of Bell-side Pipe (North), Axial Strain	B8L
	Bottom of Bell-side Pipe (North), Axial Strain	B7L
	East of Bell-side Pipe (North), Axial Strain	B6L
	Top of Spigot (North), Axial Strain	S1L
	East of Spigot (North), Axial Strain	S2L
	Bottom of Spigot (North), Axial Strain	S3L
	West of Spigot (North), Axial Strain	S4L
	Top of Bell-side Pipe (North), Circumferential Strain	B5R
	West of Bell-side Pipe (North), Circumferential Strain	B8R
	Bottom of Bell-side Pipe (North), Circumferential Strain	B7R
	East of Bell-side Pipe (North), Circumferential Strain	B6R
	Top of Spigot (North), Circumferential Strain	S1R
	East of Spigot (North), Circumferential Strain	S2R
	Bottom of Spigot (North), Circumferential Strain	S3R
	West of Spigot (North), Circumferential Strain	S4R
	Top of Bell-side Pipe (South), Axial Strain	B1L
West of Bell-side Pipe (South), Axial Strain	B2L	
Bottom of Bell-side Pipe (South), Axial Strain	B3L	

	East of Bell-side Pipe (South), Axial Strain	B4L
	Top of Spigot (South), Axial Strain	S5L
	East of Spigot (South), Axial Strain	S6L
	Bottom of Spigot (South), Axial Strain	S7L
	West of Spigot (South), Axial Strain	S8L
	Top of Bell-side Pipe (South), Circumferential Strain	B1R
	West of Bell-side Pipe (South), Circumferential Strain	B2R
	Bottom of Bell-side Pipe (South), Circumferential Strain	B3R
	East of Bell-side Pipe (South), Circumferential Strain	B4R
	Top of Spigot (South), Circumferential Strain	S5R
	East of Spigot (South), Circumferential Strain	S6R
	Bottom of Spigot (South), Circumferential Strain	S7R
	West of Spigot (South), Circumferential Strain	S8R

3.2 Distributed Fiber Optic Sensors

Two types of fiber optic cables manufactured by NanZee Sensing Technology Co. were used as shown in Table 3-2; (a) 5 mm diameter armored cable (NanZee 5mm) and (b) 0.9 mm diameter cable (NanZee 0.9mm). The local instrument names are listed in Table 3-3 and the layouts of the cables are shown in Figure 3-2. 3M SCOTCH-WELD DP8010 epoxy was used to attach the cables to the pipes.

Table 3-2 Schematic illustration of the selected strain sensor cable (Wu et al., 2015)

Brand	NanZee Sensing Technology Co.	NanZee Sensing Technology Co.
Model	NZS-DSS-C07	NZS-DSS-C02
Cross section	 <p>0.9mm</p>	 <p>5mm</p>
Side view	 <p>Hytre buffer Core optic</p>	 <p>Sheath Metal reinforcer Fiber</p>

NanZee 5mm cables (blue lines) were used in the longitudinal direction to mimic the use at construction sites. They were attached on both pipes, 45 degrees apart, numbered S9-S25. Though most longitudinal cables start and end at similar locations, some variations are due to the experimental setup’s conflicts.

To better understand the deformation mechanism of the pipeline and joint section, NanZee 0.9mm (red lines) were used for measuring circumferential strains, numbered S1-S9. Three circumferential sensors with about 18-inch spacing were installed on both spigot and bell

pipe. In addition, another three circumferential sensors were attached to the bell joint, end, and middle of the section, and the location on top of the locking segments (i.e., about 3.5 inches from the bell face).

A Rayleigh-based optical frequency domain reflectometry (OFDR), Luna ODiSI 6100 series (LUNA, 2022), was used in this experiment for data acquisition. The analyzer is capable of measuring up to 50m long fiber optic cable with an accuracy of less than ± 1 micro strain when taking a measurement every 0.65mm. More detail about the cables and analyzer can be found in Appendix A.

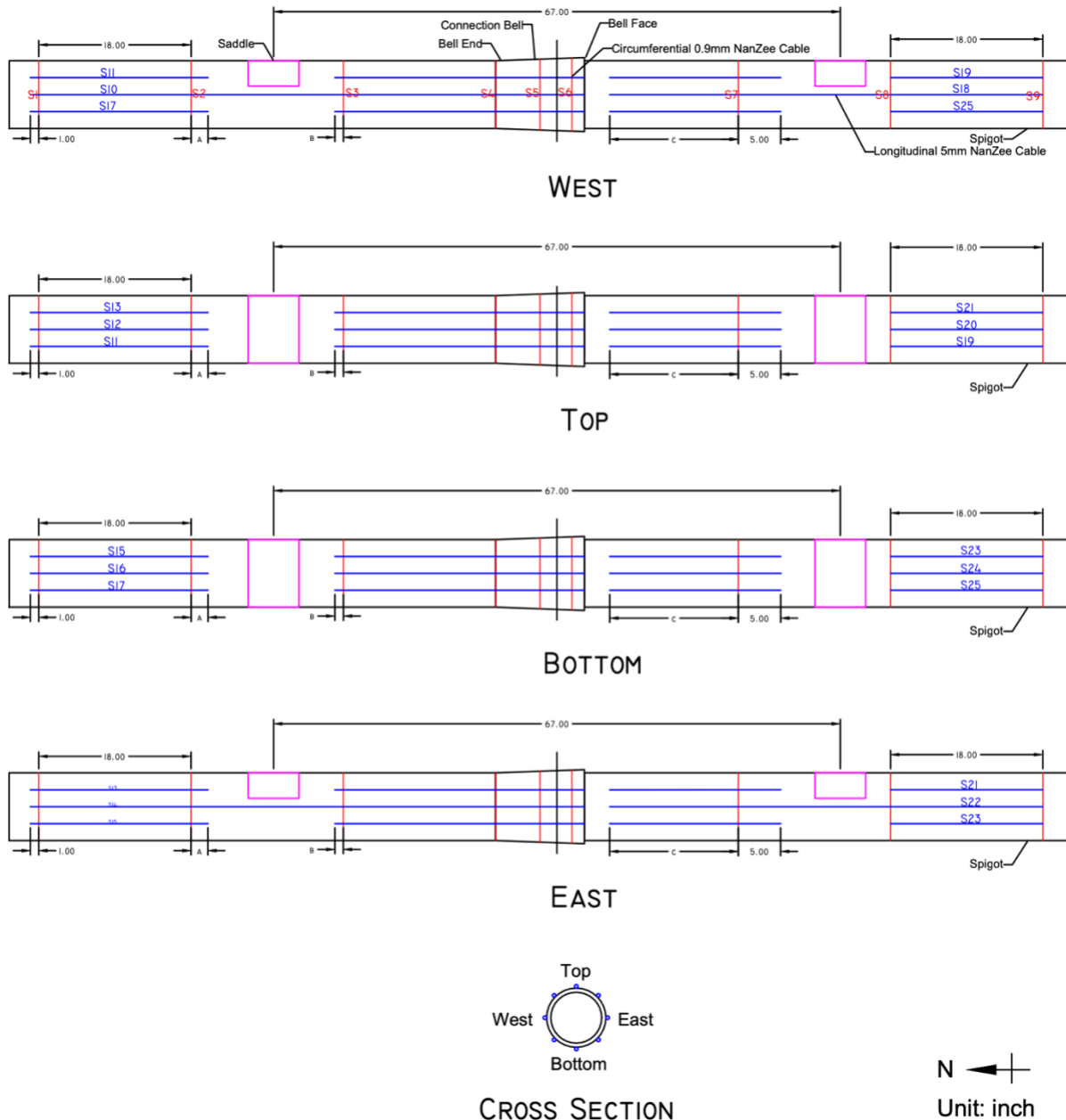


Figure 3-2 DFOS instrumentation plan

Table 3-3 DFOS local names

Instrument	Location	Local Instrument Name
DFOS	64.5 inches north of bell face, Circumferential	S1
	46.5 inches north of bell face, Circumferential	S2
	28.5 inches north of bell face, Circumferential	S3
	Bell end, Circumferential	S4
	Mid location of bell, Circumferential	S5
	3.5 inches north of bell face, Circumferential	S6
	18 inches south of bell face, Circumferential	S7
	36 inches south of bell face, Circumferential	S8
	5 inches south of bell face, Circumferential	S9
	Bell pipe, West, Longitudinal	S10
	Bell pipe, West-top, Longitudinal	S11
	Bell pipe, Top, Longitudinal	S12
	Bell pipe, Top-east, Longitudinal	S13
	Bell pipe, East, Longitudinal	S14
	Bell pipe, East-bottom, Longitudinal	S15
	Bell pipe, Bottom, Longitudinal	S16
	Bell pipe, Bottom-west, Longitudinal	S17
	Spigot, West, Longitudinal	S18
	Spigot, West-top, Longitudinal	S19
	Spigot, Top, Longitudinal	S20
	Spigot, Top-east, Longitudinal	S21
	Spigot, East, Longitudinal	S22
	Spigot, East-bottom, Longitudinal	S23
	Spigot, Bottom, Longitudinal	S24
	Spigot, Bottom-west, Longitudinal	S25

Table 3-4 Location of longitudinal fiber optic cables

Sensor	Test 1			Test 2		
	A	B	C	A	B	C
S11	2"	0"	10"	2"	1"	5"
S12	2"	1"	10"	2"	1"	5"
S13	2"	1"	10"	2"	1"	5"
S15	2"	1"	10"	2"	1"	5"
S16	0"	1"	10"	2"	1"	5"
S17	4"	1"	10"	2"	1"	5"
S19	2"	1"	10"	2"	1"	5"
S20	2"	1"	10"	2"	1"	5"
S21	2"	1"	10"	2"	1"	5"
S23	2"	1"	10"	2"	1"	5"
S24	2"	1"	10"	2"	1"	5"
S25	2"	1"	10"	2"	1"	5"

4. Test Results

All test results are discussed in this section. In addition, a summary of the observed failure mode and the performance of the 8-inch diameter U.S. Pipe TR-XTREME™ joint under biaxial tensile force is described.

4.1 Calculation Approach

The approaches to calculating the deflection angle and moment are discussed herein. The pipes are assumed to be rigid bodies, and the deflection angles of the pipes are calculated using equations (1) – (3). The vertical displacements of the pipes were measured by the vertical wire pots (VWP) located beneath the pipes. θ_{Bell} and θ_{Spigot} are the deflection angles of the bell pipe and the spigot, respectively. The overall deflection angle, θ_{Total} , of the joint is defined as the sum of the two side angles.

$$\theta_{Bell} = \tan^{-1}\left(\frac{\text{vertical displacement of bell pipe}}{\text{distance between VWP and the end support}}\right) \quad (1)$$

$$\theta_{Spigot} = \tan^{-1}\left(\frac{\text{vertical displacement of spigot}}{\text{distance between VWP and the end support}}\right) \quad (2)$$

$$\theta_{Total} = \theta_{Bell} + \theta_{Spigot} \quad (3)$$

The system is considered to be a simple-supported beam. The self-weight, including the pipe's and water's weight, is assumed to be evenly distributed, and hence the moment introduced by self-weight is calculated based on equation (4), where w is the uniform load due to the self-weight, and l is the length of the pipe. The additional moment applied to the central portion of the pipe is calculated using equation (5), where P is the actuator load, and L is the distance between the support and the loading location.

$$M_{distrib} = \frac{wl^2}{8} \quad (4)$$

$$M_{central} = \frac{PL}{2} \quad (5)$$

4.2 Experimental Data Analysis

As mentioned in Chapter 2, four stages (self-weight moving down, actuator pushing down, water pressurization, and pull) were conducted for the two biaxial tension tests. This section discusses the performance of the pipes under different loading and boundary conditions using experimental data.

4.2.1 Joint Moment and Deflection

The measured moment-rotation (deflection) relationships of the two specimens are shown in Figure 4-1. The pipes were first moving downward due to the gravity forces. The equilibrium point was achieved when the specimens reached about 3.58-degree and 3.94-degree deflection, respectively, with a moment of about 13.6 kip-in.

Next, a vertical force was applied to push the pipeline down until reaching a total deflection of 8.36 degrees. The specimens reached the targeted deflection angle with moments of about 1033.5 kip-in and 871.4 kip-in, respectively.

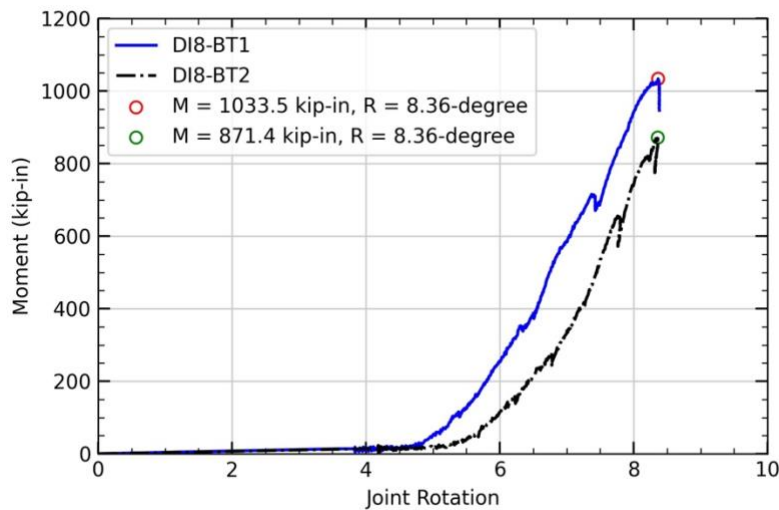


Figure 4-1 Moment vs. Rotation (Deflection angle)

As shown in Figure 4-1, Specimen 1 constantly requires a larger moment to achieve the desired deflection, due to the difference in the locking segments' orientations. For Specimen 1, the spigot needs to overcome the locking segment located on the top while deflecting relatively to the bell in the joint to achieve the given deflection angle. Instead of having a locking segment at the top side (12 o'clock) location, Specimen 2 has a rubber gasket to seal the single slot, which allows a larger displacement. Therefore, Specimen 2 tends to have a larger deflection with a similar applied moment. In addition, while comparing the stress developed at the bottom edge of the spigot (highlighted in purple), the concentrated stresses are higher than that from Specimen 2. The mechanism is shown in Figure 4-2.

After the specimens reached an 8.36-degree deflection, a monotonic axial force was applied to the specimen. During this stage, the vertical actuator remained in place to force the pipes to maintain an 8.36-degree deflection while being pulled.

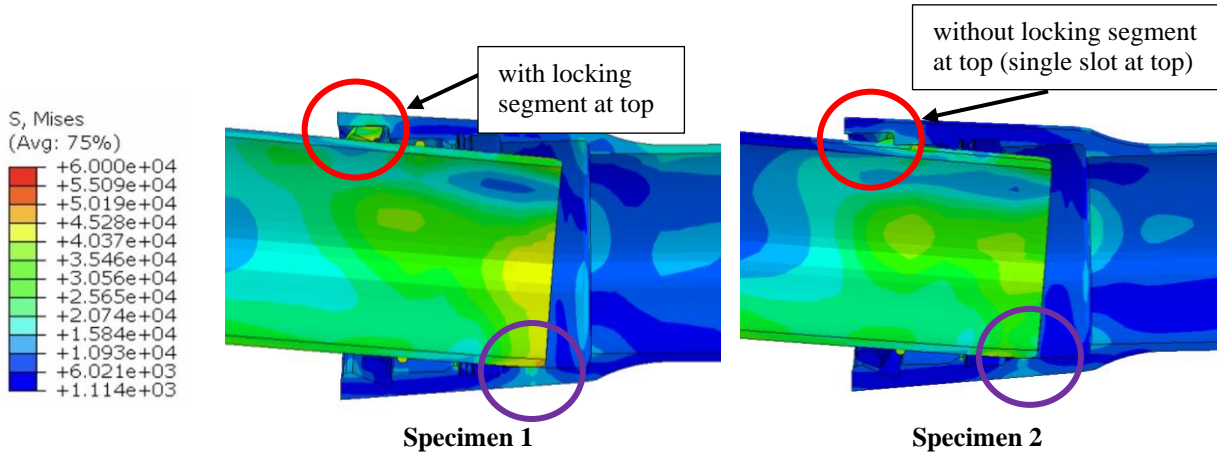


Figure 4-2 Sketch of the bell after Push Down stage

4.2.2 Axial Force and Joint Opening

Specimens were pulled with a minimum 8.36-degree deflection until a severe failure occurred. Figure 4-3 shows the axial force and average joint opening curve of the specimens. The peak values are about 171 kips and 145 kips, individually. The average joint opening at maximum force is about 2.3 inches (Specimen 1) and 2 inches (Specimen 2). The difference is again due to the locking segment’s orientations.

Figure 4-4 demonstrates the stress distribution of the bell after being pulled. As shown in the plots, the stress distributions and the deformation of the bell varies. While being pulled, frictions were developed between the spigot and the locking segments located at 3, 9, and 12 o’clock (west, east, top) sides. Since the pipes were bent, the locking segment located at the bottom side (6 o’clock) was not well-contacted with the spigot, resulting in a smaller frictional force (i.e., smaller stress was developed at the bottom side). Due to the locking segment located at the top position of Specimen 1 but not of Specimen 2, the weld bead in Specimen 1 may counteract the raised internal surfaces of the bell, resulting in mutual compression. This compression generates a higher axial force due to increased friction during pulling. Besides, the deformed shapes of the bell of the two specimens are different. A symmetric deformation can be observed in Specimen 2. Because of the different force transfer and deformation mechanisms, the ultimate capacities vary between the specimens.

The results of the two tests are summarized in Table 4-1.

Table 4-1 Summary of the tests

	Locking Segments Orientation	Max. Axial load (kips)	Max. Ave. Joint Opening (in.)	Total Rotation (degree)
Specimen 1	9 o'clock	171	2	8.36
Specimen 2	12 o'clock	145	2.3	8.36

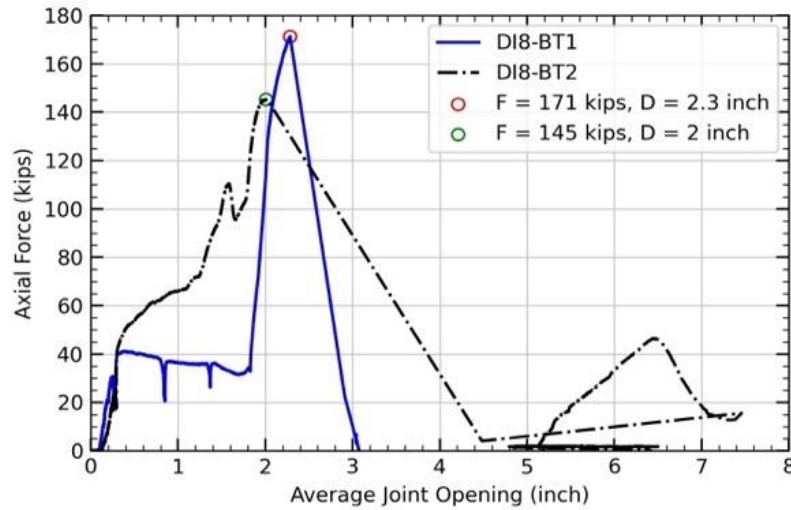


Figure 4-3 Axial force vs. average joint opening

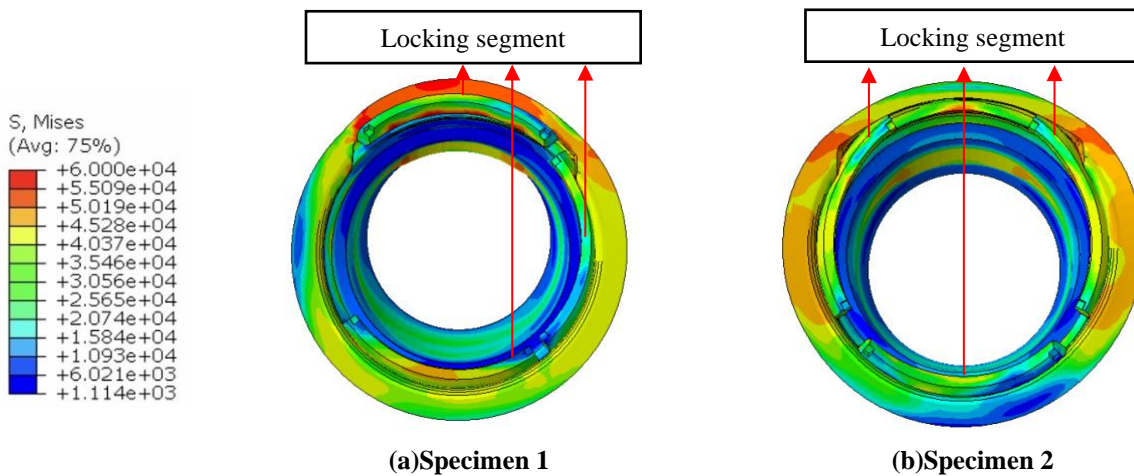


Figure 4-4 Stress distribution of the cross-section of the bell under the Pull stage

4.2.3 Axial Strains

General

The axial strain results measured by the strain gauges are shown in Figure 4-5 and Figure 4-6 for the two specimens, respectively. Looking at the Self-Weight Moving Down and Actuator Pushing Down stages, one can observe a clear pattern: the top side (12 o'clock) is generally under compression due to bending, and the bottom side (6 o'clock) is mainly under tension from both of the specimens. However, the magnitude of the strains of the east side (3 o'clock) and west side (9 o'clock) differ between the specimens. This is because Specimen 1 has a non-symmetric configuration of the locking segments (i.e., locking segments were placed on the west side but not on the east side). Since the locking segment provides a better constraint than the rubber gasket, the pipe tends to move out more on the rubber gasket side, resulting in a

bending moment. Hence, for Specimen 1, tensile strains were developed at the west side (9 o'clock), and compressive strains were developed at the east side (3 o'clock).

On the contrary, since the locking segments were placed at both the east and west sides of Specimen 2, the above-mentioned phenomenon is not observed. Theoretically, the axial strains at the east side (3 o'clock) and west side (9 o'clock) of Specimen 2 would be close to zero. However, the strain gauges might not be located exactly at the east and west locations due to installation errors, resulting in non-zero strains on both sides. During the Pull stage, tensile strains were developing in both specimens' directions.

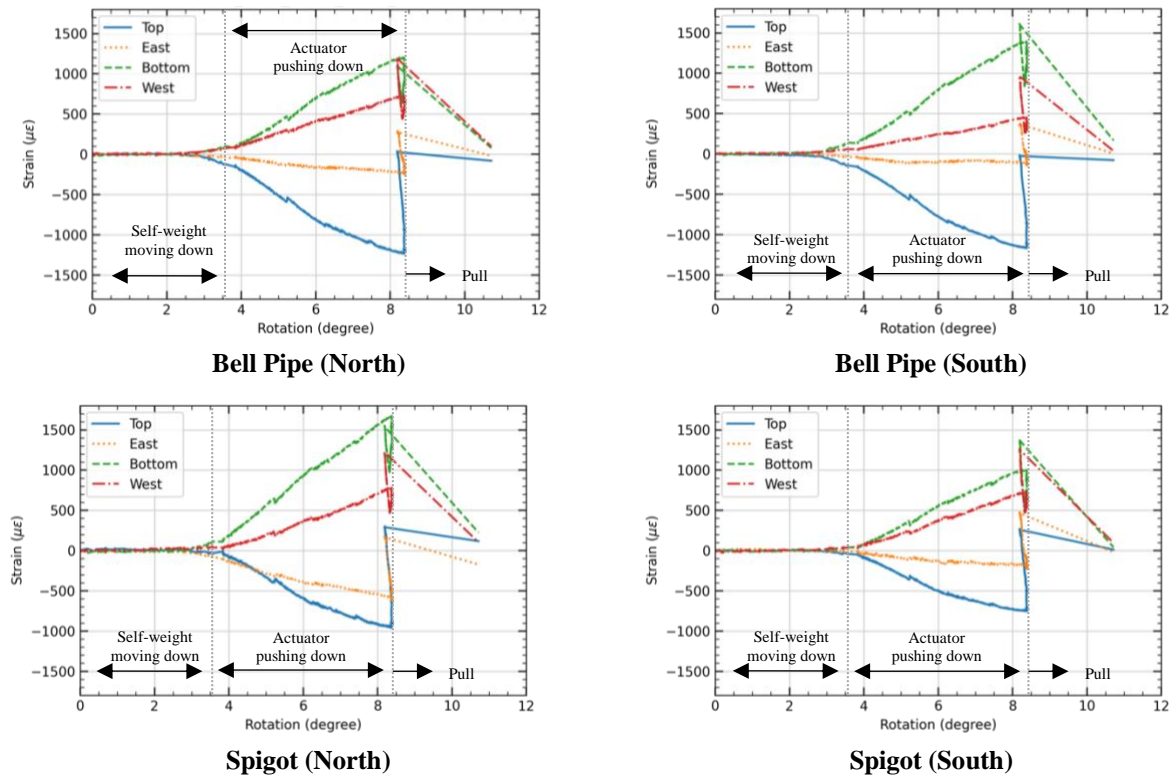


Figure 4-5 Axial strain vs. rotation (deflection) of Specimen 1

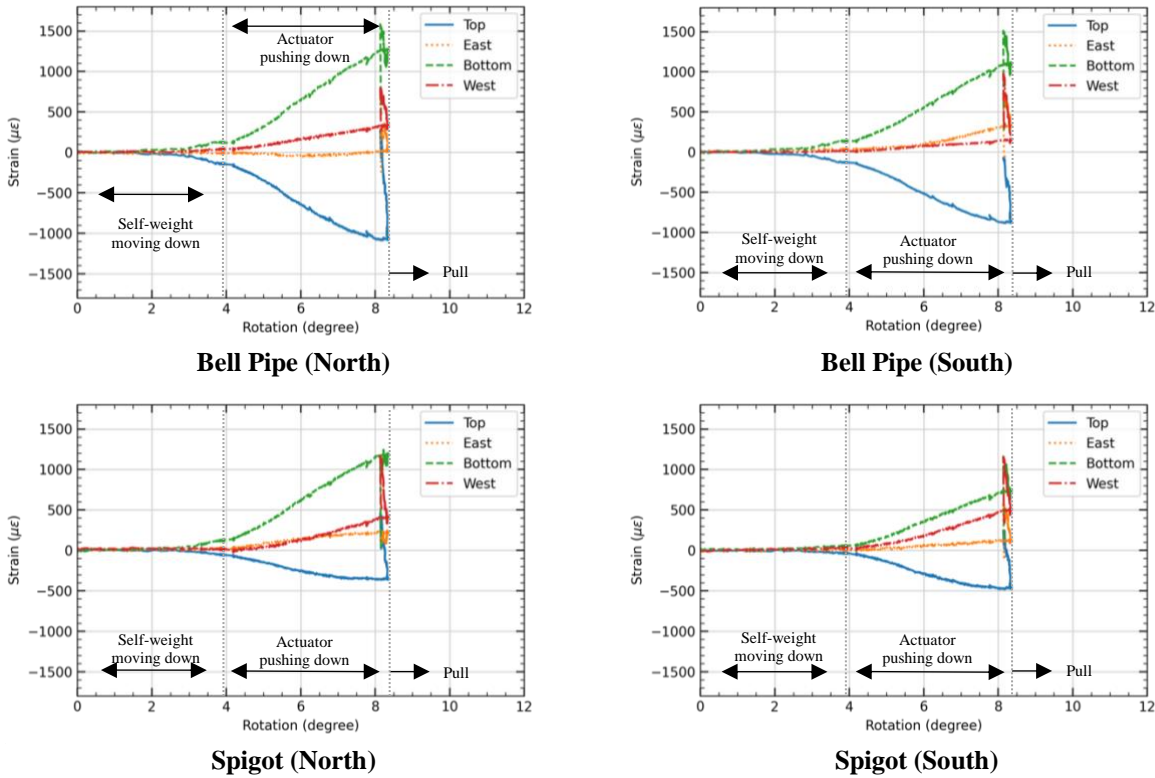


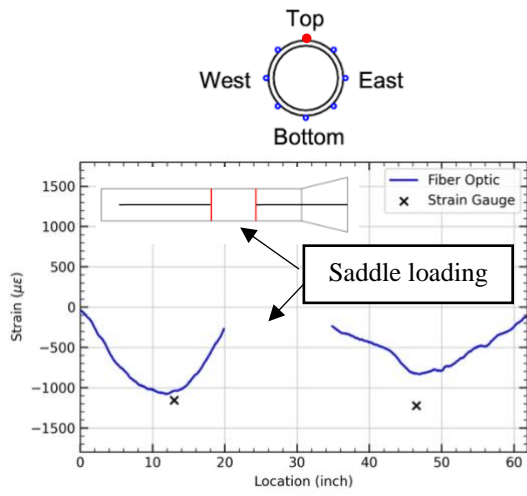
Figure 4-6 Axial strain vs. rotation (deflection) of Specimen 2

Bending stage

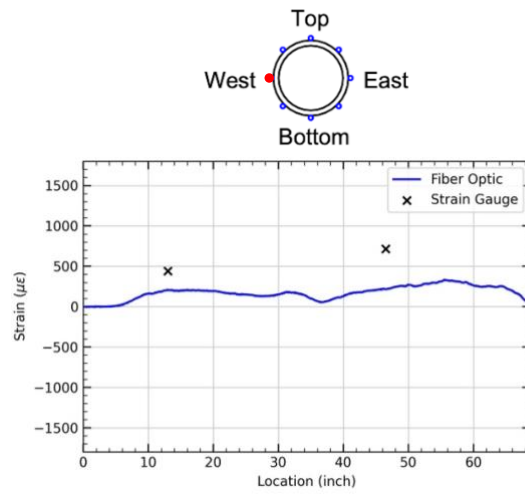
Figure 4-7 and Figure 4-8 show the axial strain distribution of bell pipe and spigot when the pipe first achieved the targeted deflection contraction (i.e., 8.36-degree deflection, which occurred at the end of the Actuator Pushing Down stage) measured by the DFOS placed on specimens. In this section, the 3D continuous strain profile of the jointed pipeline in both longitudinal and circumferential directions is revealed by DFOS data against strain gauge. All the strain distribution of the sensors is plotted from the north to the south. Due to experimental setup conflict, the fiber optic cables were not attached to the locations where the saddles were placed, resulting in missing values in the middle section of the plots.

Since the pipes are being pushed down, most of the sections of the pipes on the top side (12 o'clock) are under compression. However, smaller compressive strains close to the saddle can be found on the top side (12 o'clock). The saddles are transferring a large force pointing downward to the pipe, and due to the Poisson's effect, tensile strains in the axial direction are developing. Hence, the strains close to the saddle are the combination of strains introduced by both bending and Poisson's effect. At this stage, the specimen can be treated as experiencing pure bending forces. Hence, the axial strains at the west side (9 o'clock) remain small and close to zero. The slight difference between the strain gauges and fiber optic sensor results are due to the offset between each other.

More fiber optic sensor results can be found in Appendix B.

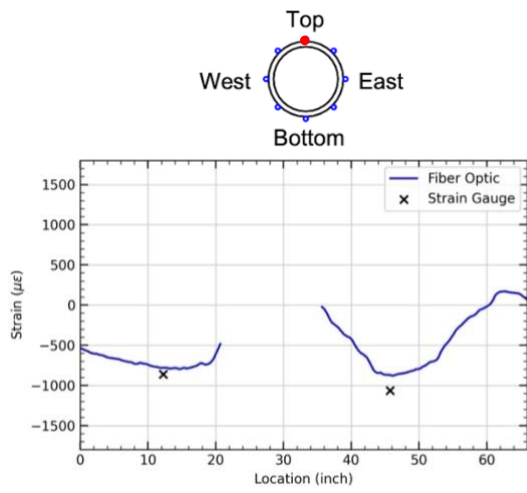


(i)

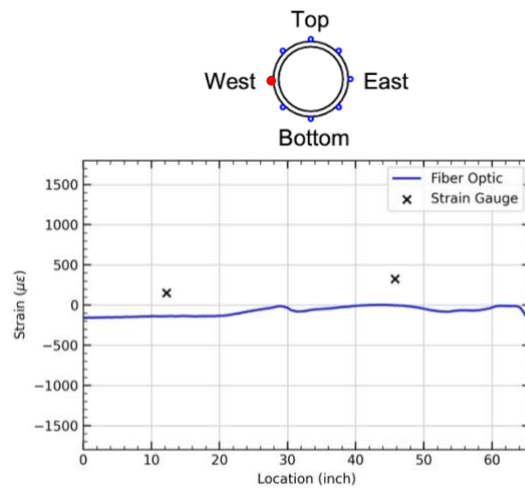


(ii)

(a) Specimen 1



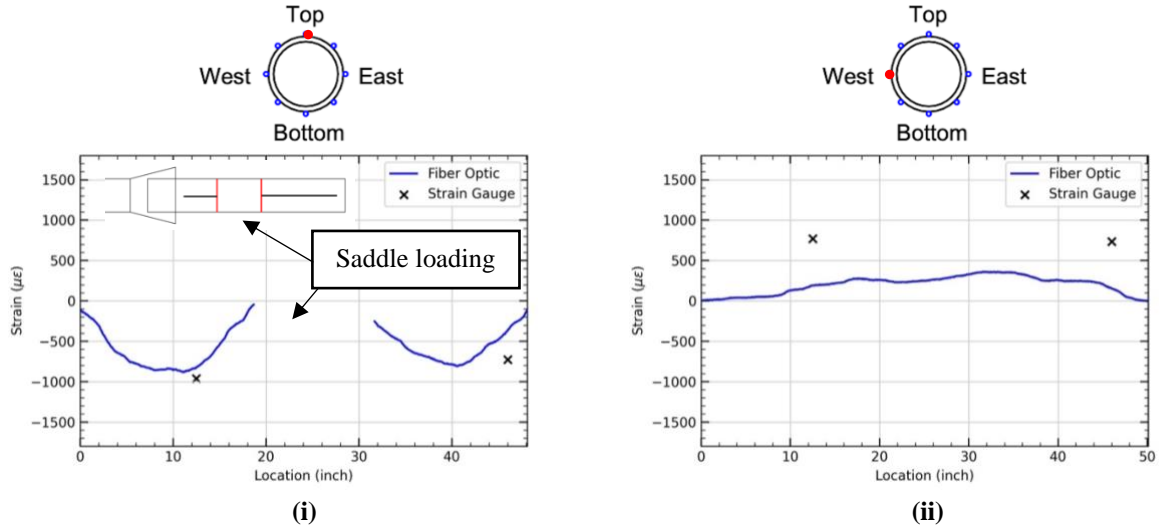
(i)



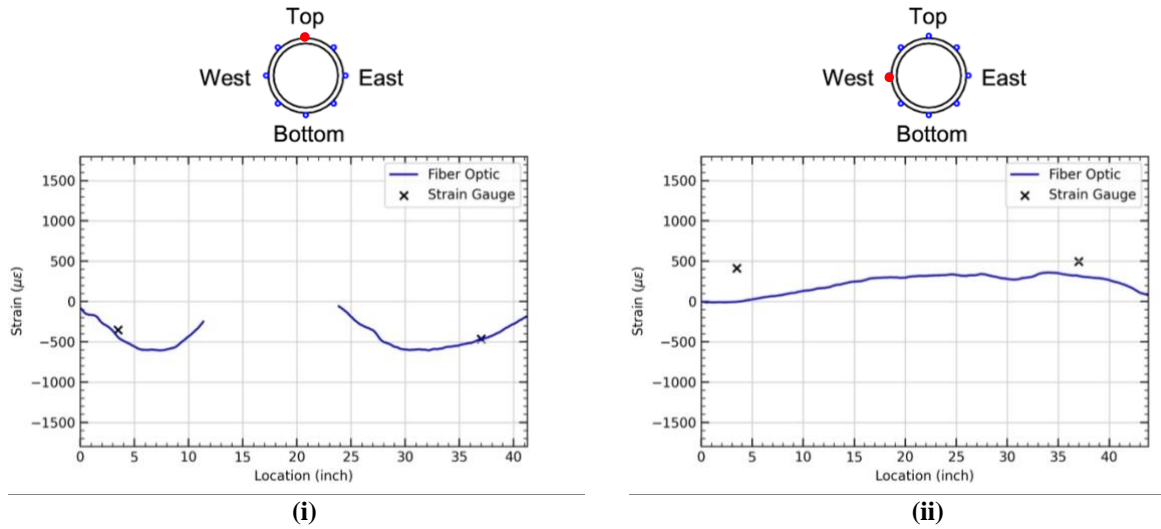
(ii)

(b) Specimen 2

Figure 4-7 Strain development of bell pipe in the longitudinal direction under 8.36-degree deflection. (a) Specimen 1; (b) Specimen 2



(a) Specimen 1



(b) Specimen 2

Figure 4-8 Strain development of spigot in the longitudinal direction under 8.36-degree deflection condition. (a) Specimen 1; (b) Specimen 2

Pulling stage

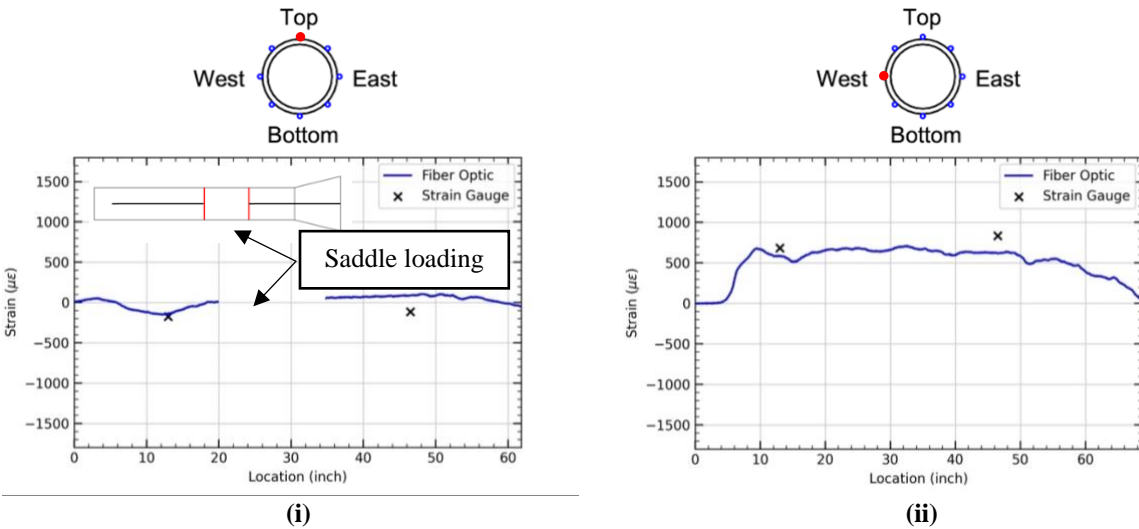
Figure 4-9 and Figure 4-10 show DFOS results of bell pipe and spigot during the Pull stage under an axial force of 140 kips. A different pattern can be observed from the bell pipe of the two specimens. Take the results from the west side (9 o'clock), for example. Most of the sections are under tension because of the axial force. However, the locking segments were being pulled out by weld bead, resulting in a significant compression strain on the surface close to the locking segment in Specimen 2. In contrast, for Specimen 1 at the same Pull stage with a 140 kips axial force (equivalent to the peak pull force in Specimen 2), no similar phenomenon is captured by the sensor, due to the locking segments in Specimen 1 might not be pulled under the critical loading condition. As a result, the sensor didn't register the phenomenon evident in

Specimen 2.

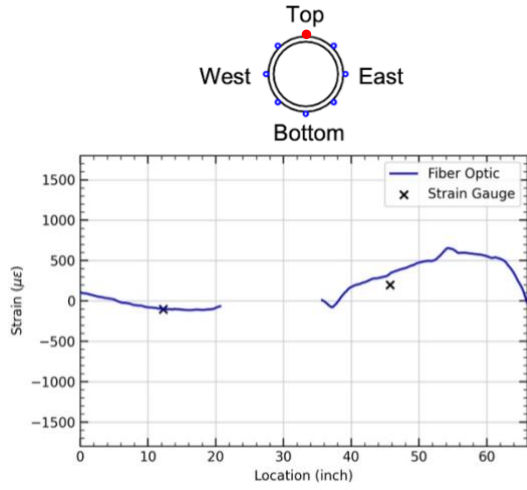
Looking at the results from the top side (12 o'clock) of Specimen 2, one can observe a larger tensile strain close to the bell. This might be the reason that as the locking segments on the sides (3 and 9 o'clock) were pulled out, the thickness of the bell on the top decreased, resulting in a larger tensile strain close to the bell section. A detailed discussion can be found in Section 5.

The spigot's strain distribution is similar between the two specimens. Since the specimens were bent to the desired deflection angle, the top sides of the specimens were under compression, and the bottom side was under tension. During the pulling stage, although tensile strains were developed at all the faces, the ultimate tensile strains at the top side were the smallest, and those at the bottom side were the largest. The axial strain results of the top and west sides of the two specimens are shown in Figure 4-9 and Figure 4-10 (c)-(d).

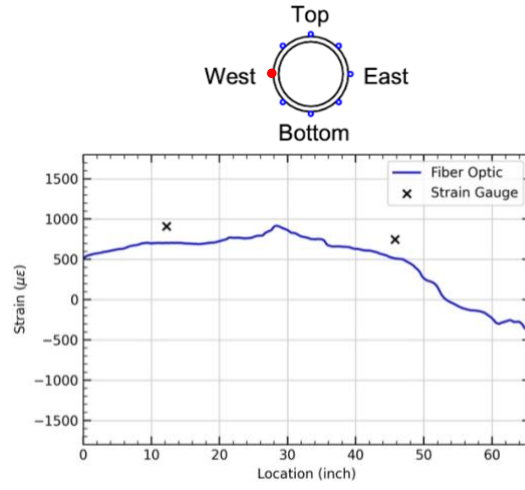
All the axial strain results measured by fiber optic sensors are listed in Appendix B.



(a) Specimen 1



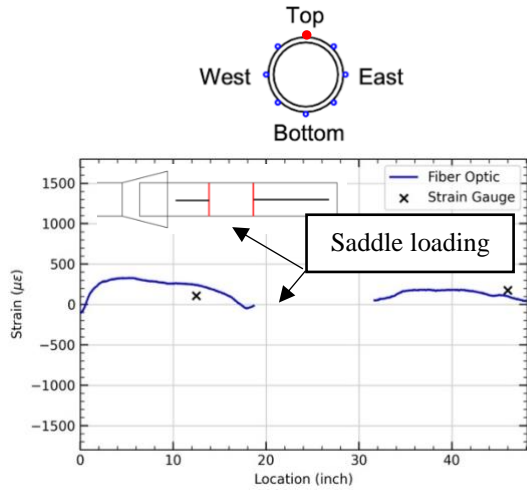
(i)



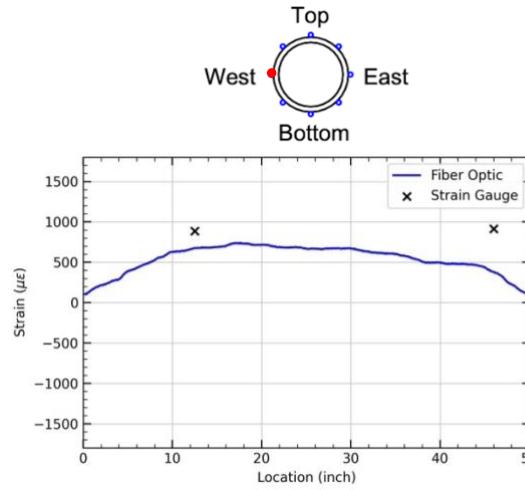
(ii)

(b) Specimen 2

Figure 4-9 Strain development of bell pipe in longitudinal direction under 140 kips axial force loading condition. (a) Specimen 1; (b) Specimen 2



(i)



(ii)

(a) Specimen 1

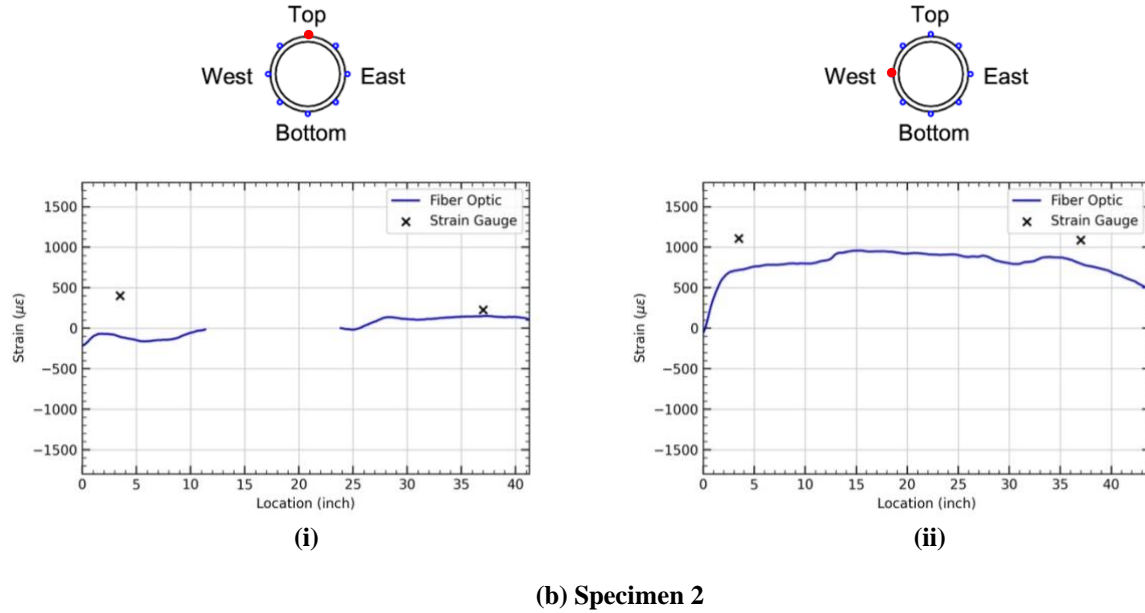


Figure 4-10 Strain development of spigot in longitudinal direction under 140 kips axial force loading condition. (a) Specimen 1; (b) Specimen 2

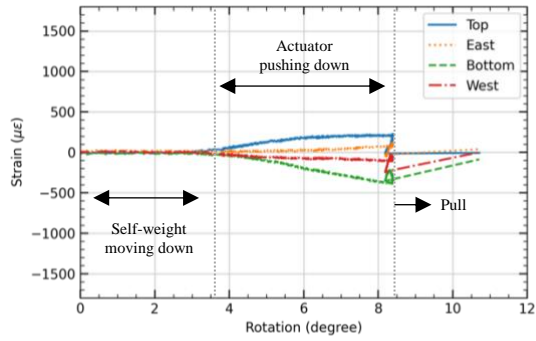
4.2.4 Hoop Strains

General

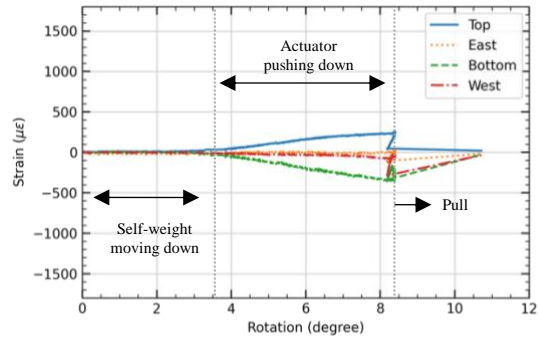
The relationships between the hoop strains, measured by strain gauges with total deflection, are plotted in Figure 4-11 and Figure 4-12 for Specimens 1 and 2, respectively. The Actuator Pushing Down stage is close to pure bending conditions; hence, compressive axial strain can be found at the top side (12 o'clock), and tensile axial strain can be observed at the bottom side (6 o'clock), as discussed in the previous section. Due to Poisson's effect, the strains in the circumferential direction are mainly opposite to those in the longitudinal direction. Tensile hoop strains can be observed at the top side (12 o'clock), and compressive hoop strains occur at the bottom side (6 o'clock). The strains at the west and east (3 and 9 o'clock) sides are generally small and close to zero.

During the Pull stage, the mechanism of the pipes is similar to the previous stage, meaning that expansion can be found on the top side, compression is observed at the bottom side, and small deformation develops at the other two sides. However, the mechanism of the bell differs between the two locking segment orientations. As the locking segments tend to be pulled out, the bell tends to shrink on the location where the single slot locates and expand on the other sides to allow the locking segments to come out.

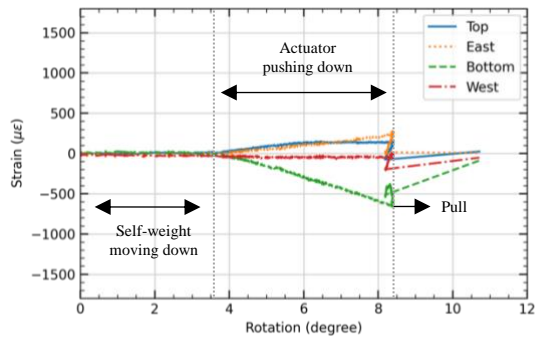
The detailed mechanism of the pipe deformation will be discussed using the fiber-optic sensing results in the following sections regarding each stage.



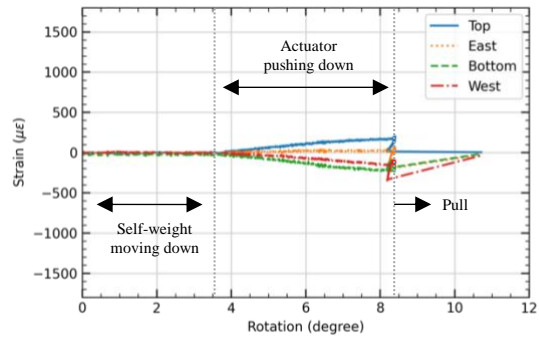
Bell Pipe (North)



Bell Pipe (South)

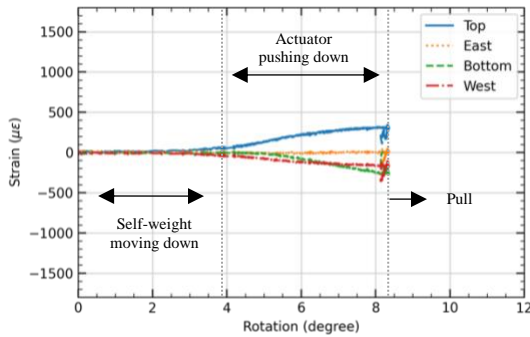


Spigot (North)

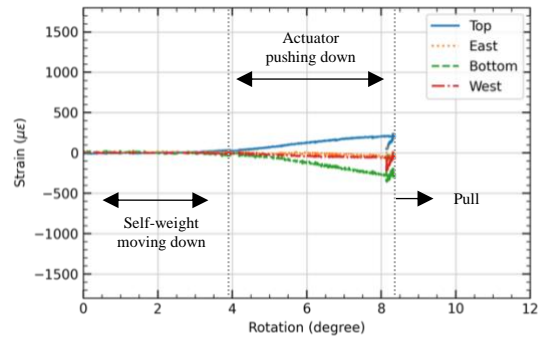


Spigot (South)

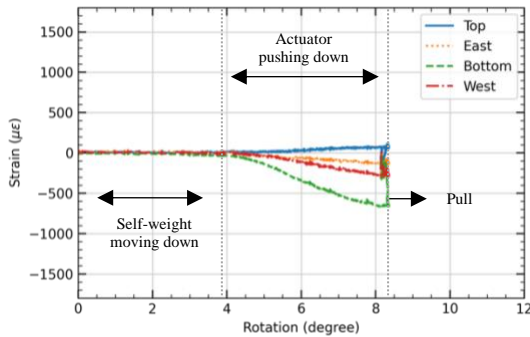
Figure 4-11 Hoop strain vs. rotation of Specimen 1



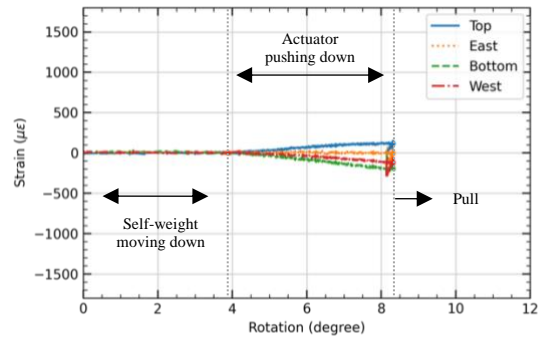
Bell Pipe (North)



Bell Pipe (South)



Spigot (North)



Spigot (South)

Figure 4-12 Hoop strain vs. the rotation of Specimen 2

Bending stage

The fiber optic results of the hoop strains close to the connection bell sections when the pipe first achieved the targeted deflection angle (i.e., 8.36-degree deflection, which occurred at the end of the Actuator Pushing Down stage) in Specimen 1 and Specimen 2 are plotted in Figure 4-13 and Figure 4-14. During the bending stage, the strain distribution pattern of the two specimens is similar. Tensile hoop strains are observed on the top side (12 o'clock) and compressive strains on the bottom (6 o'clock) of the pipes, which indicates that the pipes are squashing, as shown in Figure 4-13(a and d) and Figure 4-14(a and d).

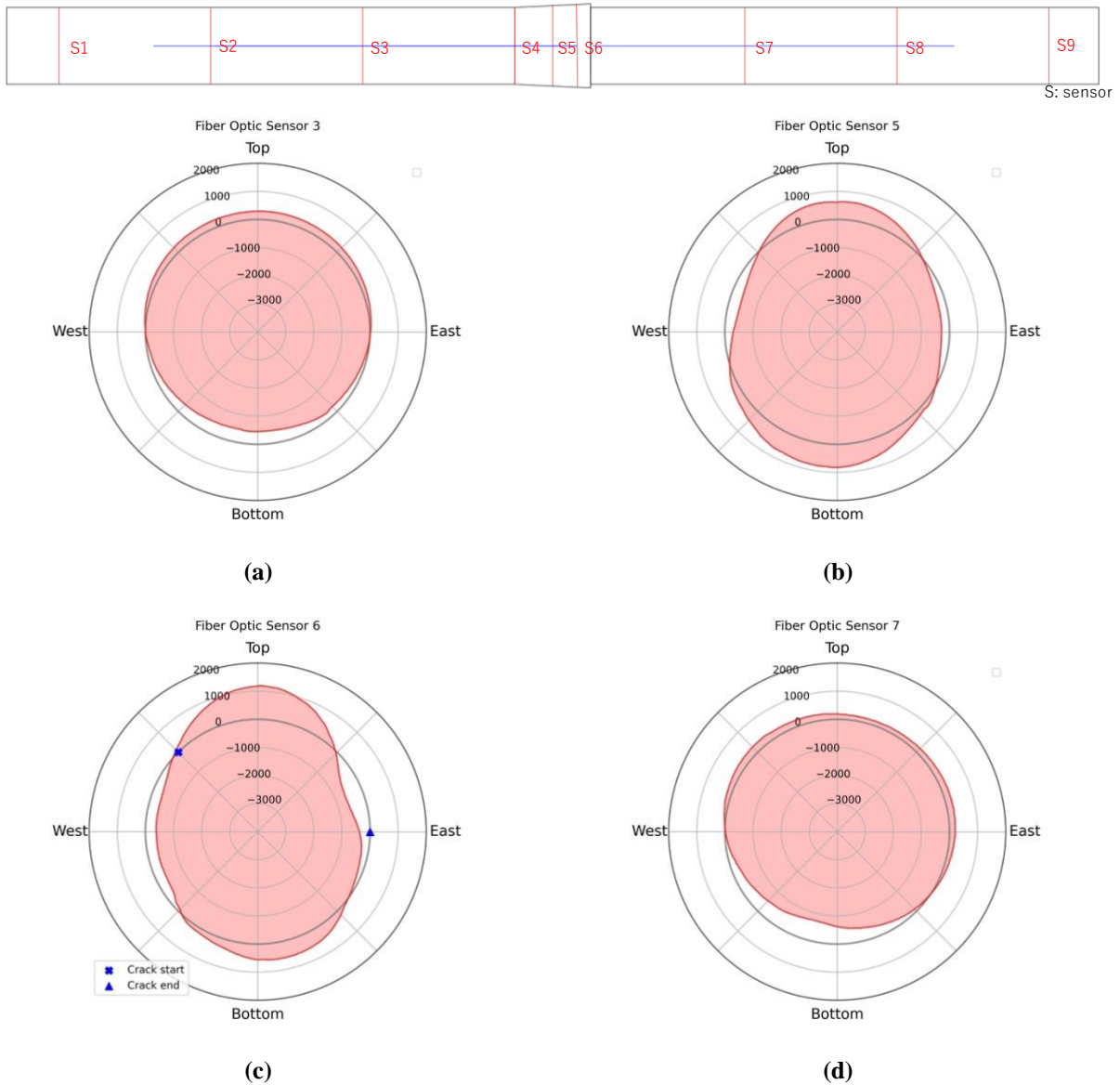


Figure 4-13 Strain distribution in the circumferential direction of Specimen 1 under 8.3-degree deflection condition. (a) sensor on the bell pipe (b) sensor at the mid location of the bell (c) sensor on top of the locking segments on the bell (d) sensor on the spigot

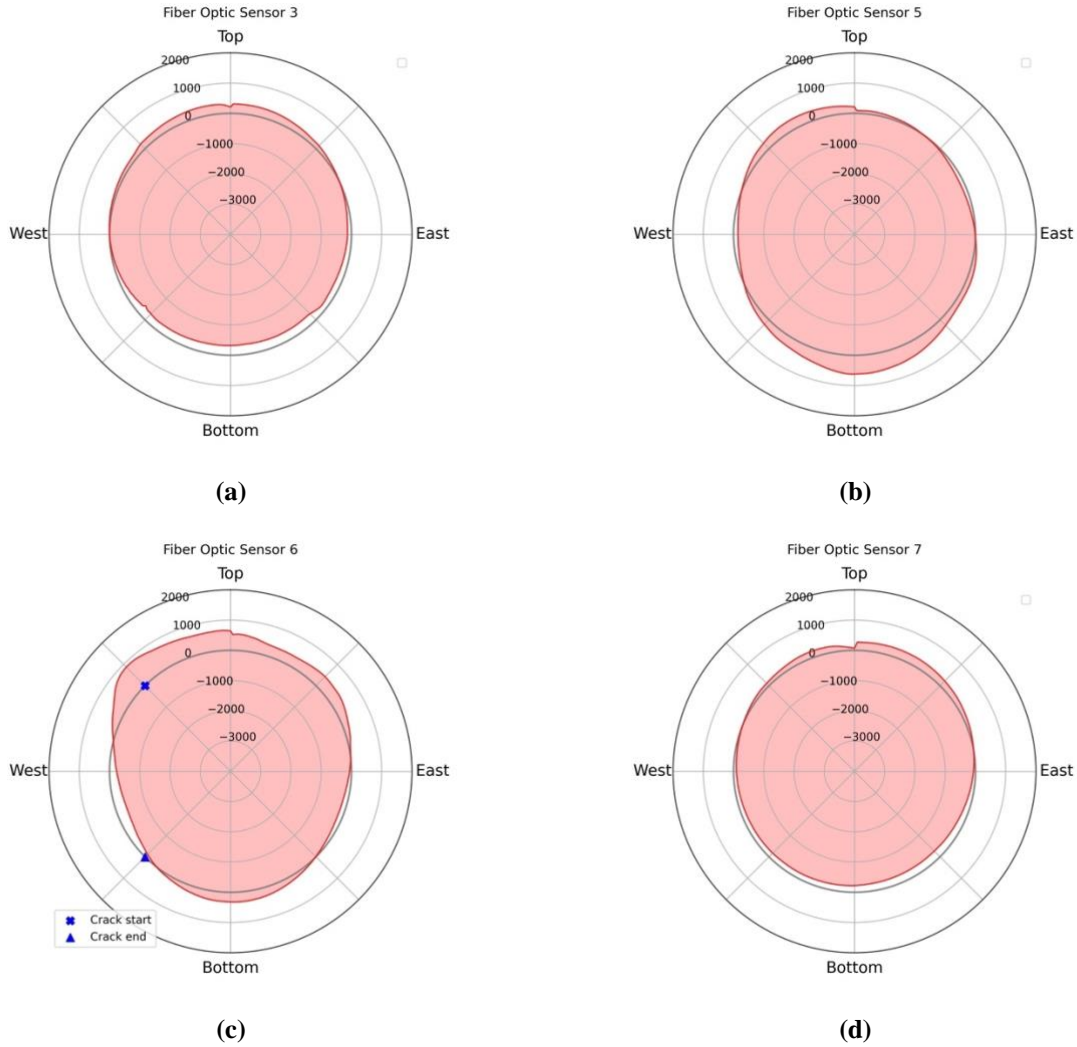
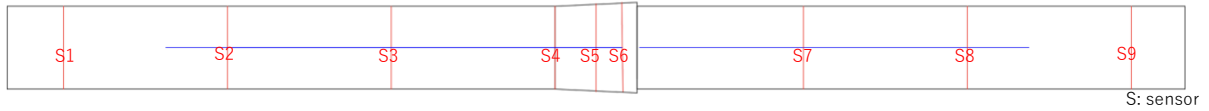


Figure 4-14 Strain distribution in circumferential direction under Specimen 2 under 8.3-degree deflection condition. (a) sensor on the bell pipe (b) sensor at the mid location of the bell (c) sensor on top of the locking segments on the bell (d) sensor on the spigot

On the other hand, the bells were expanding on the top and bottom sides (6 and 12 o'clock) and compressing on the east and west sides (3 and 9 o'clock), as shown in Figure 4-13(c) and Figure 4-14(c). The spigot contacted the top and bottom sides of the bell, which expanded the bell on both sides and resulted in compression on the other two sides, as shown in Figure 4-15.

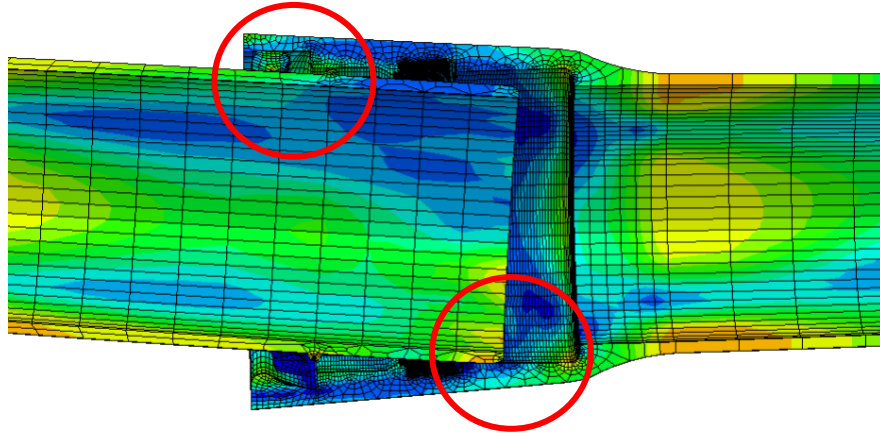


Figure 4-15 Joint deformed mechanism in Push Down stage

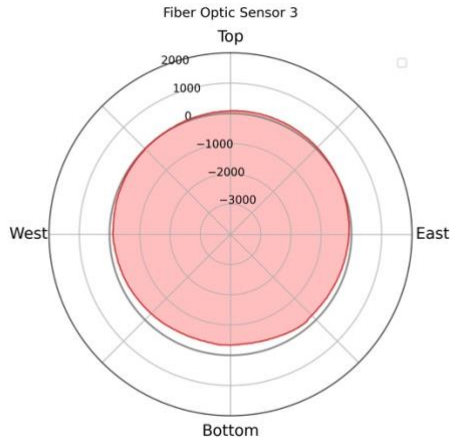
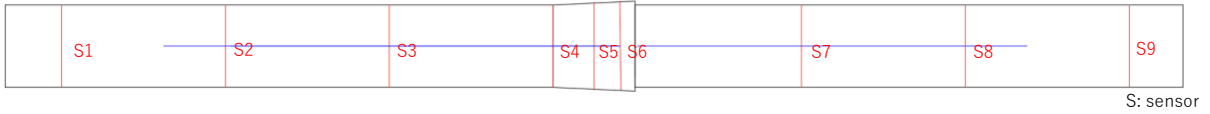
Pulling stage

Figure 4-16 and Figure 4-17 demonstrate the hoop strain results under 140 kips axial force conditions measured by DFOS for both specimens. Similar to the previous stage, the pipes experienced circumferential tensile strain on the top (12 o'clock) and compressive strain on the bottom sides (6 o'clock).

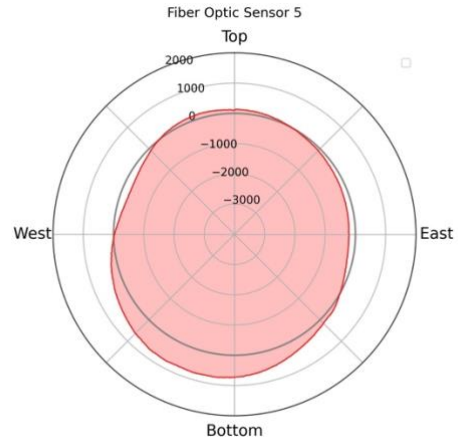
Due to the different orientations of the locking segments, the bells of the two specimens reacted differently. While being pulled, the locking segments in the bell section were in contact with the weld bead on the spigot. The locking segments tended to expand the bell to be pulled out. For Specimen 1, instead of a locking segment, a rubber gasket was placed on the west side (9 o'clock). Hence, the bell tends to shrink on the west and east (3 and 9 o'clock) sides and expand on the top and bottom (6 and 12 o'clock) sides, which allows the locking segments to be pulled out. Similarly, since the rubber gasket was placed on the top side (12 o'clock) of Specimen 2, the bell tends to compress on the top and bottom (12 and 6 o'clock) and expand on the west and east sides (9 and 3 o'clock).

The pipes failed because of cracks in the bells. Although the cracks propagated differently, the start points of the cracks are similar. They are at the mid-point of the top and west sides, where the boundary of the single slot and locking segments is located. For Specimen 1, the cracks started from the mid-point of the top and west sides through the top to the east. For Specimen 2, a shorter crack was observed. The cracks propagated from the mid-point of the top and west sides to the mid-point of the west and bottom sides. The start and end points of the cracks are marked on the plots of Sensor 6 in Figure 4-16 and Figure 4-17, which is located on top of the locking segments.

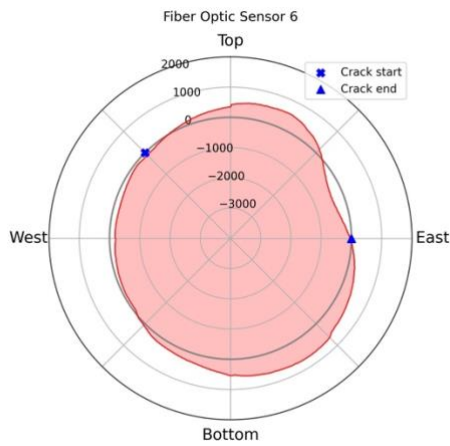
All the hoop strain results measured by the fiber optic sensors are presented in Appendix B.



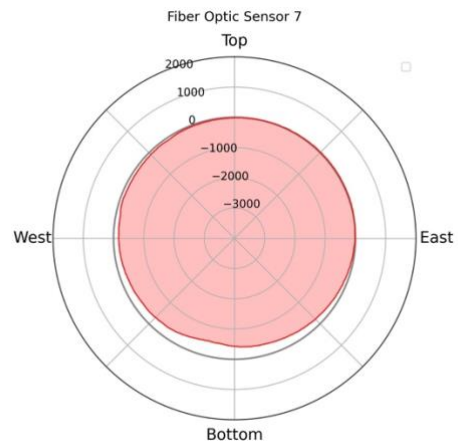
(a)



(b)



(c)



(d)

Figure 4-16 Strain distribution in the circumferential direction of Specimen 1 under 140 kips loading condition. (a) sensor on the bell pipe (b) sensor at the mid location of the bell (c) sensor on top of the locking segments on the bell (d) sensor on the spigot

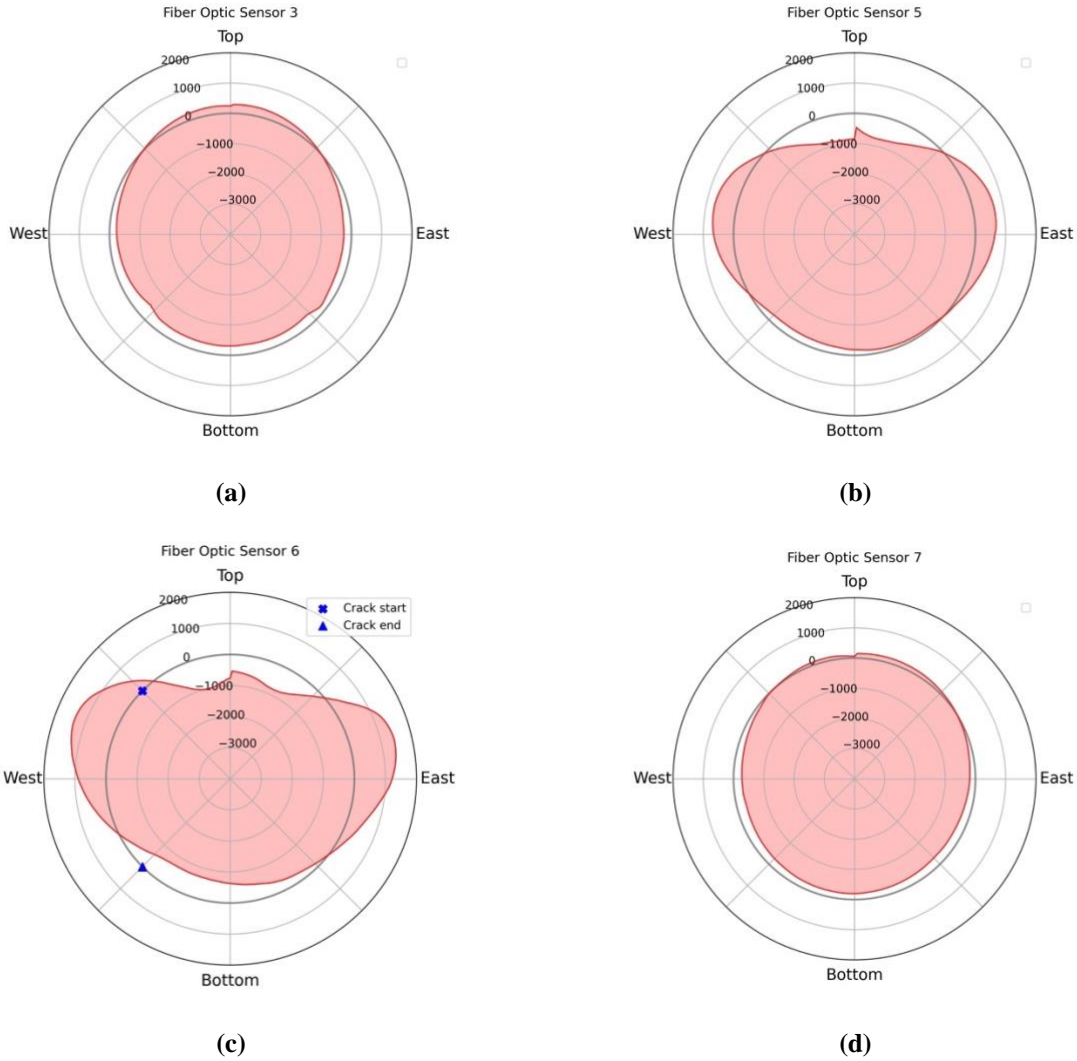
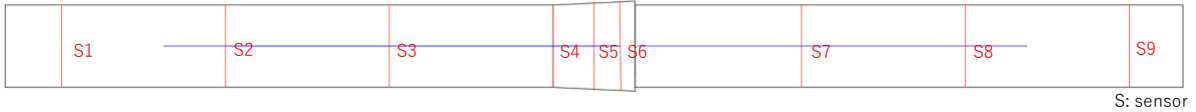


Figure 4-17 Strain distribution in the circumferential direction of Specimen 2 under 140 kips loading condition. (a) sensor on the bell pipe (b) sensor at the mid location of the bell (c) sensor on top of the locking segments on the bell (d) sensor on the spigot

4.3 Failure Modes

The experiments were designed to test up to a pipe failure or a significant water leakage resulting in a large water pressure drop. The tests were stopped due to the pipe failing at the bell near the location of the locking segments, as shown in Figure 4-18. The pipe failed with severe water leakage when the tensile forces reached 171 kips with 2.3 inches displacement for Specimen 1 and 145 kips with 2 inches displacement for Specimen 2, respectively, meaning that the orientation of the locking segments would be influential to the seismic capacity of the pipe.

Although the cracks on the bell propagated differently, they both started from the mid-point of the west and top position, where the boundary of the single slot and locking segments is located. This would be the weak area of the bell.

The crack on Specimen 1 started from the boundary of locking segments and the single slot, located at the mid-point of the top and west sides, through the top to the east. The crack propagated from the edge to the middle of the bell. A diagonal crack can be observed, as shown in Figure 4-18, meaning that combined shear and tensile stresses dominated the failure. On the other hand, the crack along the circumference of the bell can be found in Specimen 2, indicating that tensile stress was governing the failure. The start point of the crack is similar to the location of Specimen 1, and the crack propagated to the mid-point of the west and bottom. More details will be discussed in Chapter 5.



Figure 4-18 Failure of Bell of Specimen 1 (left) and 2 (right)

5. Finite Element Analysis

5.1 Overview of Numerical Model

Two explicit three-dimensional (3D) full-scale finite element (FE) models, , considering 12 o'clock and 9 o'clock orientations of locking segments, were developed using ABAQUS to examine the pipe behavior under biaxial force. The geometry and material of the pipe and joint models were carefully designed to be consistent with the experiments. The only difference between the two FE models is the orientation of the locking segments (9 o'clock and 12 o'clock).

In the models, the pipelines are simplified into four main parts: a spigot, a bell pipe, three pieces of locking segments and loading saddles. FE meshes used for the analysis are shown in Figure 5-1, where the isotropic 3D solid continuum elements (C3D8R) are used. Especially the finer mesh at the bell section is defined to ensure strain development can be accurately determined. The number of elements and nodes in the finite element model are around 124,779 and 157,117, respectively.

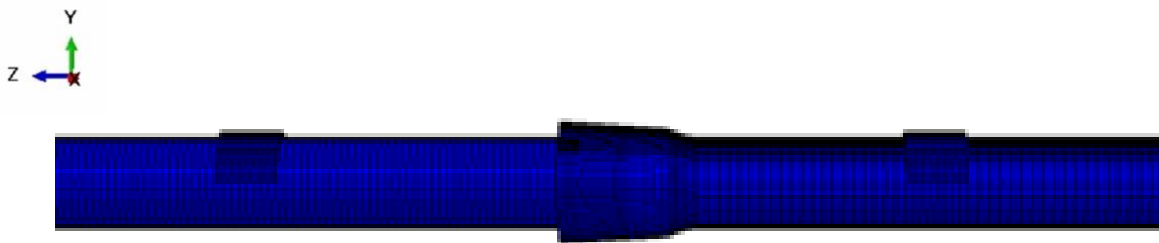


Figure 5-1 3-D FE model mesh for biaxial tension condition

The loading conditions and boundary conditions are briefly summarized as follows. At the bell joint, the interaction between the pipe and the locking segments is set to be contacted and allowed to slip into each other. The normal behavior of the interaction is set to behave as the hard contact, and the friction coefficient of the tangential behavior is set as 0.8 according to the standard friction coefficient between materials of ductile iron and steel ([Engineering ToolBox 2004](#)). To simulate the pipeline subjected to bending moment, two ends were set to allow deflection while being bent. In the simulation, the bending force is applied on the 6-in-width loading saddles, similar as the experimental setup. At the pulling stage, the spigot end is allowed to move horizontally up to 3 inches displacement.

The initial position of the bell and spigot is located the same as that in the experiment, as shown in Figure 5-2. A 50 psi water pressure is applied on the inside surface of the pipelines. A vertical load is first applied to the loading saddles to around 8-degree deflection. Then the axial force is applied to the spigot until the bell joint breaks.

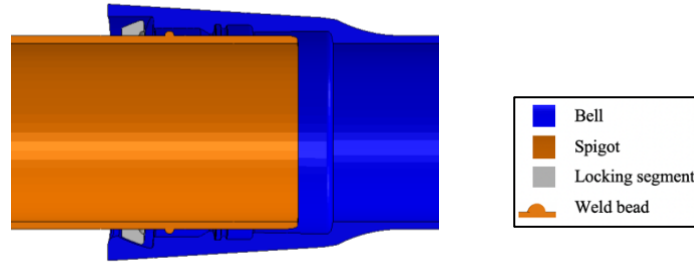


Figure 5-2 Initial position of the bell and spigot

5.2 Determination of Pipe Parameters

Table 5-1 presents the material properties provided by U.S. Pipe for the ductile iron pipe and locking segments used in the tests. The plastic properties are included in the simulation to accommodate some parts of the pipe reaching the yielding stress of the material, resulting in plastic deformation.

Von Mises stress is a value used to determine if a given material yields or fractures in shear. It is mostly used for ductile materials. For the tested US pipes, when the value of Mises stress exceeds the yield stress (42,000 psi), the pipe generates plastic strains with irreversible deformation. The properties utilized in this FE model align with those used for the Tension test finite element method.

Table 5-1 Ductile Iron Pipe properties

Part	Density (lb/in ³)	Young's Modulus (psi)	Poisson's Ratio	Yield Strength (psi)	Ultimate Strength (psi)	Defined Yield Strain	Elongation
Ductile Iron Pipe (plastic)	0.28	23,500,000	0.29	42,000	60,000	0.25%	10%
Locking segments (plastic)	0.3	24,000,000	0.26	42,000	60,000	0.25%	10%

5.3 Overview of FEM Results

5.3.1 Push down stage

The moment-rotation (deflection) relationships of the two specimens from FEM results and experimental results are compared side-by-side shown in Figure 5-11, along with the process of the push stages shown in Figure 5-4. The original joint installation is at mid-point position as shown in Figure 5-4. Both the FEM and experimental findings suggest that the specimens can deflect up to approximately 4 degrees with minimal moment generation. Subsequently, the joints in both specimens continue to deflect until they achieve a total deflection of 8.36 degrees. Within this process, the spigot inside the bell joint begins to resist the bell bedding, generating a moment. Notably, the moment generated in Specimen 1 is larger than in Specimen 2, which can be attributed to the orientations of the locking segments as shown in Figure 5-4. The

specimens reached the targeted 8-degree deflection with moments of about 1033.5 kip-in and 871.4 kip-in, respectively.

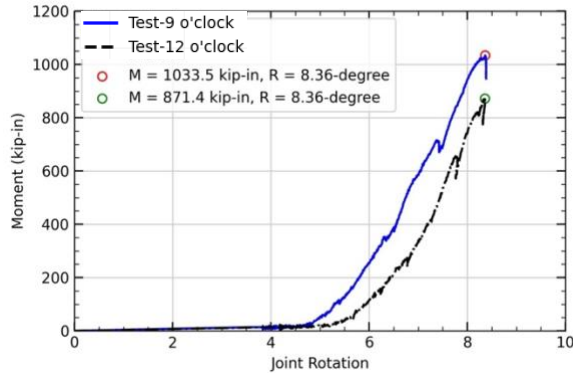


Figure 5-3 Bending moment vs. joint deflection

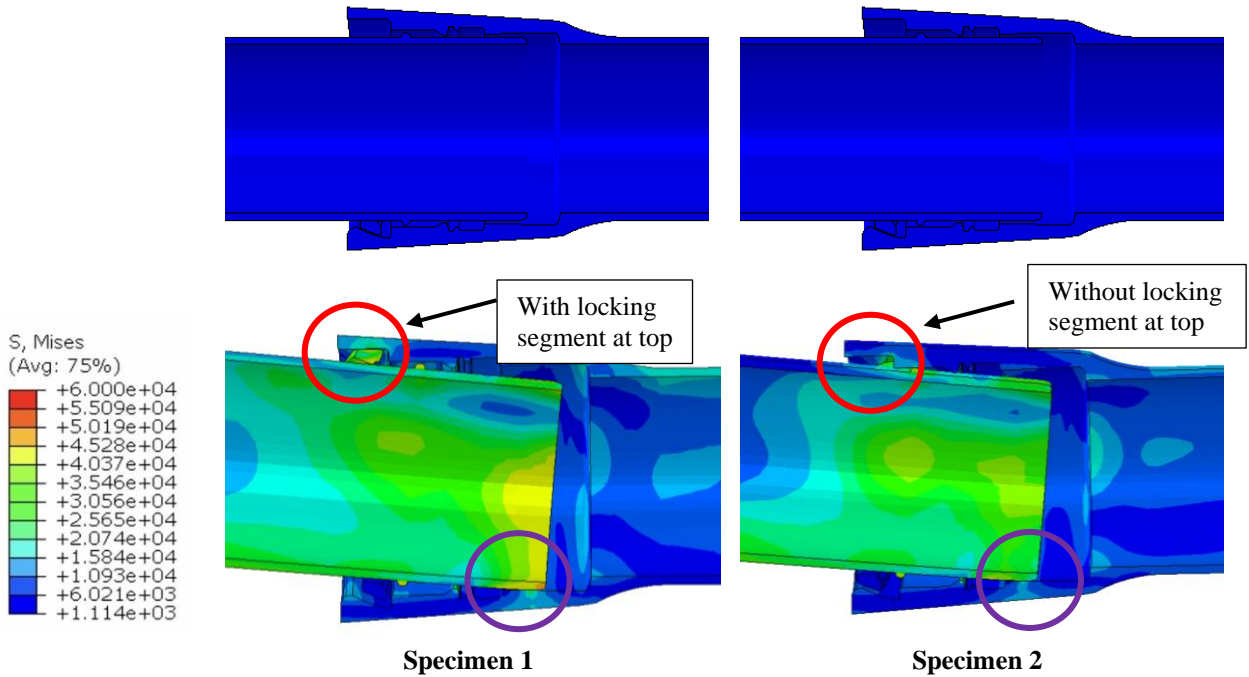
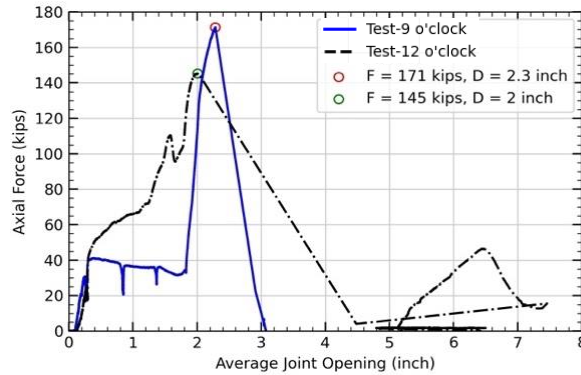


Figure 5-4 Push down stage

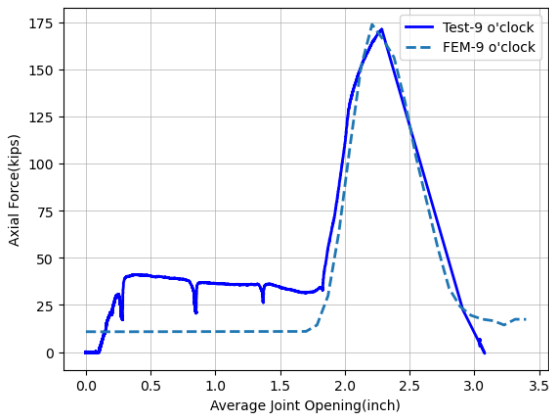
5.3.2 Pull stage

For both specimens, after the specimens reached an 8.36-degree deflection, a monotonic axial force was applied to the spigot end. During the pulling stage, since the pipelines were bent, the locking segment located at the bottom side was detached with the spigot at the bending stage, resulting in a smaller frictional force (i.e., smaller stress was developed at the bottom side). When the spigot was pulled, the spigot weld bead mainly bear against the locking segments located at top and side area of the bell. Therefore, it can be observed from both experiential and FEM results, the specimen 1 equipped with 9 o'clock orientation of locking segments have

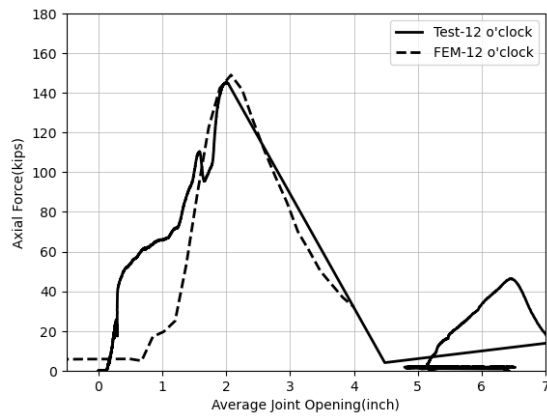
larger peak value about 171 kips than that of Specimen 2 with 145 kips. The average joint opening at maximum force is about 2.3 inches (Specimen 1) and 2 inches (Specimen 2).



(a) Test results for both specimens



(b) Comparison between test result and FEM result for Specimen 1



(c) Comparison between test result and FEM result for Specimen 2

Figure 5-5 Axial force vs. average joint opening

Figure 5-6 demonstrates the stress distribution of the bell joint when failed. As shown in the figures, the stress distributions and the deformation of the bell varies due to different locking segments orientations. The spigot weld bead in Specimens mainly bear against the locking segments located at the top and sides, resulting larger stress concentration. Besides, the deformed shapes of the bell of the two specimens are different. A symmetric deformation can be observed in Specimen 2 due to symmetrical locking segments placement circumferentially. While for Specimen 1 equipped 9 o'clock orientation, displayed an asymmetrical deformation pattern, where the bell joint squashed predominantly on one side. Because of the different force transfer and deformation mechanisms, the ultimate capacities vary between the specimens.

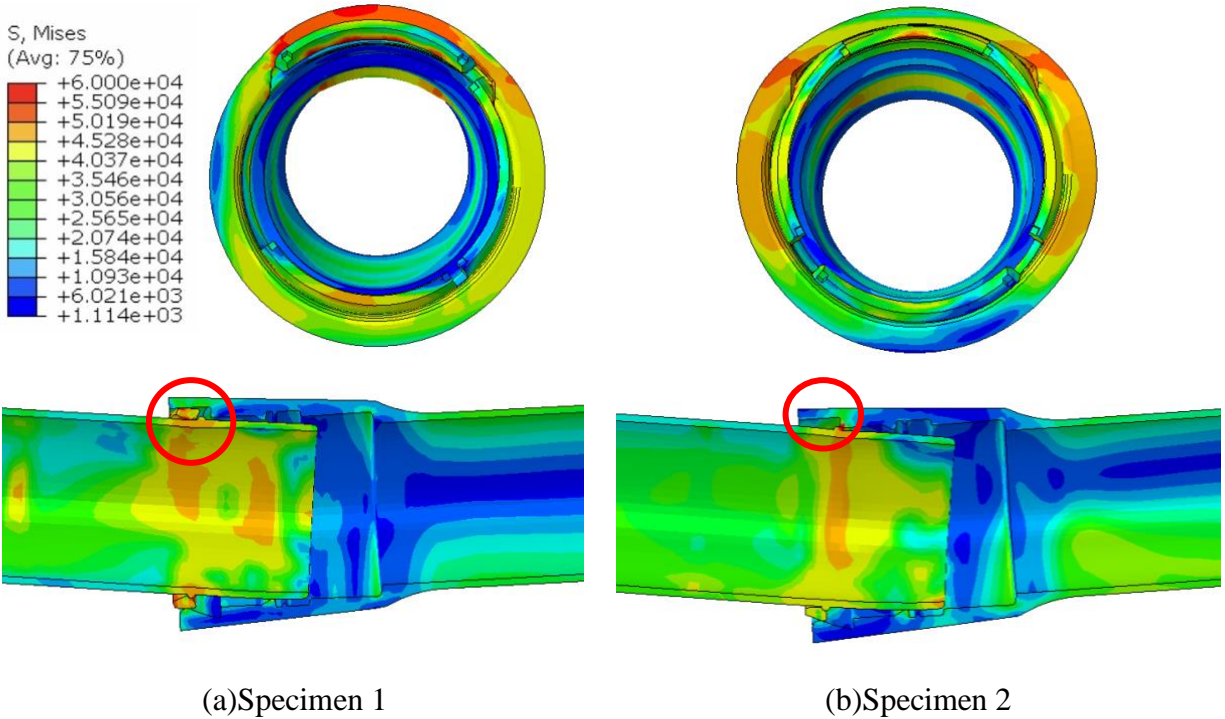


Figure 5-6 Stress distribution of bell-spigot joint

5.3.3 Failure mechanism

Figure 5-7 shows the Mises stress distribution of Specimen 1 when spigot is pulled to 2.3 inches during the Pull stage, where the red area pinpointing the vulnerable area (beyond the yield stress of 42,000 psi) around the crown of the bell joint, in alignment with this observation from experiment. This susceptibility might arise from the contact pressure between the locking segment on top and the crown of the bell. Then the crack propagated in 45-degree from side to the top area, due to the unsymmetrical orientations of locking segments. Figure 5-8 reveals that the dominant strain causing crack initiation may be attributed to the combined strains of PE11 and PE22 as well, but only one side show the grey color, representing the strain values that are over tenfold the specified yield strain 0.25%. Besides, larger hoop strain and radial strain also observed at the joint top section in Specimen 1, compared to that in Specimen 2.



Figure 5-7 Failure mode – Specimen 1

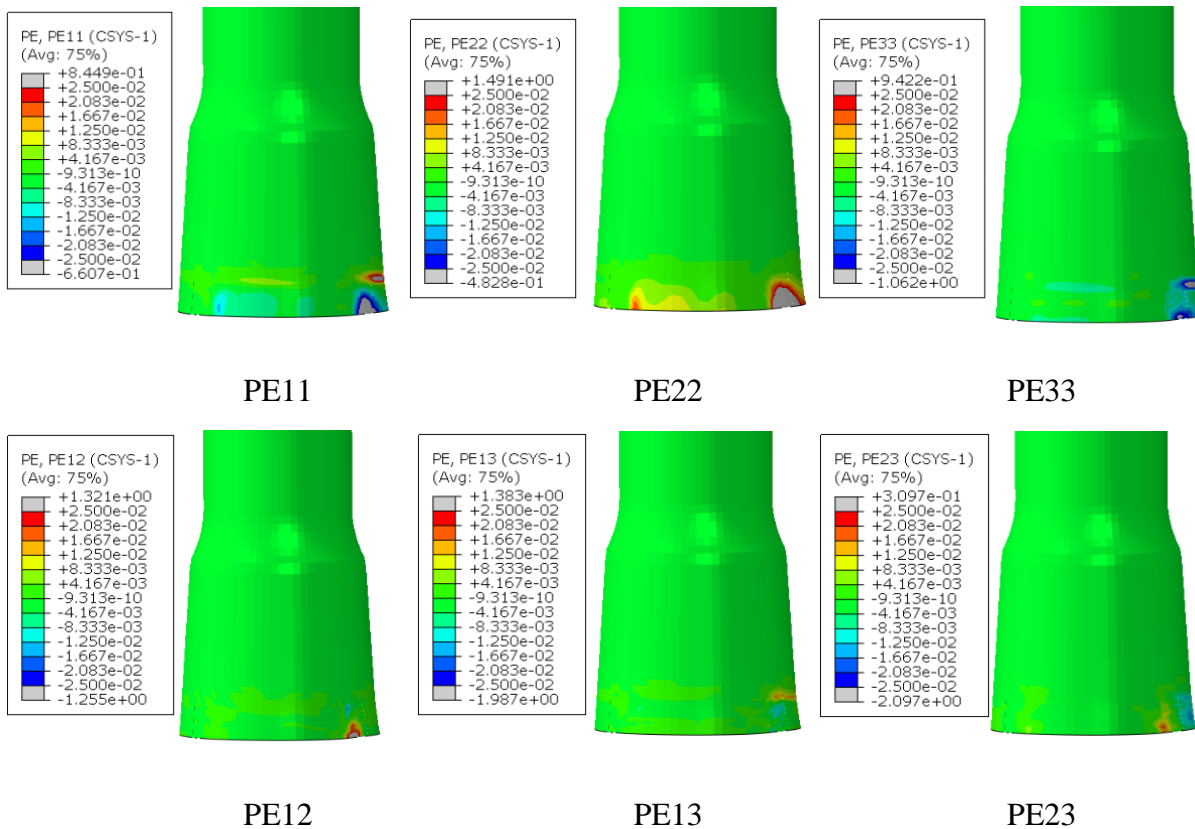


Figure 5-8 Failure mechanism – Specimen 1

In Specimen 2, when spigot is pulled to 2 inches during the Pull stage, the distribution of Mises stress suggests that a crack could initiate from the midpoint at the west and top positions same as the Specimen 1. Then progress downward to the pipe's bottom, where the boundary of the single slot and locking segments located. This pattern aligns with the failure mode evident in the test results, as depicted in Figure 5-9. In Figure 5-10, the radial strain PE11, hoop strain PE22, axial strain PE33, and shear strain PE12, PE13 and PE23 are illustrated using cylindrical coordinates. The grey regions depict strain values that are over tenfold the specified yield strain 0.25%. Observations suggest that the crack's initiation may be attributed to the combined strains of radial strain PE11, hoop strain PE22 and shear strain PE12, while its subsequent propagation is predominantly influenced by PE11 and PE33.



Figure 5-9 Failure mode – Specimen 2

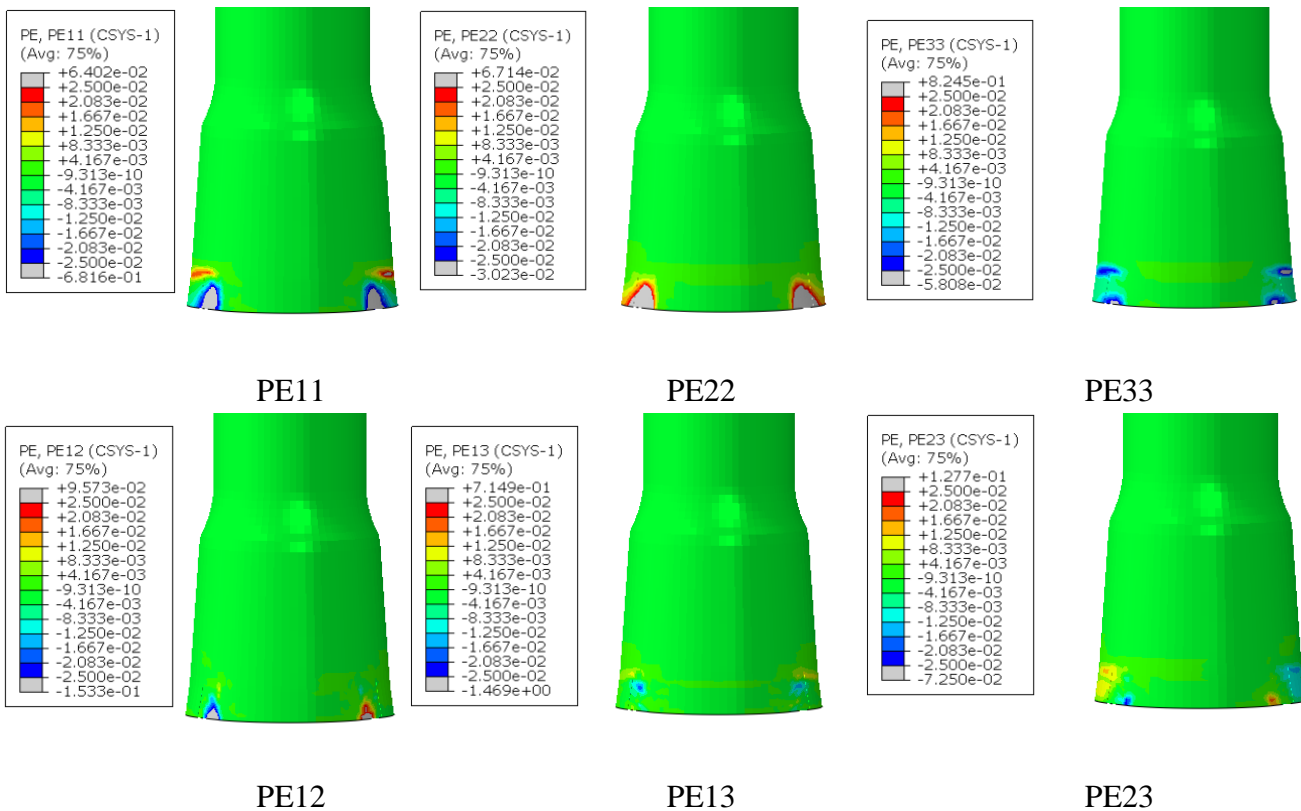


Figure 5-10 Plastic strain distribution– Specimen 2

5.4 FEM Results of Specimen 1

5.4.1 Overview

Figure 5-11 depicts a comparison of axial force-average joint opening relationships obtained from FE analysis and the experimental results of Specimen 1.

As illustrated in Figure 5-11, following the push-down stage where deflection reached approximately 8 degrees, the relationship between axial force and average joint opening was

measured during the subsequent pull stage. Both FEM and test results show that the average joint opening increases from 0 to 1.8 inches under a relatively low axial force. This corresponds to the spigot, with its weld bead, being pulled until it makes contact with the locking segments. Following this, the weld bead was beared against the locking segments until they were pulled out from the bell, reaching peak average joint opening of approximately 2.3 inches.

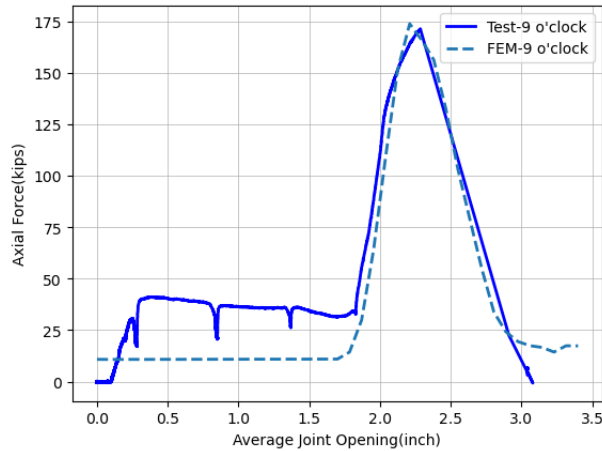


Figure 5-11 Axial force vs. average joint opening – Specimen 1

Figure 5-12 shows the Mises stress contour and deformation of the bell pipe and spigot when a 8-degree deflection was applied. Because of the bending, a significant stress concentration can be found at the bottom and top of the spigot inside the bell, where the spigot bears against the bell.

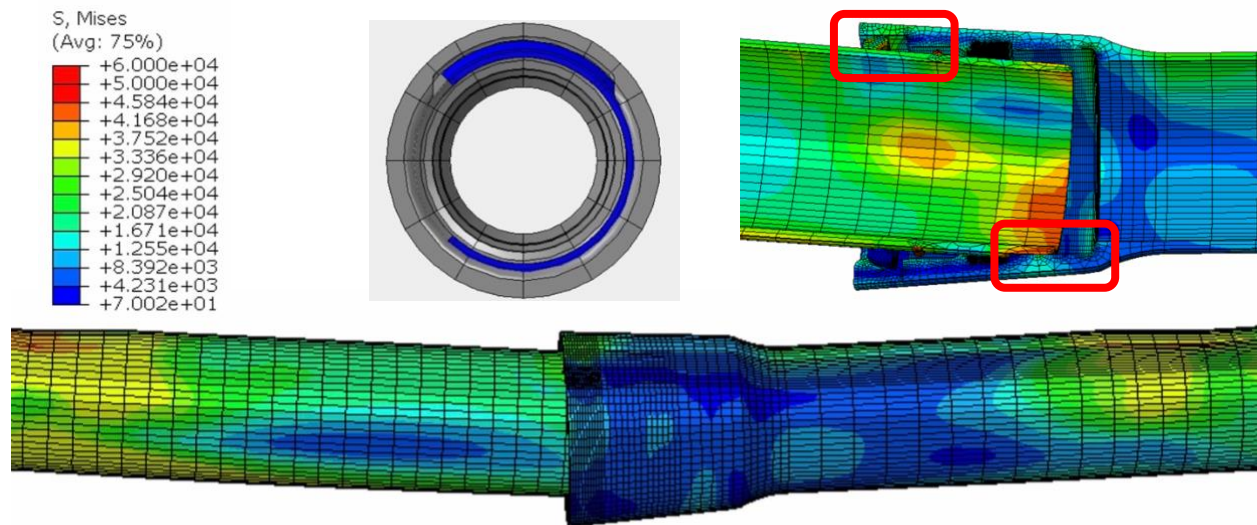


Figure 5-12 The stress contours of the deformed joint at push down stage – Specimen 1

Figure 5-13 shows the Mises stress contour and deformation of the bell pipe and spigot when the spigot is pulled to around 175 kips axial force. While being pulled, the bell joint is restrained from moving up (i.e., the deflection angle remains at least 8 degrees), and the locking

segments are allowed to slip out of the bell, the same as in the lab test. The spigot made contact with the bell invert, resulting in significant deformation at the bottom of the spigot and the crown of the bell edge.

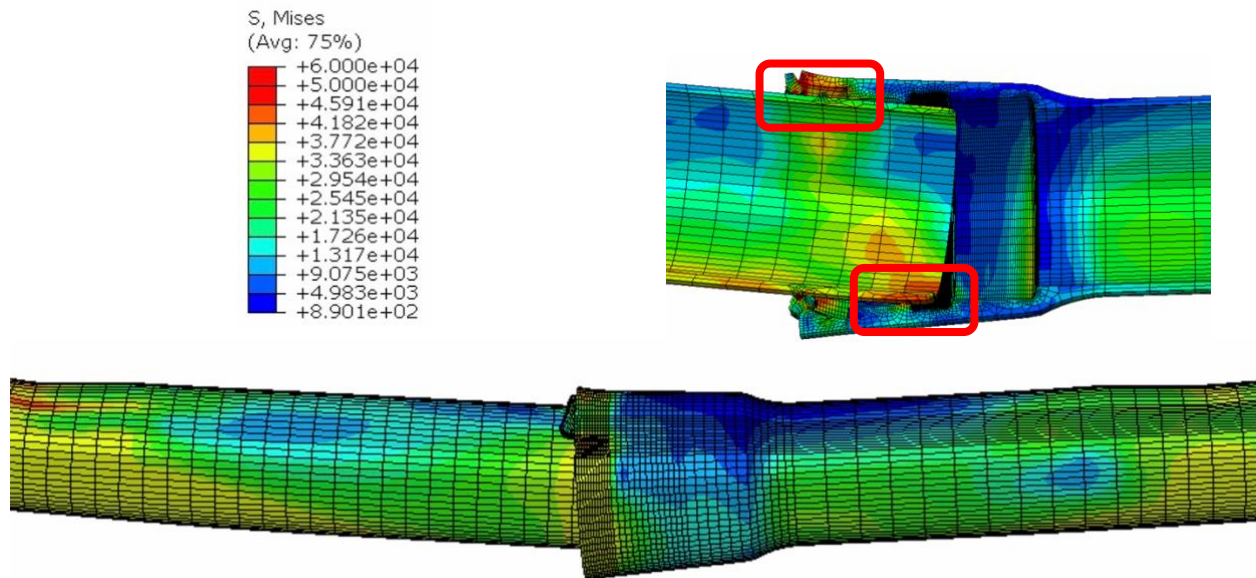


Figure 5-13 The stress contours of the deformed joint at pull stage – Specimen 1

5.4.2 Bell Deformation

Figure 5-14 shows the Mises stress distribution of the bell cross-section at the initial, push down, and pull stages. Throughout the push-down phase, the bell's shape largely remains consistent. After the locking segments are being pulled out from the bell, the bell cross-section deformed to an ellipse with irrecoverable deformation.

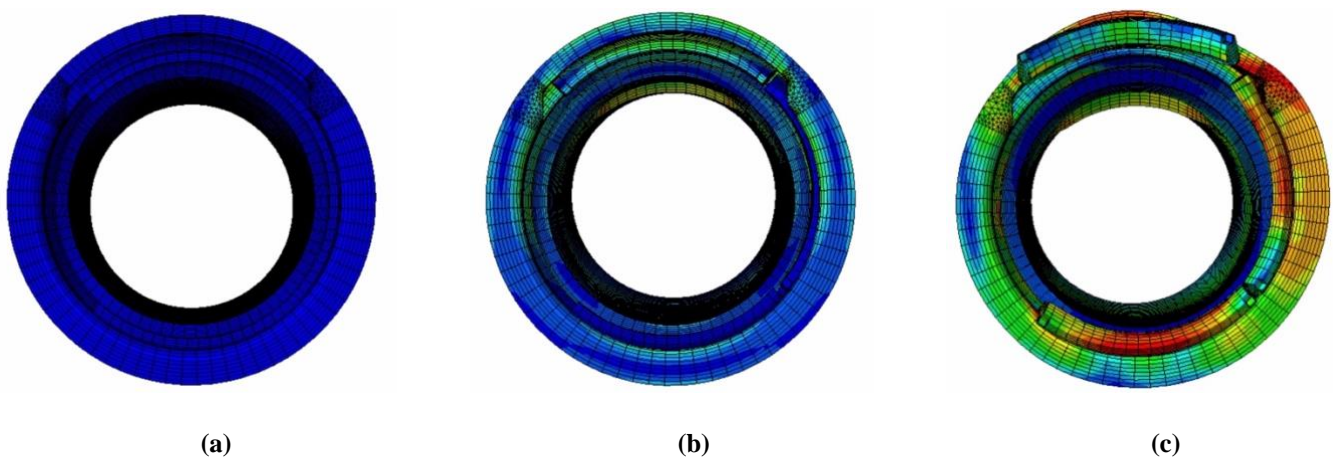


Figure 5-14 The stress contours of bell cross-section: (a) initial stage (b) push down stage (c) pull stage- Specimen 1

5.4.3 Spigot Deformation

Figure 5-15 shows the Mises stress distribution of the spigot located inside of the bell joint at the three stages. During the push down stage, the invert of the spigot shows significant concentrated stresses. The spigot cross section is squeezed into an ellipse. During the pull stage, The weld bead deforms at the area where it bears against the locking segments, as shown in Figure 5-16.

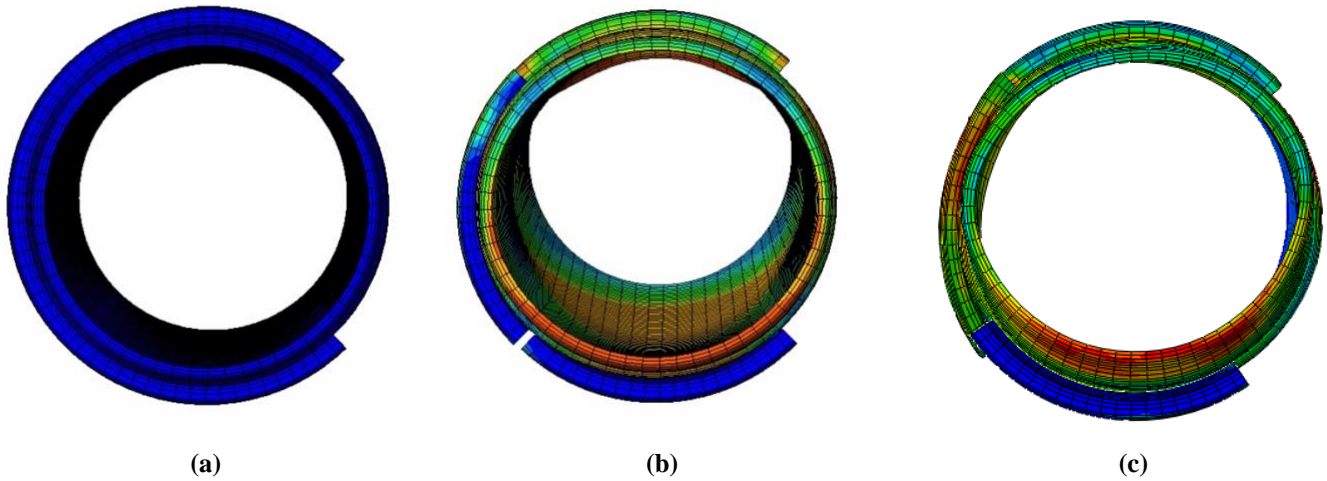


Figure 5-15 The stress contours of spigot cross-section: (a) initial stage (b) push down stage (c) pull stage – Specimen 1

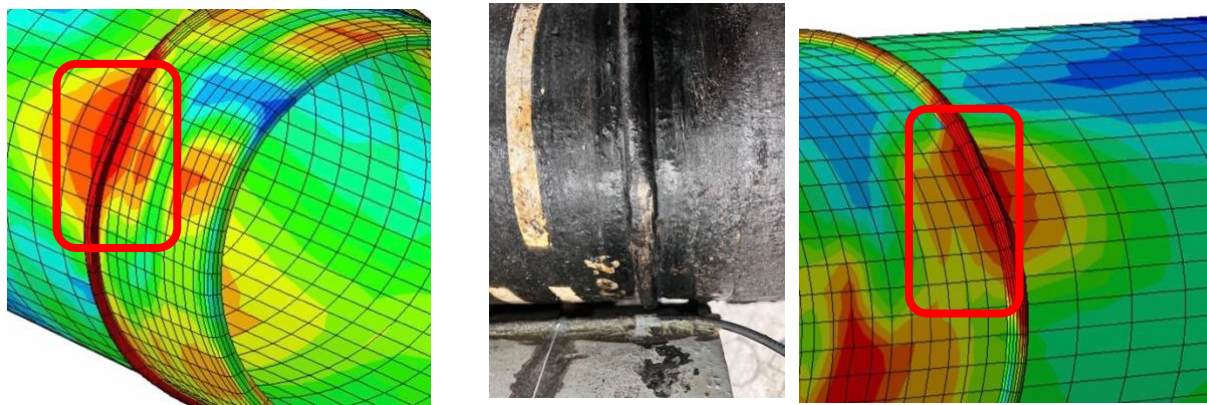


Figure 5-16 The deformation of the weld bead – Specimen 1

5.4.4 Strain Comparison between FE Analysis and Experimental Results

Figure 5-17 and Figure 5-18 show the comparison of the circumferential strain development and longitudinal strain development on the bell pipe from the FE analysis and the experiments. The FE simulation results show good agreement with the pipeline behavior observed in the lab test. The strains from Sensor 4, Sensor 5, and Sensor 6 in Figure 5-17 indicate

the circumferential strains at the bell joint (bell end, mid-point, and top of the locking segments, respectively). It can be seen that Sensor 5 experienced a larger strain distribution, due to it closed to the locking segments section where the larger concentrated stress generated.

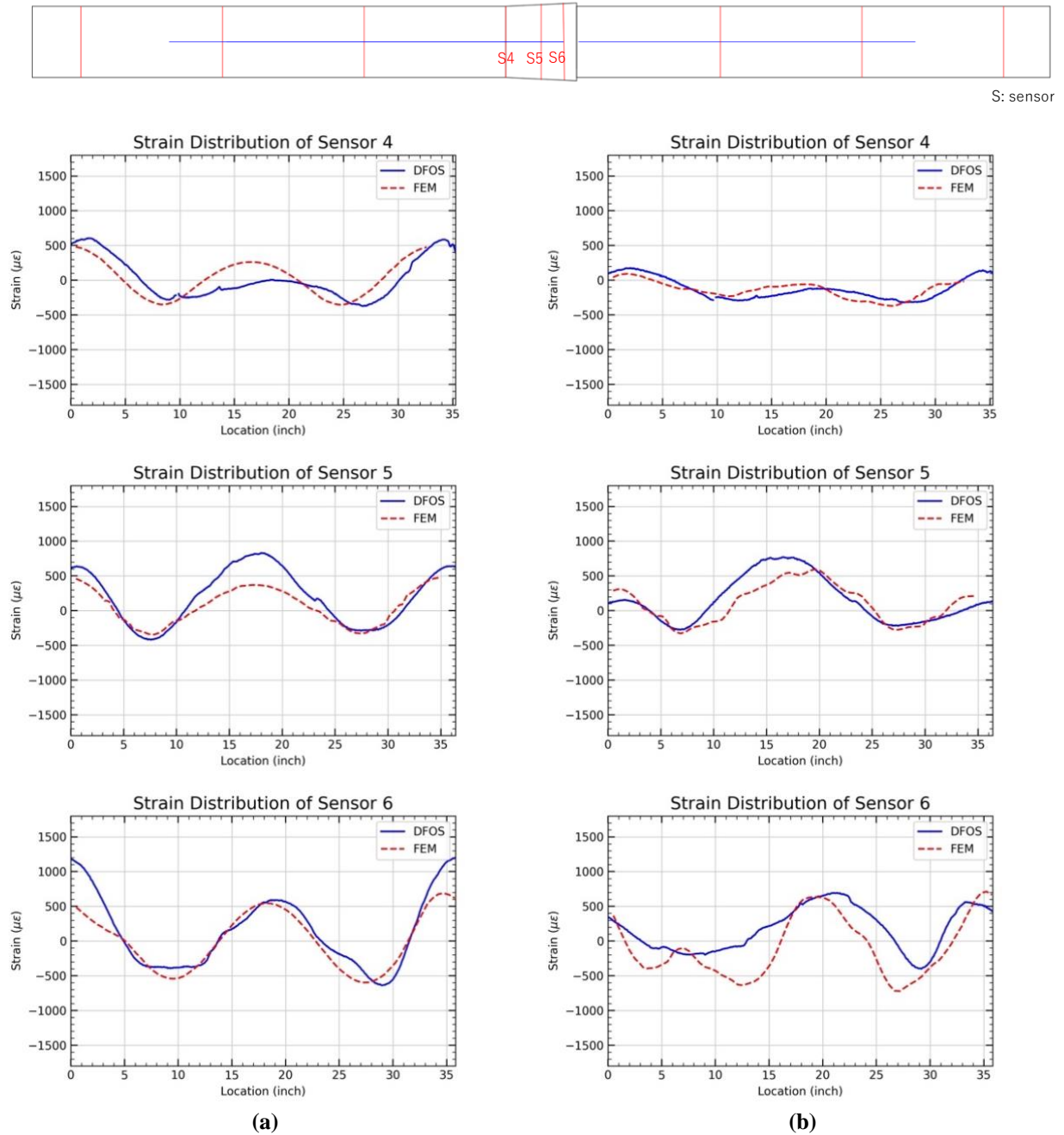
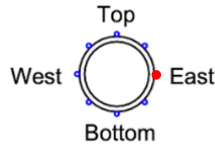


Figure 5-17 Comparison of hoop strains (a) Actuator push down (b) Pull to 2.2 inches – Specimen 1

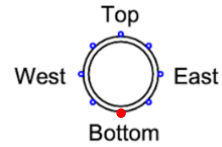
The data from Sensor 14 and Sensor 16 in Figure 5-18 correspond to the longitudinal strains at the east (3 o'clock) and bottom (6 o'clock) sides. The gaps in the DFOS data are the loading saddle locations. For side area, it can be seen that during the push down stage, tiny strain generated

as they are bear the neutral axis, where the bending strain is minimal. While during the pulling stage, the increased strain captured in the sides area due to the spigot weld bead bear against the locking segments, leading to the axial force along the pipeline.

Both FEM and experimental results show the bottom side was experiencing tensile force during both push down stage and pull stage. The strain development shows similar trend and fluctuation in bending stage and pulling stage, while the strain value in bending stage shows larger strain than that in pulling stage. During bending, the load path and stress distribution are not uniform. The bottom side, being farthest from the neutral axis, experiencing the highest tensile stress during bending. However, during pulling, the stresses are more uniformly distributed along the cross-section, potentially leading to a reduced strain.

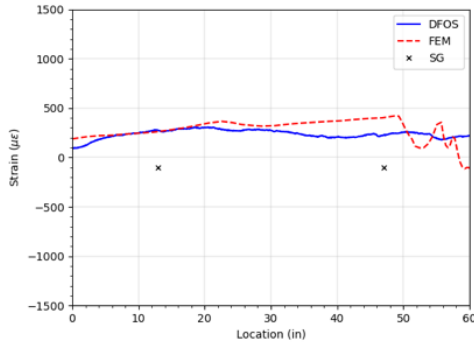


Strain Distribution of Sensor 13

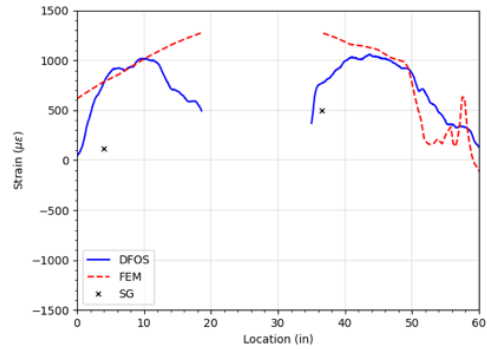


Strain Distribution of Sensor 12

(a)



Strain Distribution of Sensor 13



Strain Distribution of Sensor 12

(b)

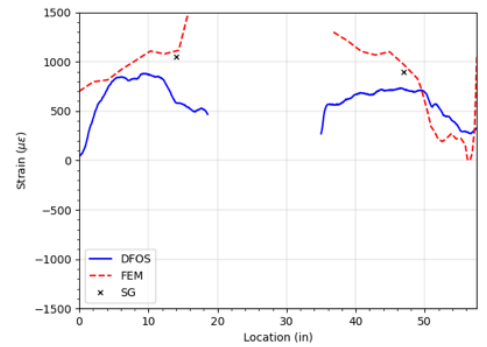
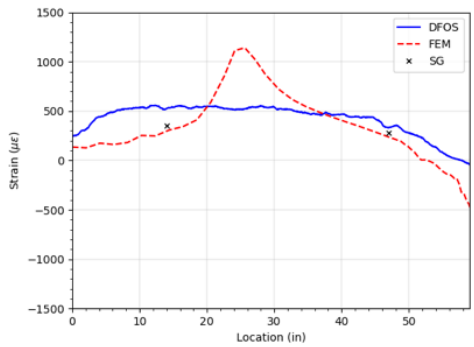


Figure 5-18 Comparison of axial strains (a) Actuator push down (b) Pull to 2.2 inches – Specimen 1

Figure 5-19 illustrates the comparison of hoop stress distributions from the bell joint’s top view during both the push down and pull stages, highlighting that the S5 and S6 areas in Specimen 1 did not exhibit significant deformation shift between the two stages.

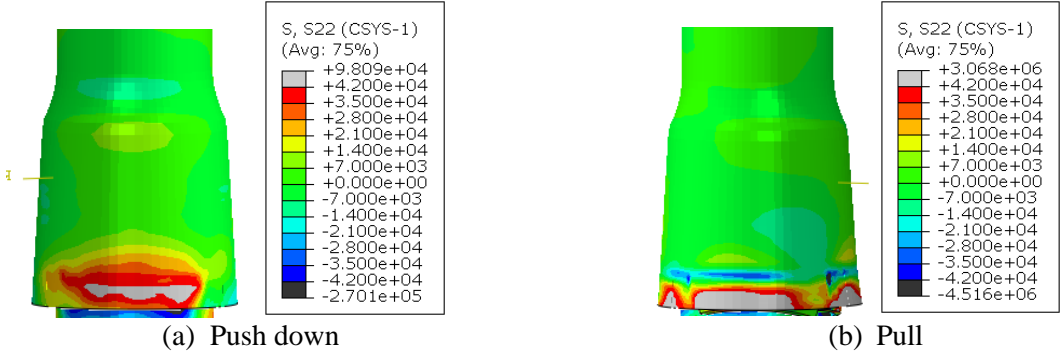


Figure 5-19 Hoop stress at push down stage and pull stage – Specimen 1

5.5 FEM Results of Specimen 2

5.5.1 Overview

Similar to Specimen 1, following the push-down stage where deflection reached approximately 8 degrees, Figure 5-20 illustrates the relationship of average joint opening and axial force between the FE analysis and experimental results. Minimal axial force is generated until the average joint opening approaches approximately 1 inch. This aligns with the phase prior to the spigot weld bead making contact with the locking segments. Subsequently, as the weld bead continues to be pulled and bears against the bell, the axial force escalates, reaching about 145 kips with an average joint opening of 2 inches.

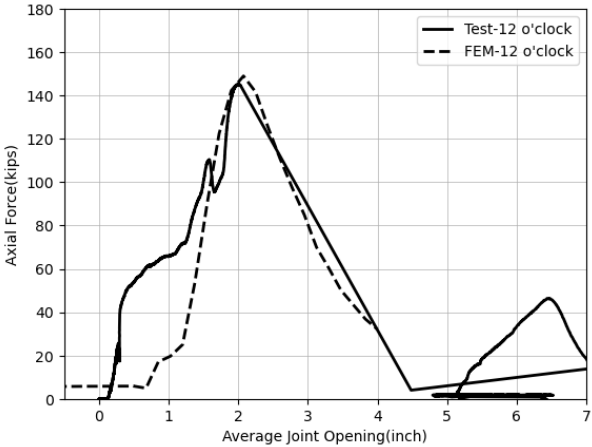


Figure 5-20 Axial force vs. average joint opening – Specimen 2

Figure 5-21 shows the Mises stress contour and deformation of the bell pipe and spigot when deflected to 8 degree. Similar to Specimen 1, concentrated stress on the bottom of the spigot can be observed.

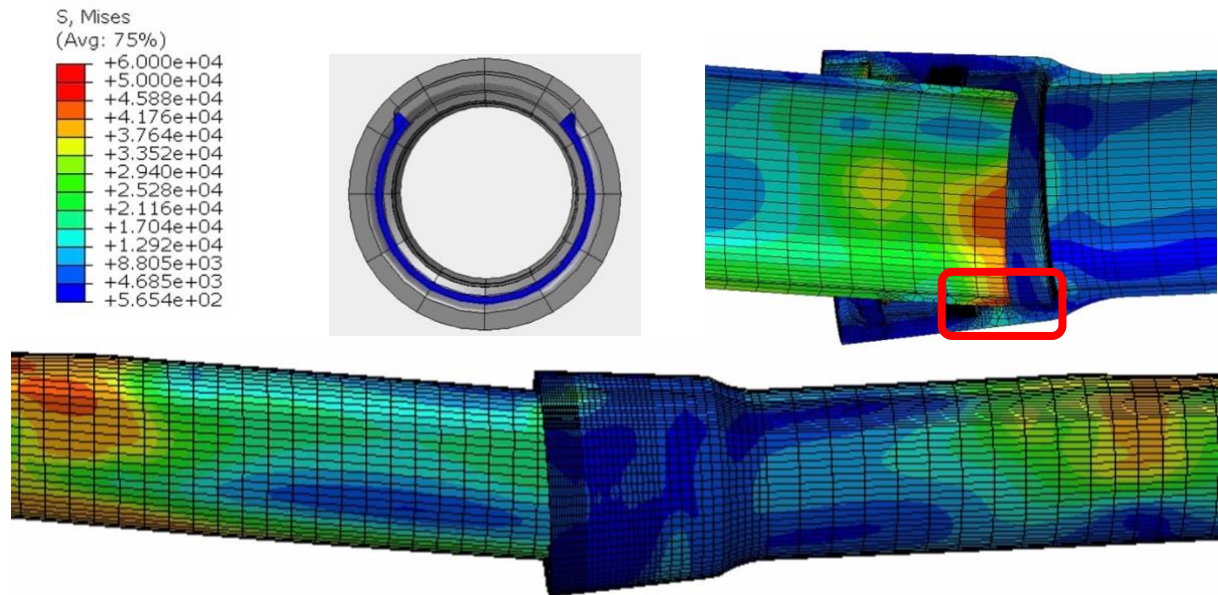


Figure 5-21 The stress contours of the deformed joint at push down stage – Specimen 2

Figure 5-22 shows the Mises stress contour and deformation of the bell-spigot joint when the spigot is pulled to around 2 inches. Similar to the boundary condition set for Specimen 1, during the Pull stage, the bell joint is restrained to 8 degrees of deflection. As shown in the figure, the spigot makes contact with the bell bedding, resulting in significant deformation of the invert of the spigot and the crown of the bell edge.

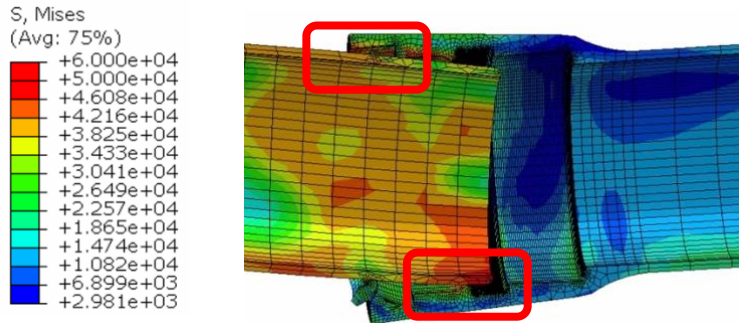


Figure 5-22 The stress contours of the deformed joint at pull stage – Specimen 2

5.5.2 Bell Deformation

Figure 5-23 shows the Mises stress distribution of the bell cross-section at the initial, actuator push down, and pull stages, respectively. Same as Specimen 1, it can be seen that, during the actuator push down stage, the shape of the bell merely changed. The bell cross-section deformed while being pulled. Unlike Specimen 1, which shows the non-symmetric stress and deformation distribution, the stress and deformation of Specimen 2 are symmetric due to the symmetric position of three locking segments.

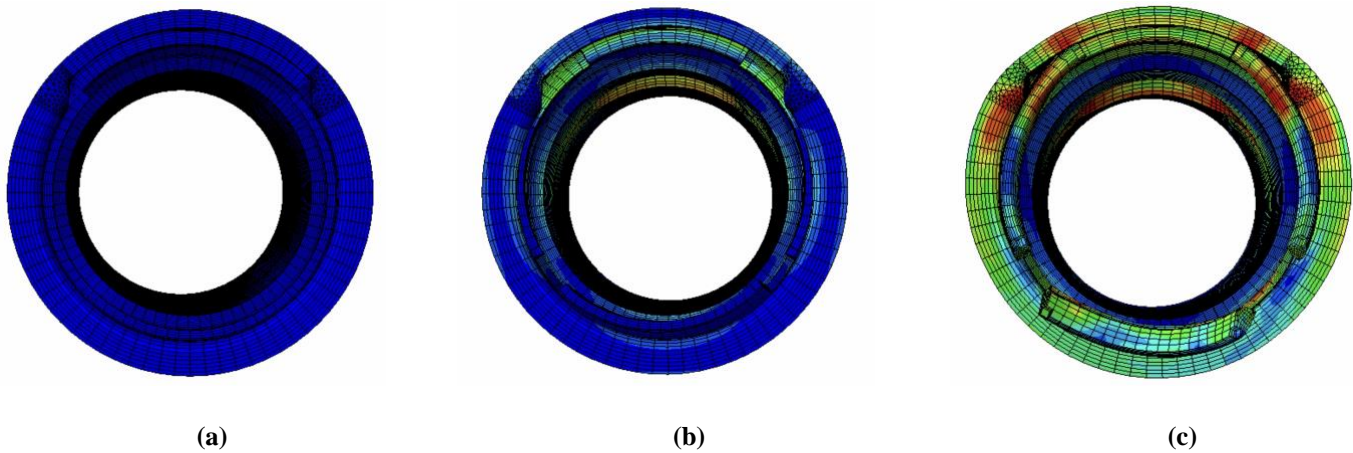
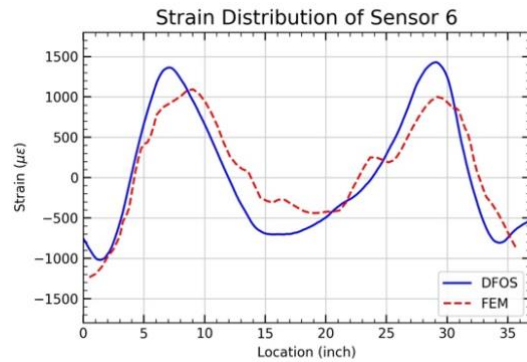
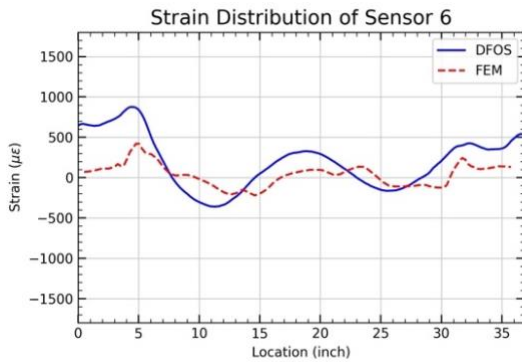
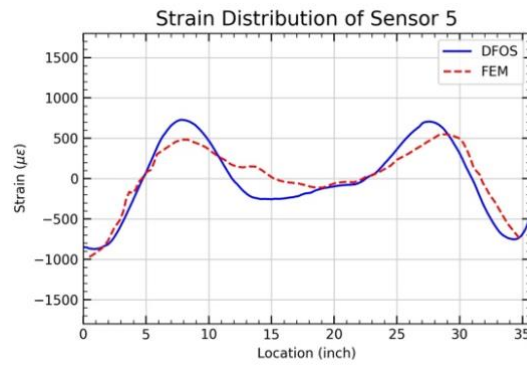
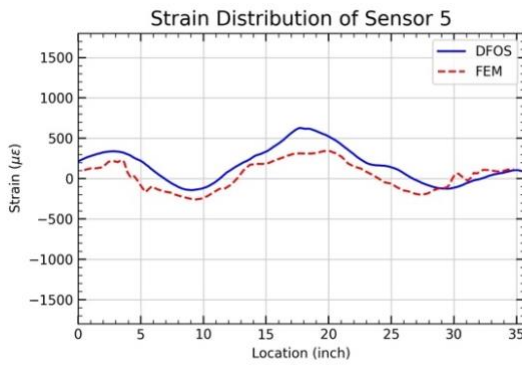
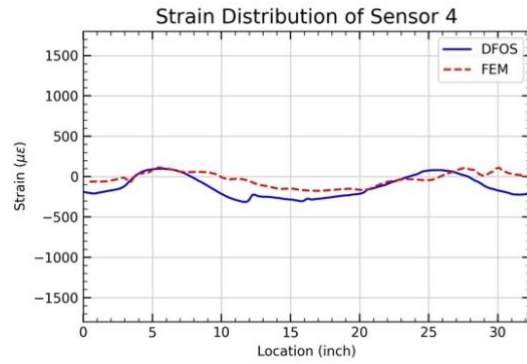
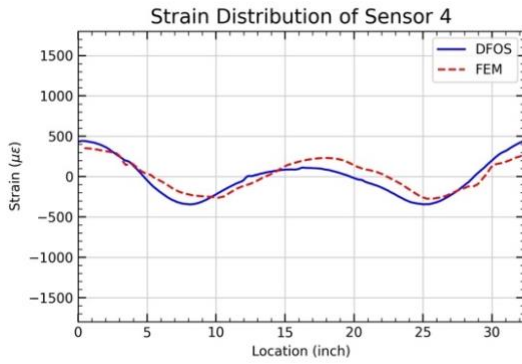
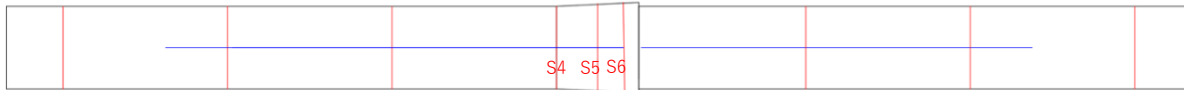


Figure 5-23 The stress contours of bell cross-section: (a) initial stage (b) push down stage (c) pull stage – Specimen 2

5.5.3 Strain Comparison between FE Analysis and Experimental Results

Figure 5-24 and Figure 5-25 show the comparison of the circumferential strain development and longitudinal strain development on the bell pipe from the FE analysis and the experiments in Specimen 2. Similarly, the readings from Sensors 4, 5, and 6 represent the circumferential strain distribution at the bell joint. Meanwhile, the data from Sensors 14 and 16 provide insight into the longitudinal strain distribution at the east (3 o’clock) and bottom (6 o’clock) of the bell pipe. Notably, Sensors 5 and 6 record a greater hoop strain when pulled to 2.2 inches compared to the push down stage, whereas Sensors 14 and 16 exhibit comparable longitudinal strain patterns. These observations suggest that the axial force primarily drives the hoop strain development relative to bending. Moreover, the orientation of the locking segments appears to impact the circumferential strain distributions more significantly than the axial strain during the pulling phase.



(a)

(b)

Figure 5-24 Comparison of hoop strains (a) actuator push down (b) pull to 2.2 inches – Specimen 2

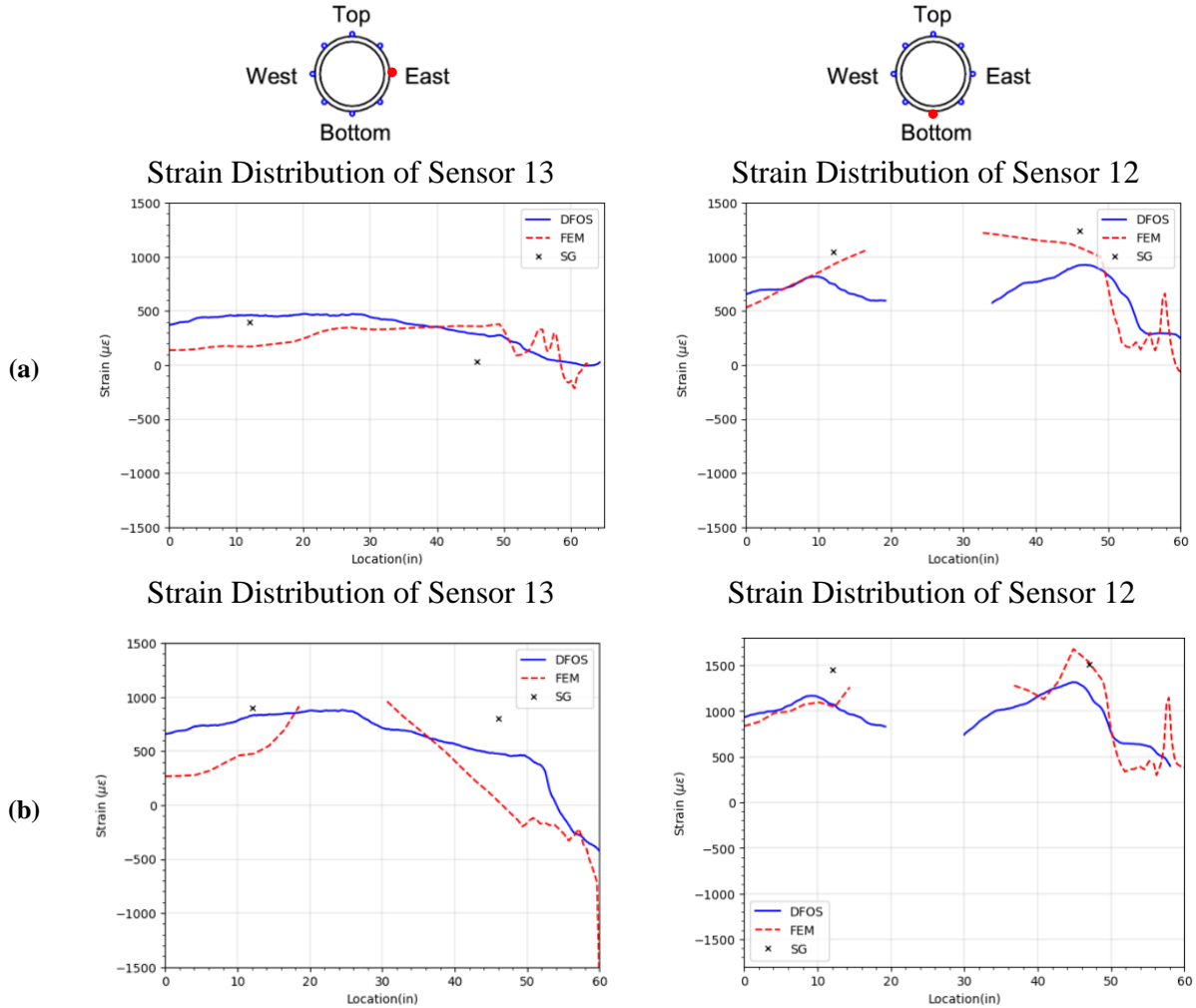


Figure 5-25 Comparison of axial strains (a) actuator push down (b) pull to 2.2 inches – Specimen 2

Figure 5-26 compares the hoop stress distributions at the bell joint's top view during both the push down and pull stages. It clearly shows that the hoop stress in the area around S5 and S6 shifted from tension during the push down stage to compressive stress during the pull stage. Simultaneously, the hoop stress on the sides, which was minimal during the push down stage, exhibited increased tensile stress during the pull stage.

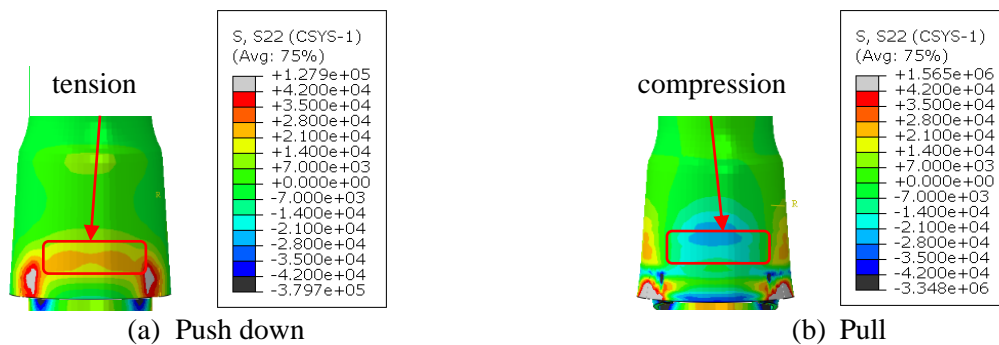


Figure 5-26 Hoop stress at push down stage and pull stage – Specimen 2

6. Conclusion

This report describes the results of the experiments and FE analysis focused on the performance of bell-spigot joint under biaxial tension forces (combined bending and tension force). The performance of two pipelines with different orientations of locking segment is discussed. The joint was initially installed at the mid-point location.

During the push-down stage, both experimental and FEM results demonstrate that the specimens were deflected to an 8-degree angle. The concentrated stress area was identified inside the bell joint, situated directly beneath where the bell mouth contacts the crown and invert of the spigot. In the pull stage, while maintaining this 8-degree deflection, the spigot initially moved about 1 inch with minimal axial force until it contacted the locking segments. Subsequently, the spigot weld bead began to exert pressure against the locking segment, attempting to pull out from the bell. The results recorded that the Specimen 1 failed at an applied axial force of 145 kips and with an average joint opening of 2 inches, whereas Specimen 2 failed at an applied axial force of 171 kips and with an average joint opening of 2.3 degrees.

In both specimens, a crack was initiated at the intersection between the locking segments and the single slot at the bell. However, the crack propagation patterns differed between them; the crack spread circumferentially in Specimen 1, whereas diagonal crack propagation towards the bell top was observed in Specimen 2. This difference is attributed to the asymmetrically placed locking segments in Specimen 2, which induced additional hoop and shear stresses at the bell top.

In this study, 3D FE models were calibrated with full-scale experiments and were further adopted to analyze the impact of the orientations of the locking segments. The strain distribution and failure patterns matched well between the experimental results obtained from the DFOSs and the simulation, indicating that the proposed FE model can reasonably predict pipe behavior under the biaxial-tension conditions. The developed FE model can be used for future parametric studies and as a guide for improved pipe design.

7. Reference

- U.S. Pipe. (2020). TR XTREME [Brochure]. https://www.uspipe.com/wp-content/uploads/2020/12/USP_TR_XTREME_Brochure_03-03-2020-for-web.pdf?fbclid=IwAR2n950mDSY8OQ39WFCoVzV8WWoNmk_ae88eCPNjQym1okpuRK7mLp6absE
- LUNA inc. (2022). ODiSI 6000 Series Optical Distributed Sensor Interrogators. Retrieved from <https://lunainc.com/sites/default/files/assets/files/data-sheet/Luna%20ODiSI%206000%20Data%20Sheet.pdf>
- Wu, J., Jiang, H., Su, J., Shi, B., Jiang, Y., & Gu, K. (2015). Application of distributed fiber optic sensing technique in land subsidence monitoring. *Journal of Civil Structural Health Monitoring*, 5(5), 587-597.
- ABAQUS (2020). <https://www.3ds.com/support/hardware-and-software/simulia-system-information/abaqus-2020/>.
- The Engineering ToolBox. (2004). <https://www.engineeringtoolbox.com/index.html>

Appendix A: Distributed Fiber Optic Sensing

Using the physical properties of light, fiber-optic sensing can detect changes in temperature, strain, and other parameters when light travels along a fiber, which uses fiber-optic cables as sensors and can measure over long distances at 100 to 1000s of points on a single cable or multiplexed cables depending on the analyzer used. Compared to the other sensing technologies, fiber-optic sensing has distinct advantages such as small size, light weight, and strong resistance to corrosion and water. Distributed fiber optic sensing consists of two main components, an analyzer, and fiber-optic cables. LUNA ODiSI 6000 series interrogator was used as the analyzer, and NanZee Sensing Technology Co manufactured the fiber-optic cables in the experiments.

LUNA Interrogator




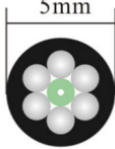
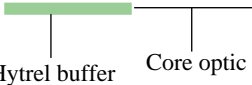
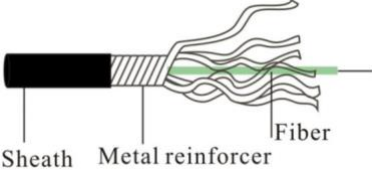
Figure A-1. LUNA ODiSI 6000 Series optical distributed sensor interrogator (LUNA, 2022)

LUNA ODiSI 6104 is an optical distributed sensor interrogator that can provide thousands of strain or temperature measurements per meter of a single high-definition fiber sensor. High-Definition H.D.D) Sensors - Strain & Temperature (HD-SC) temperature sensors utilize an advanced interrogation mode of the ODiSI to increase the accuracy of measurements when the sensors are subjected to strain, such as in embedded and surface-mount installations. It can achieve a sensor gauge pitch (the distance between two measurement points) as small as 0.65 mm, a sensor length of up to 50 m, and a measurement rate of up to 250 Hz with an accuracy of less than ± 1 microstrain.

Fiber-optic Cable

Two types of fiber optic cables manufactured by NanZee Sensing Technology Co. were used; (a) 5 mm diameter armored cable (NanZee 5mm) and (b) 0.9 mm diameter cable (NanZee 0.9mm). Table 3-2 lists the information on the cables. The difference between the two cables is the thickness and material of the coating. NanZee, a 5mm cable, provides a sheath layer and steel reinforcement, resulting in better protection to the optical core; hence, it can be used for the actual field application. The coating of NanZee 0.9mm cable is thinner than NanZee 5mm cable. NanZee 0.9mm cable has less protection, but a more sensitive strain response is achieved.

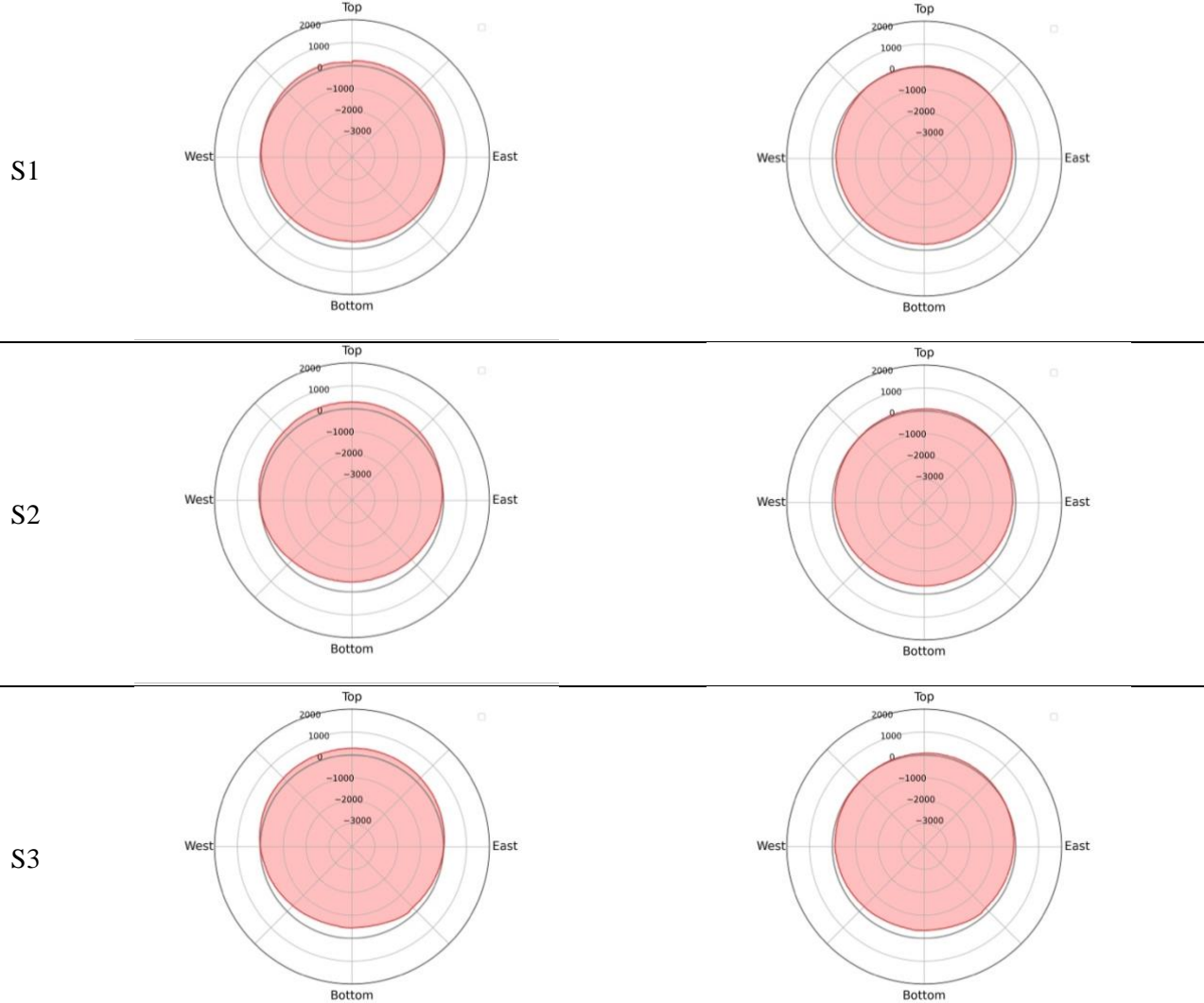
Table A-1 Schematic illustration of the selected strain sensor cable (Wu et al., 2015)

Brand	NanZee Sensing Technology Co.	NanZee Sensing Technology Co.
Model	Nzs-DSS-C07	Nzs-DSS-C02
Cross section	 <p style="text-align: center;">0.9mm</p>	 <p style="text-align: center;">5mm</p>
Side view	 <p style="text-align: center;">Hytrel buffer Core optic</p>	 <p style="text-align: center;">Sheath Metal reinforcer Fiber</p>

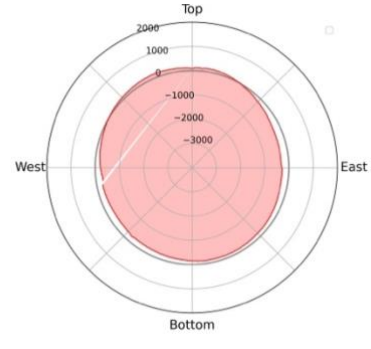
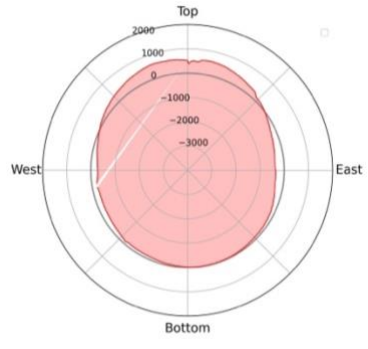
Appendix B: Distributed Fiber Optic Sensors Result

The results from the distributed fiber optic sensors are demonstrated herein. Plot (a) shows the strain distribution of the beginning state of the Pulling stage (i.e., the specimen first reaches the maximum rotation, 8.3 degrees). Plot (b) shows the strain distribution under 140 kips axial force condition.

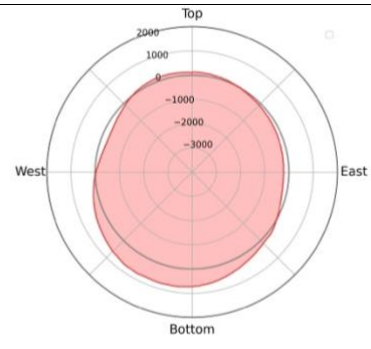
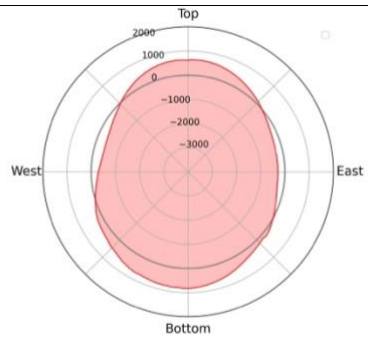
(a) Specimen 1



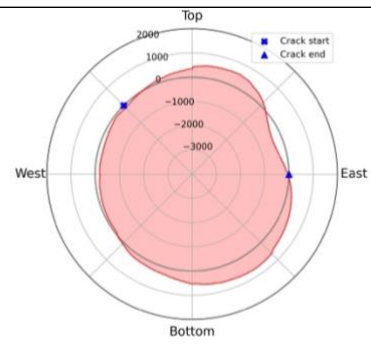
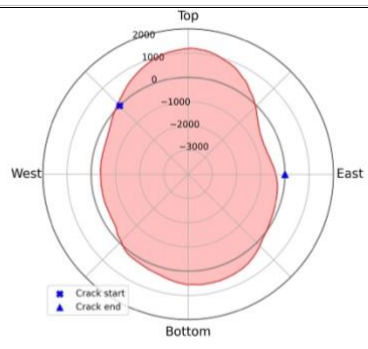
S4



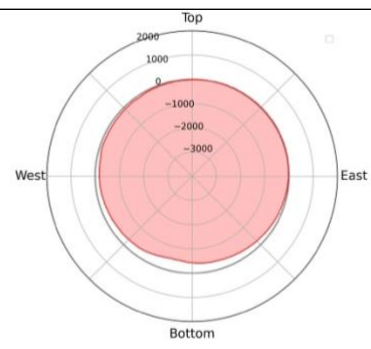
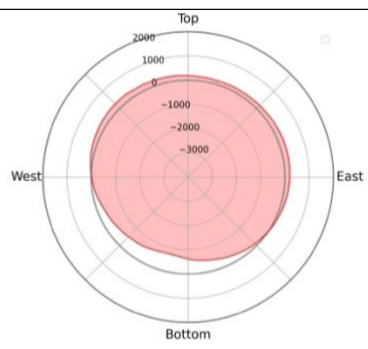
S5



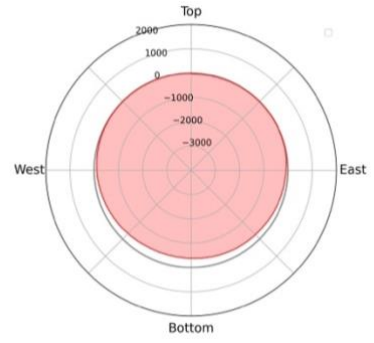
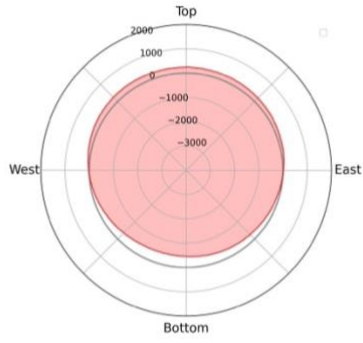
S6



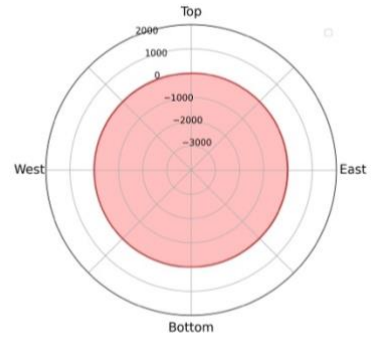
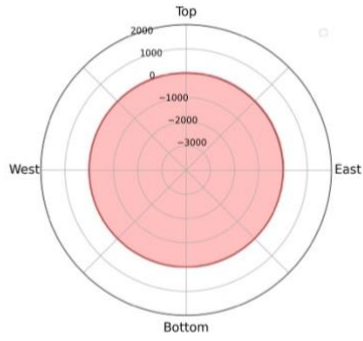
S7



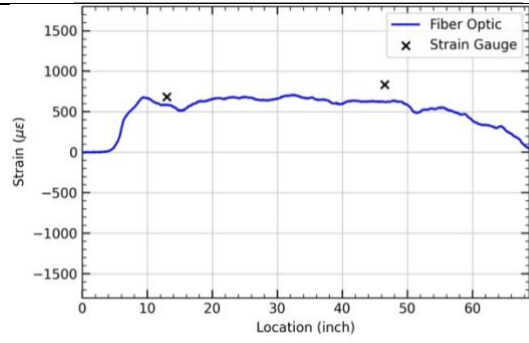
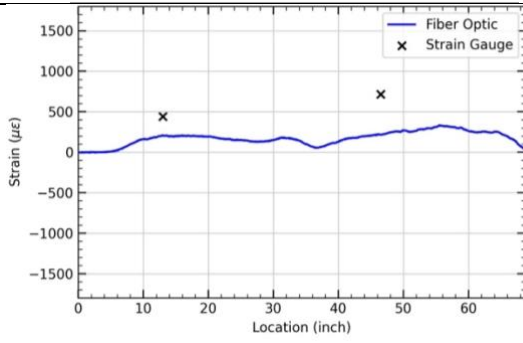
S8



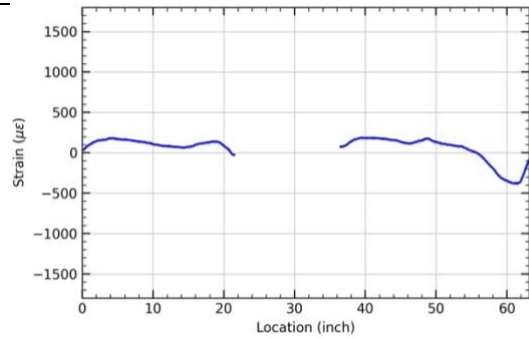
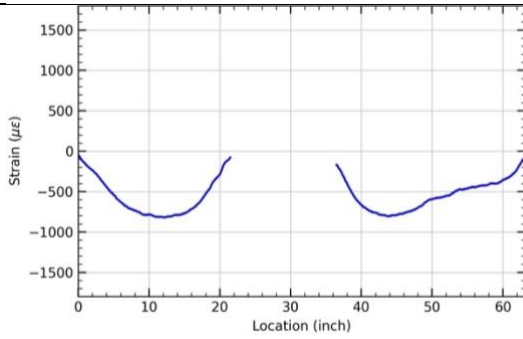
S9



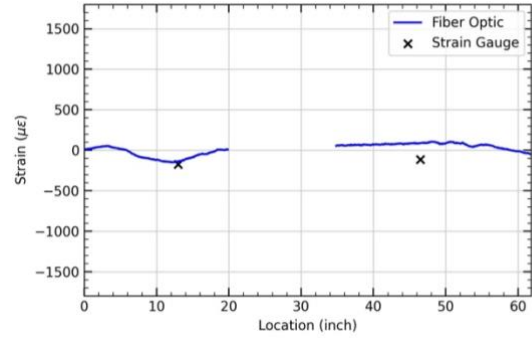
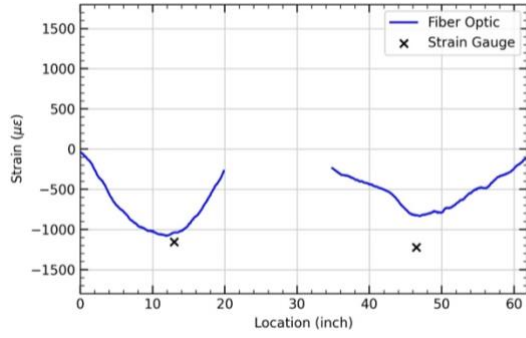
S10



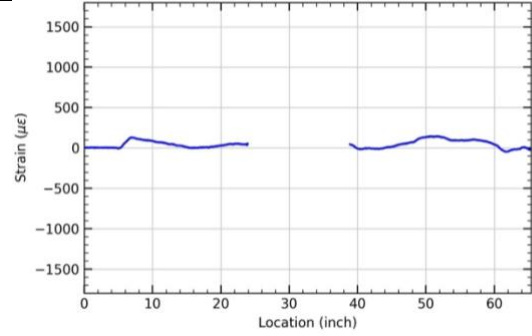
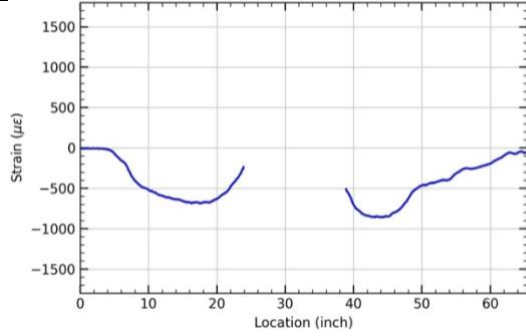
S11



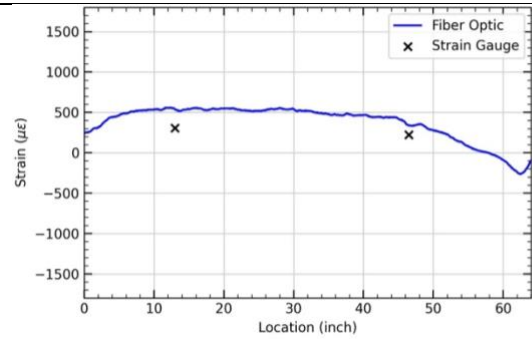
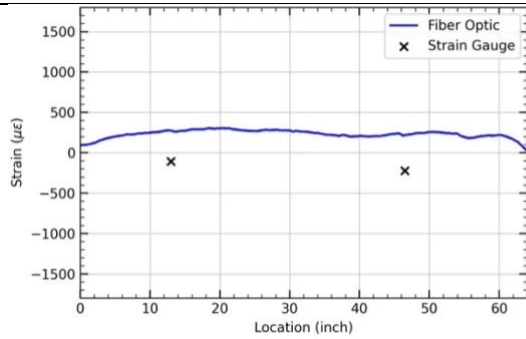
S12



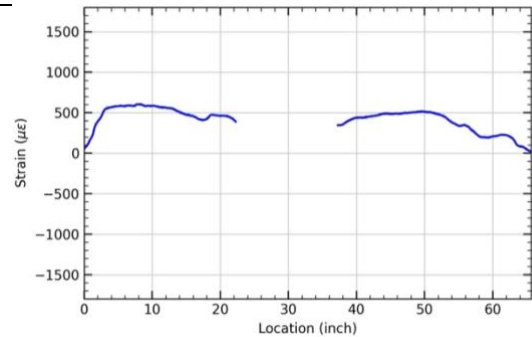
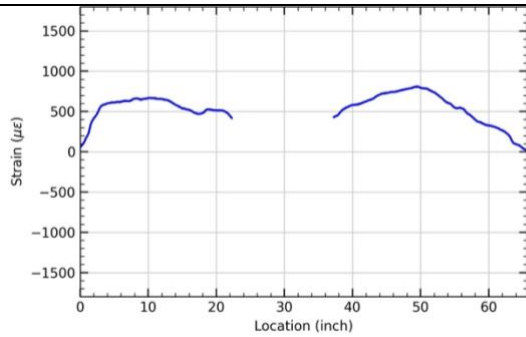
S13



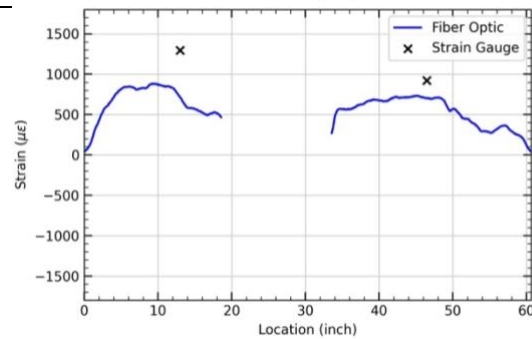
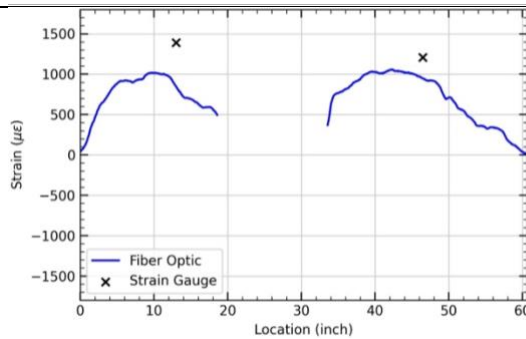
S14



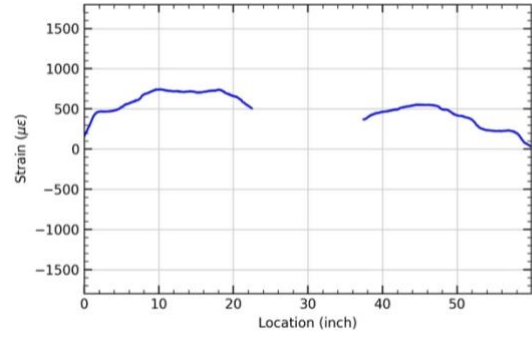
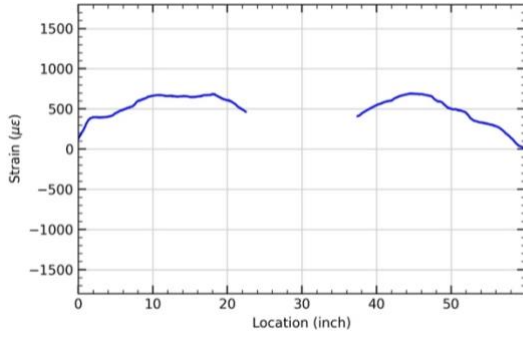
S15



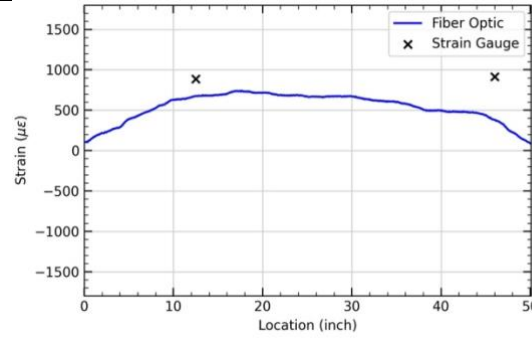
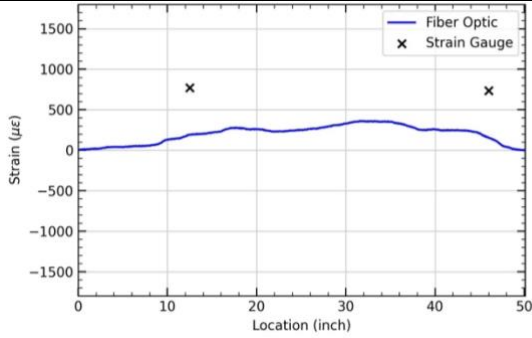
S16



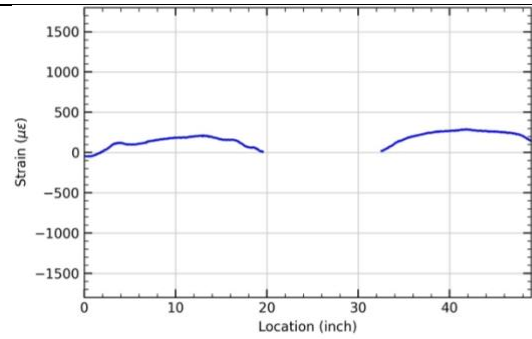
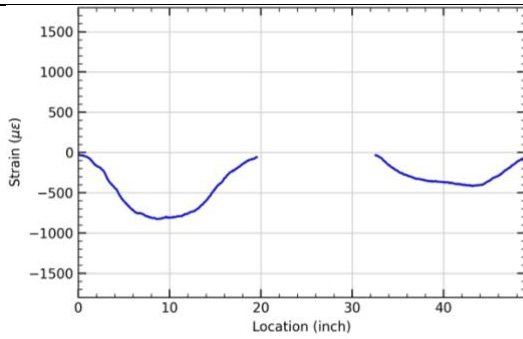
S17



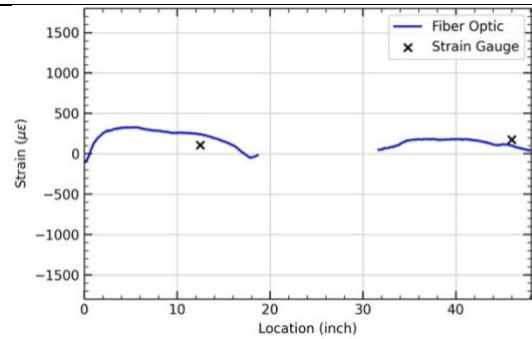
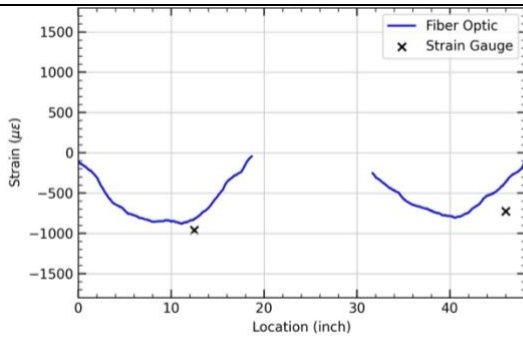
S18



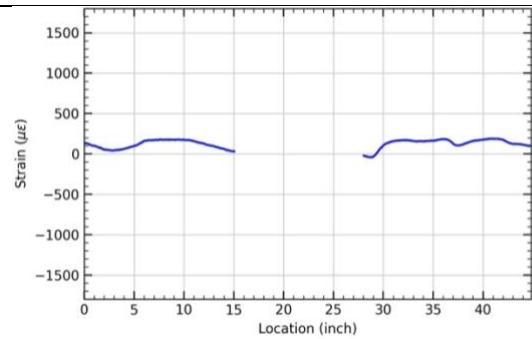
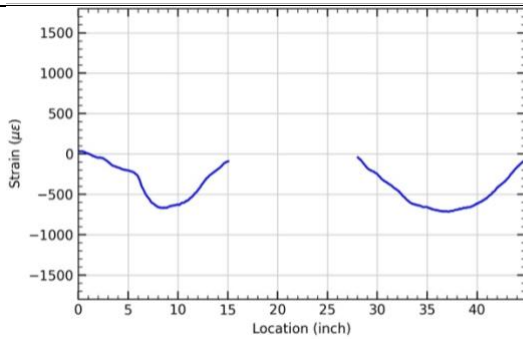
S19



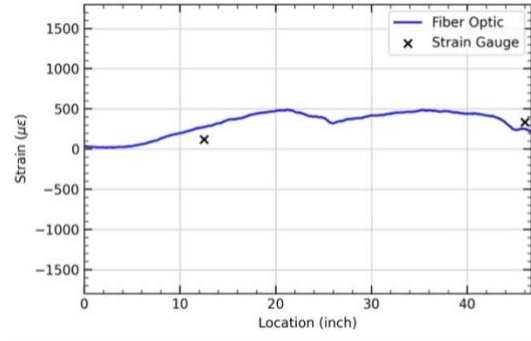
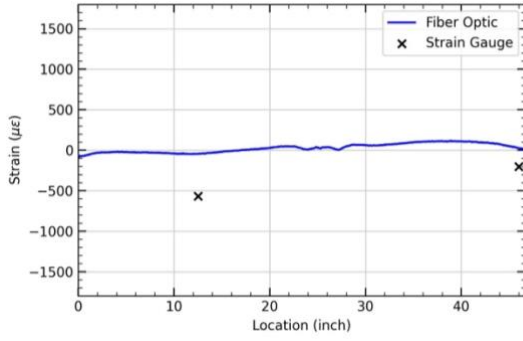
S20



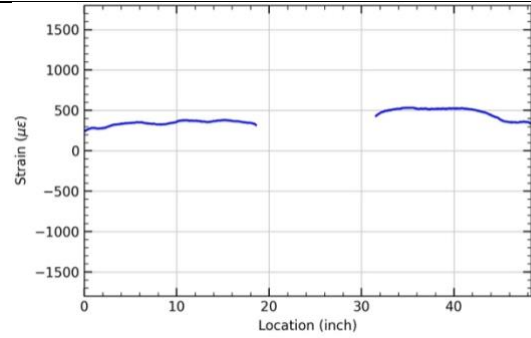
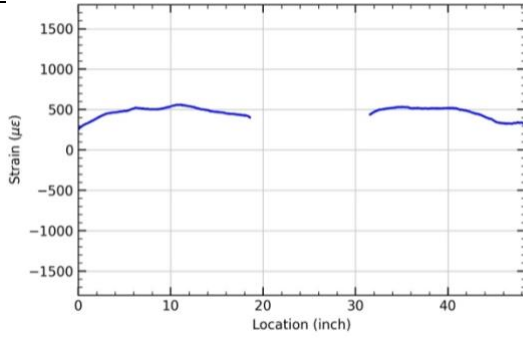
S21



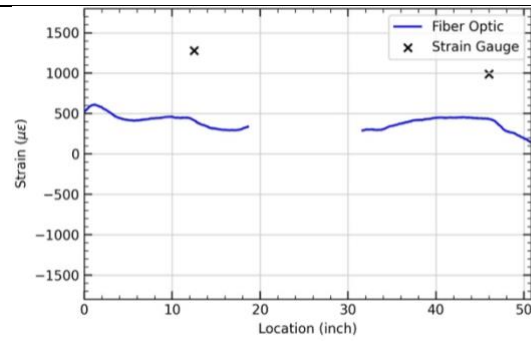
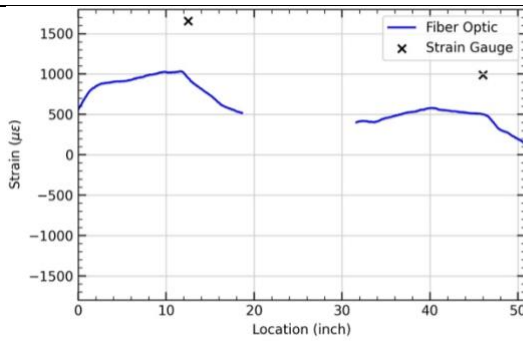
S22



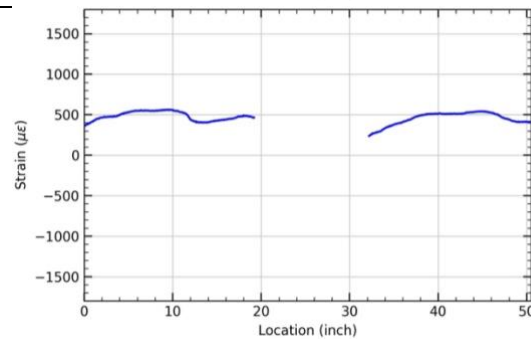
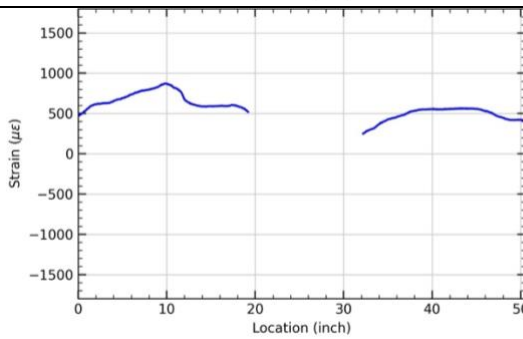
S23



S24



S25

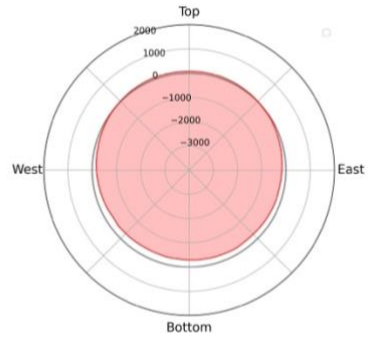
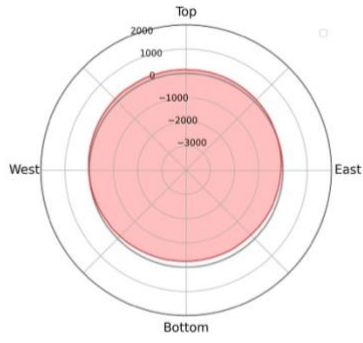


(a) Strain distribution under 8.3-degree rotation condition

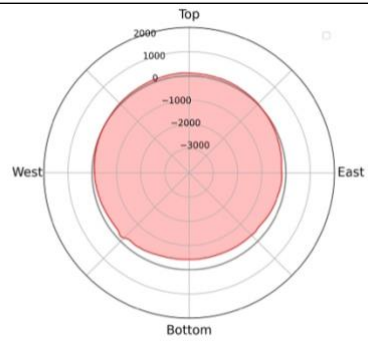
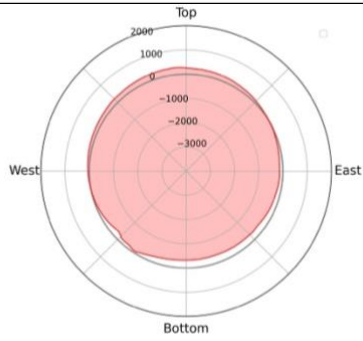
(b) Strain distribution under 140 kips axial force condition

(b) Specimen 2

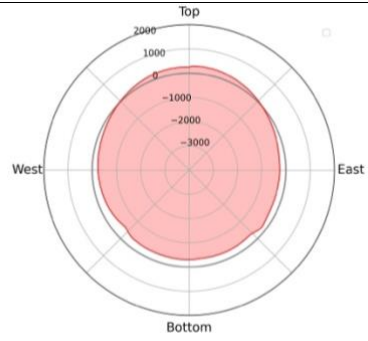
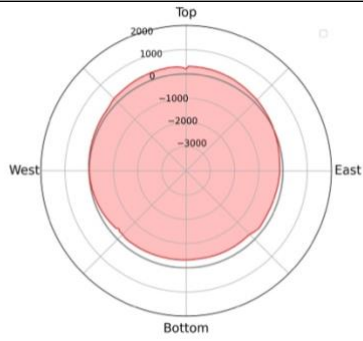
S1



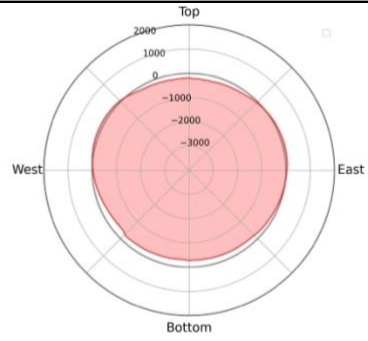
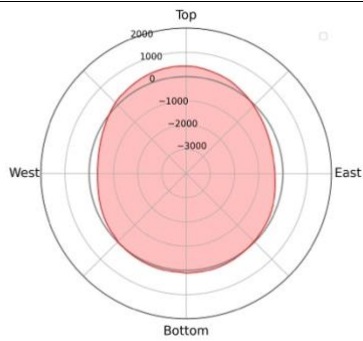
S2



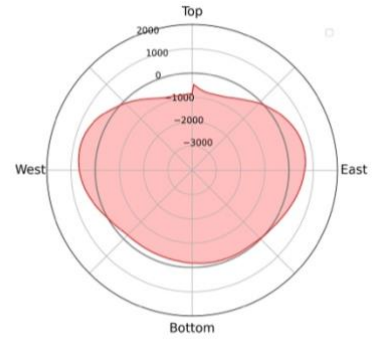
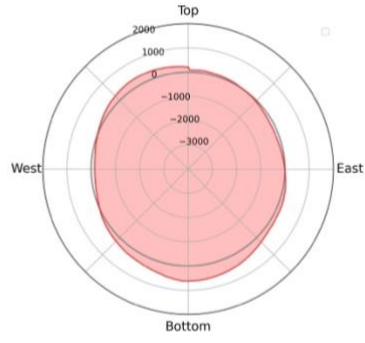
S3



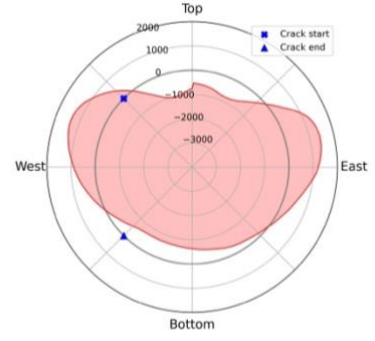
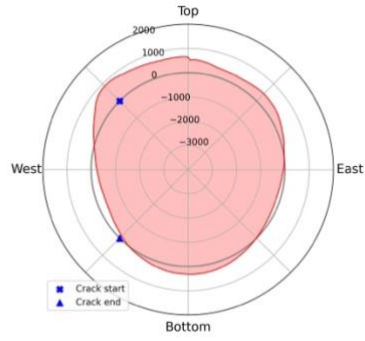
S4



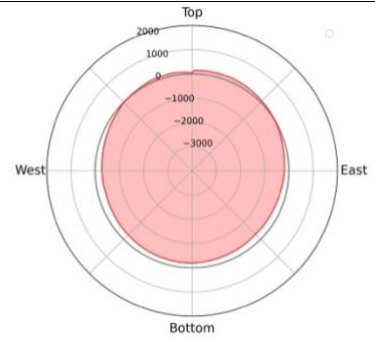
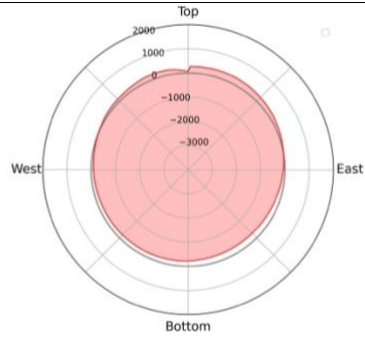
S5



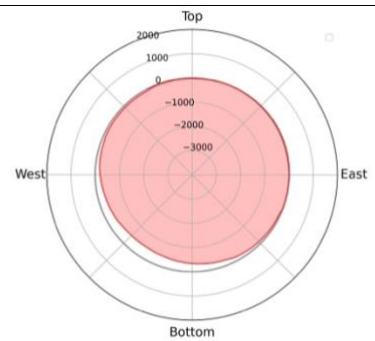
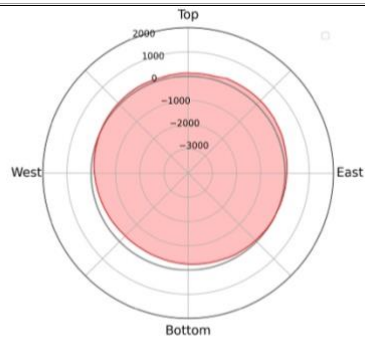
S6



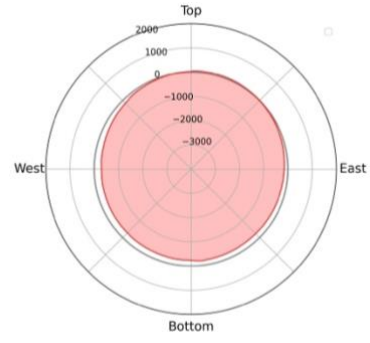
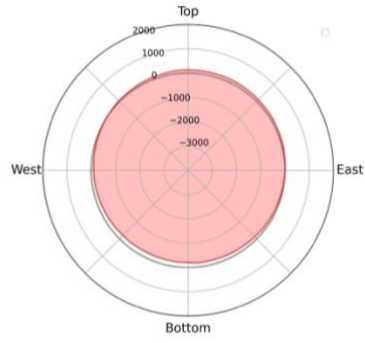
S7



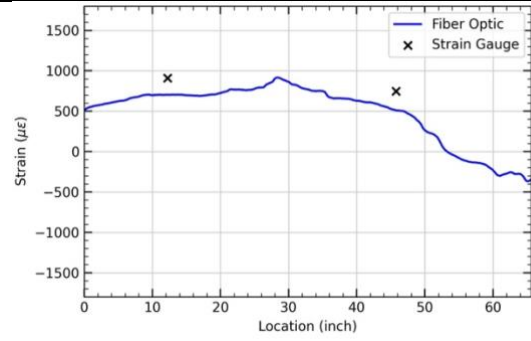
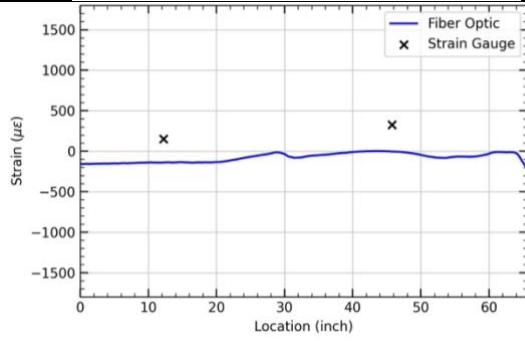
S8



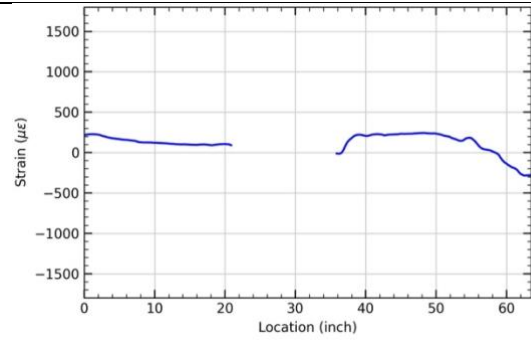
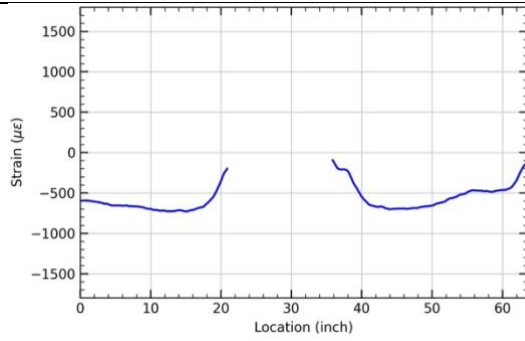
S9



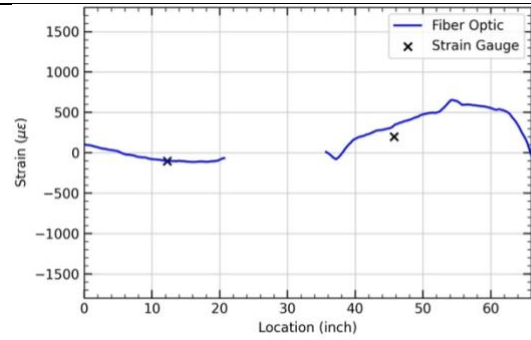
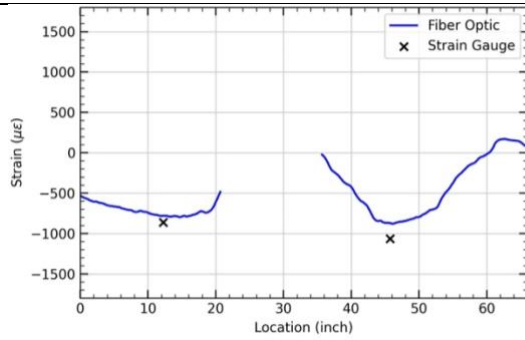
S10



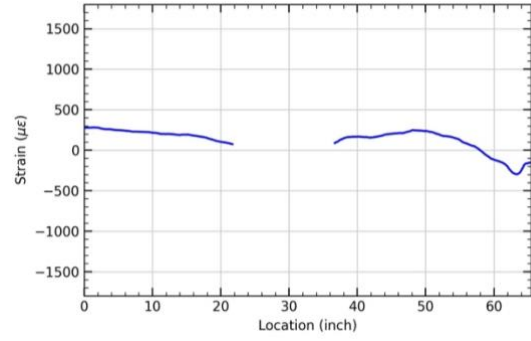
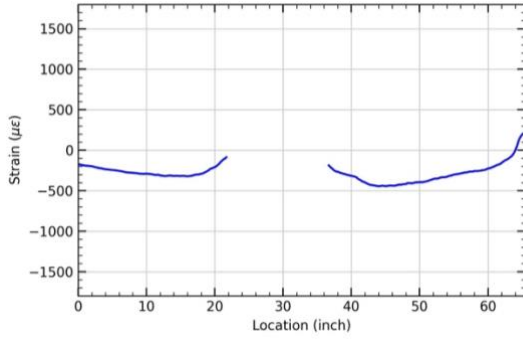
S11



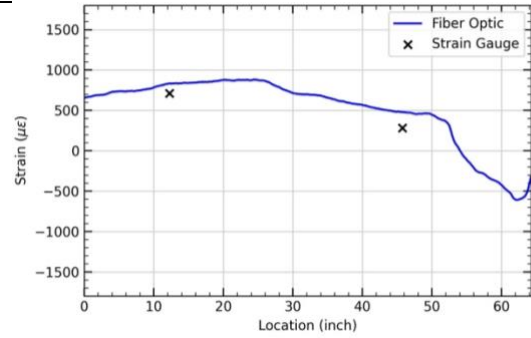
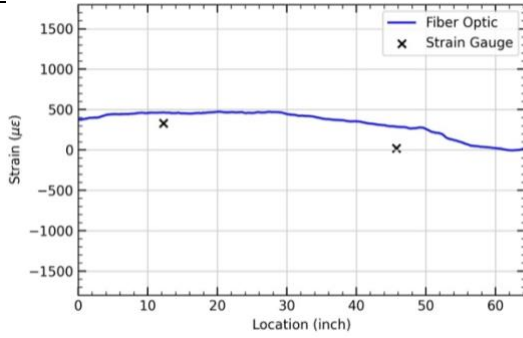
S12



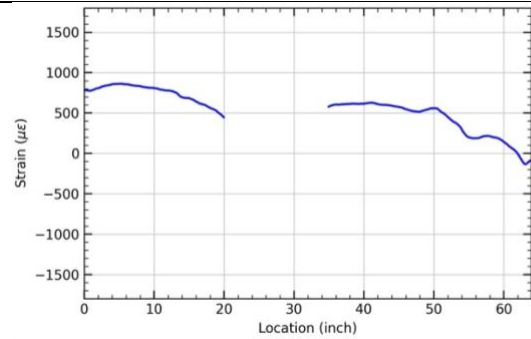
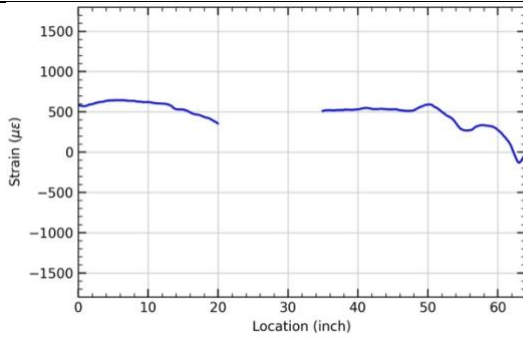
S13



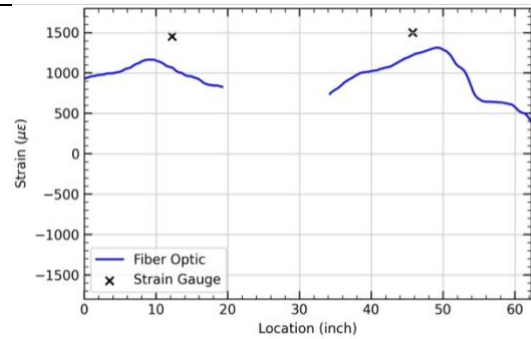
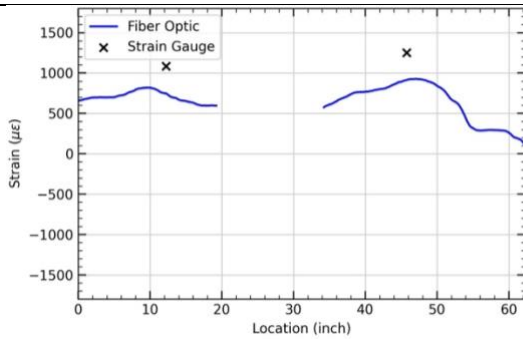
S14



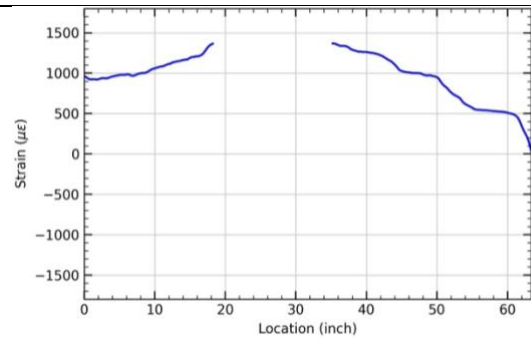
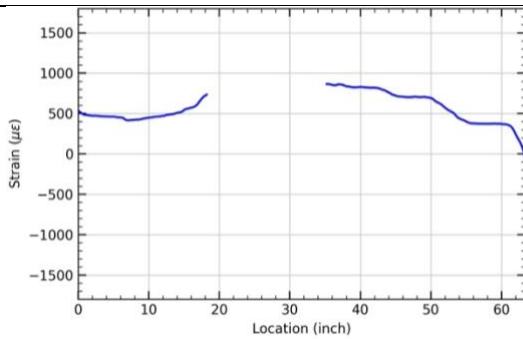
S15



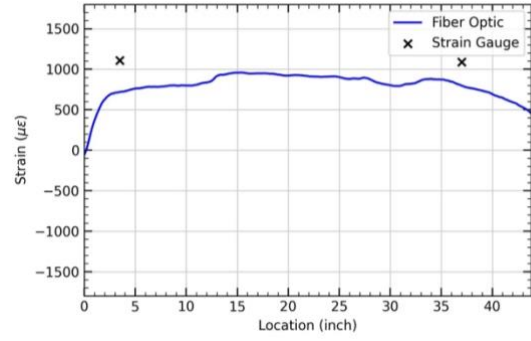
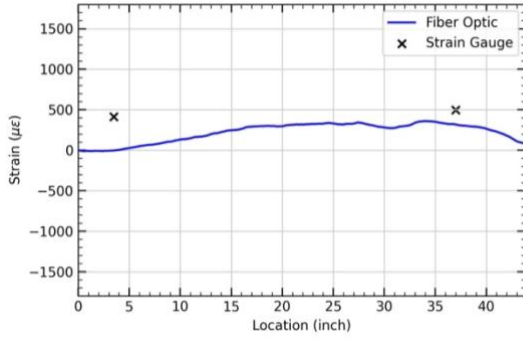
S16



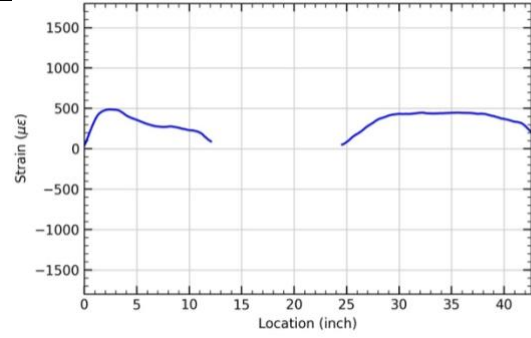
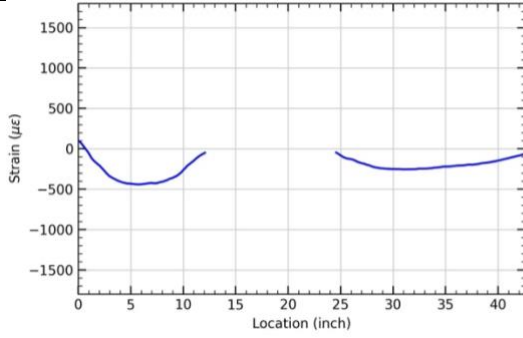
S17



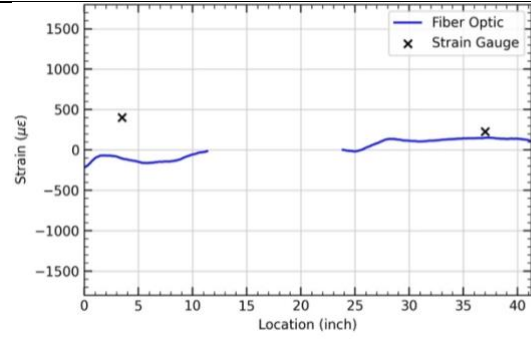
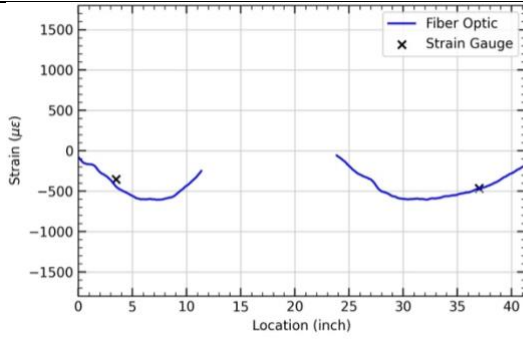
S18



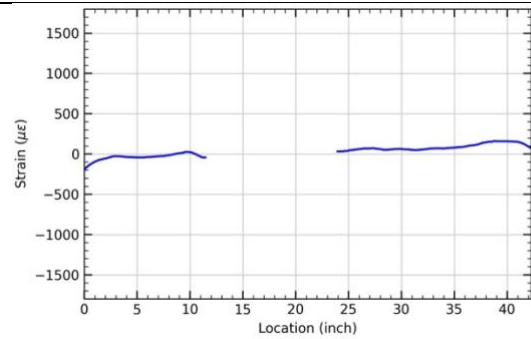
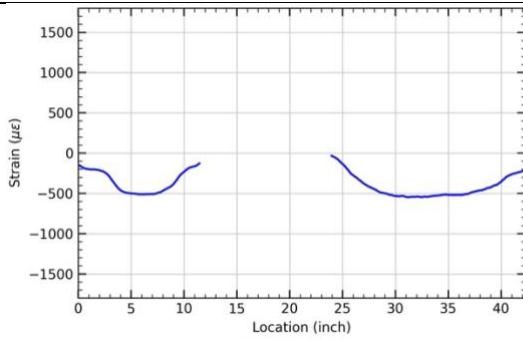
S19



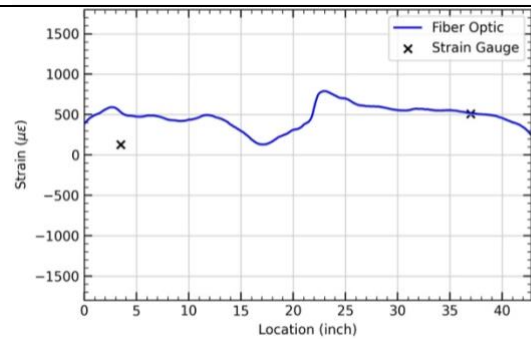
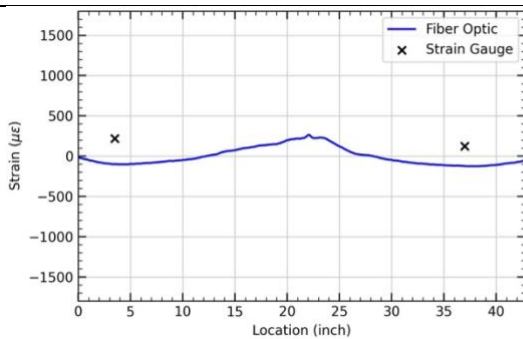
S20



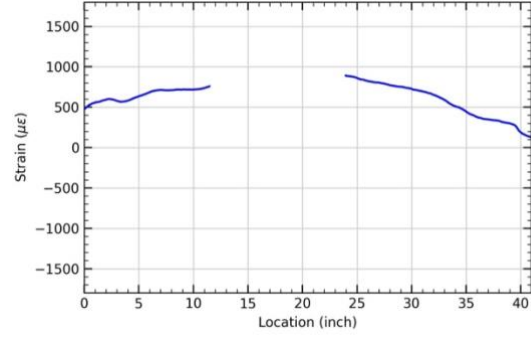
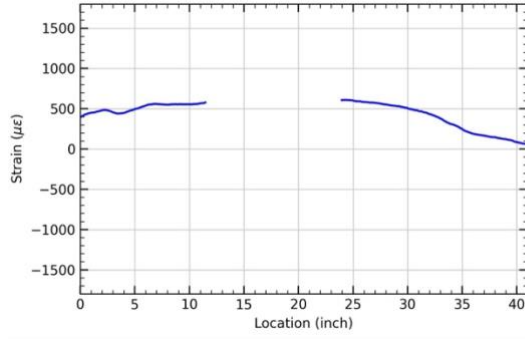
S21



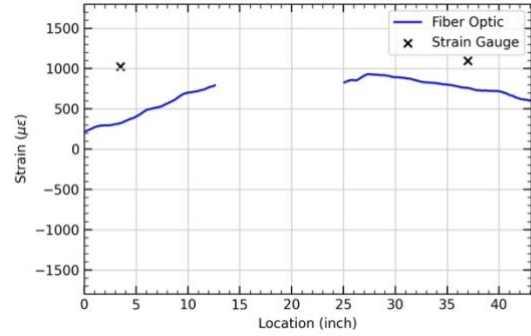
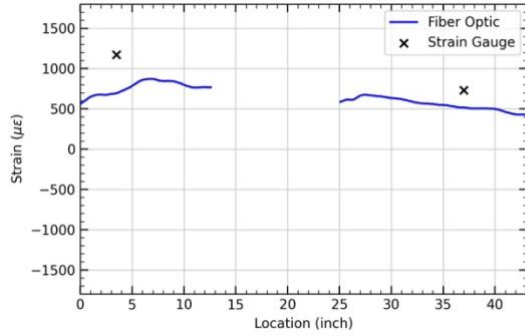
S22



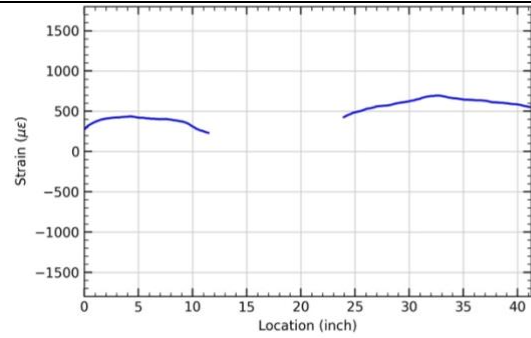
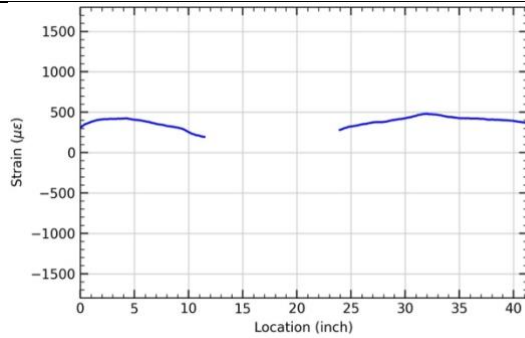
S23



S24



S25



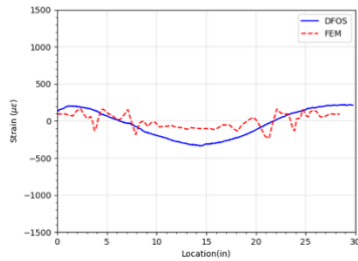
(a) Strain distribution under 8.3-degree rotation condition

(b) Strain distribution under 140 kips axial force condition

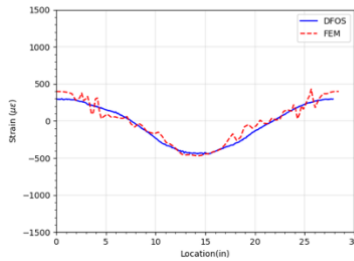
Appendix C: Comparison of FEM simulation results and experimental results

The experimental data were compared to the results from the F.E. model.

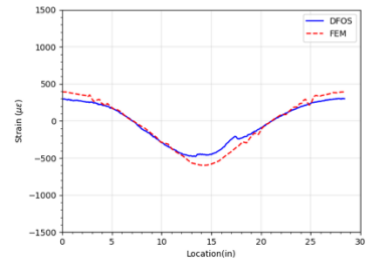
(c) Specimen 1



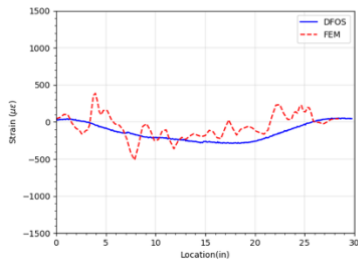
Strain distribution of S1
(push down)



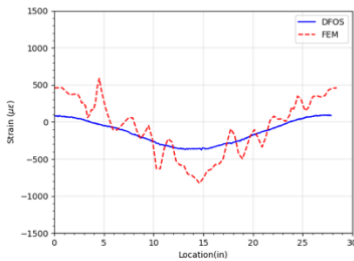
Strain distribution of S2
(push down)



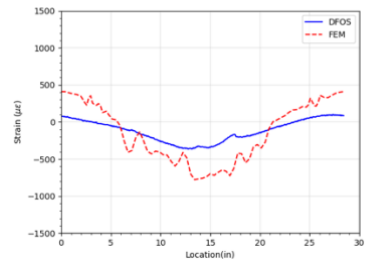
Strain distribution of S3
(push down)



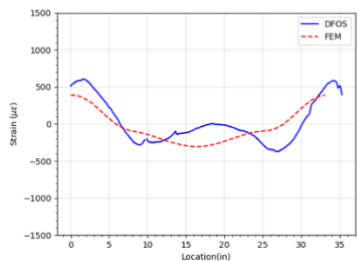
Strain distribution of S1
(pull)



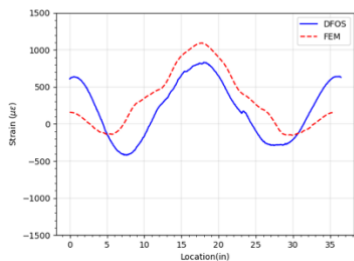
Strain distribution of S2
(pull)



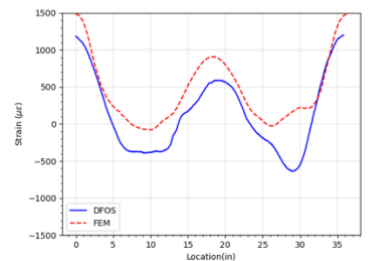
Strain distribution of S3
(pull)



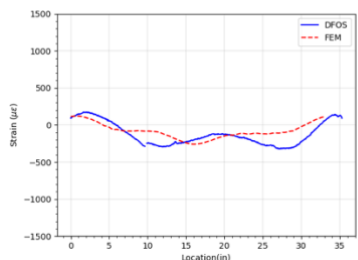
Strain distribution of S4
(push down)



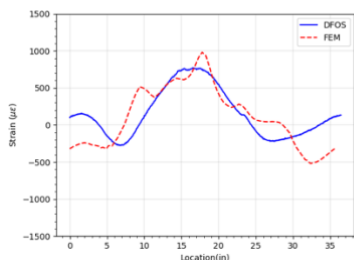
Strain distribution of S5
(push down)



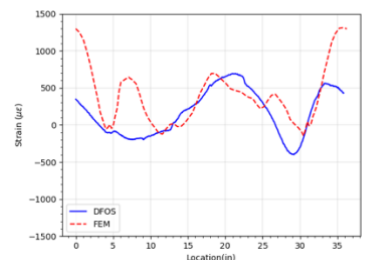
Strain distribution of S6
(push down)



Strain distribution of S4

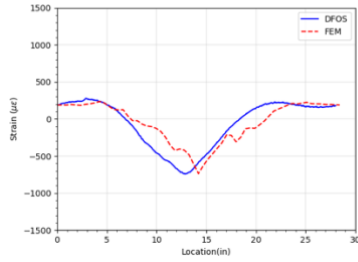


Strain distribution of S5



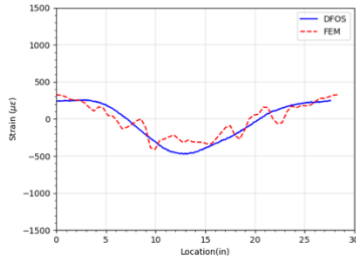
Strain distribution of S6

(pull)



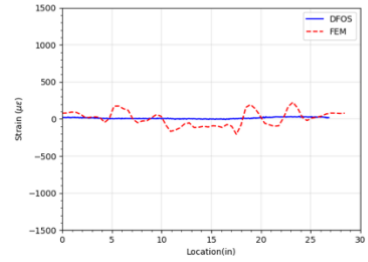
Strain distribution of S7
(push down)

(pull)

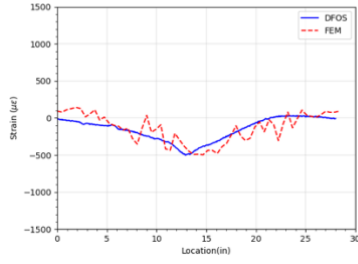


Strain distribution of S8
(push down)

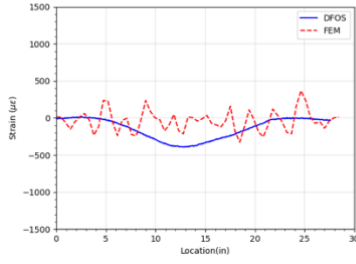
(pull)



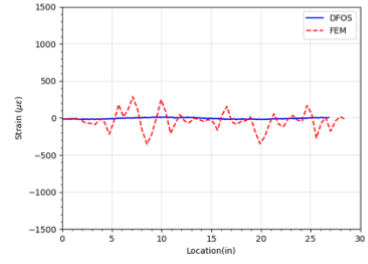
Strain distribution of S9
(push down)



Strain distribution of S7
(pull)

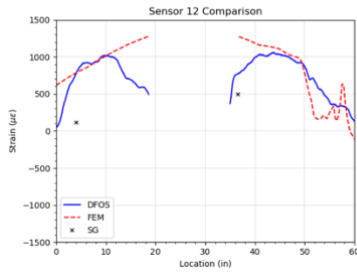


Strain distribution of S8
(pull)

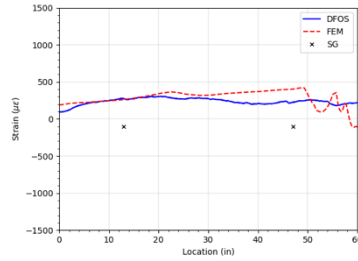


Strain distribution of S9
(pull)

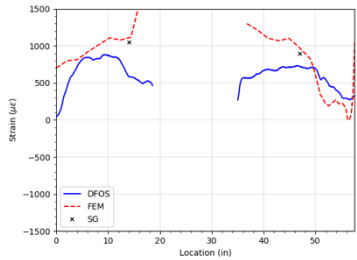
Hoop strain



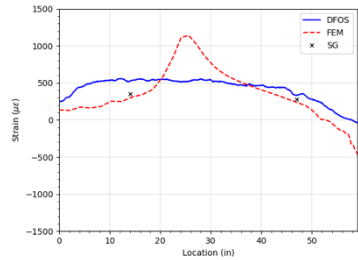
Strain distribution of S12
(push down)



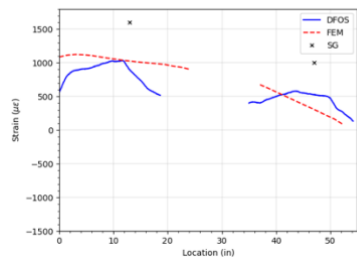
Strain distribution of S13
(push down)



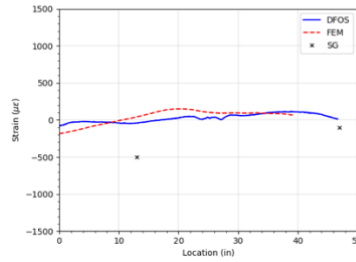
Strain distribution of S12
(pull)



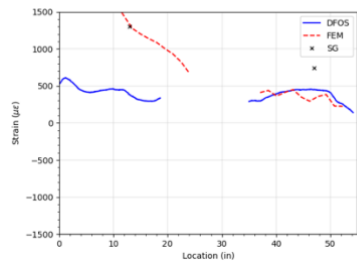
Strain distribution of S13
(pull)



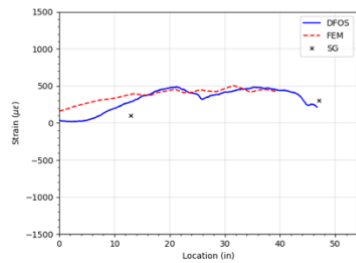
Strain distribution of S16
(push down)



Strain distribution of S15
(push down)



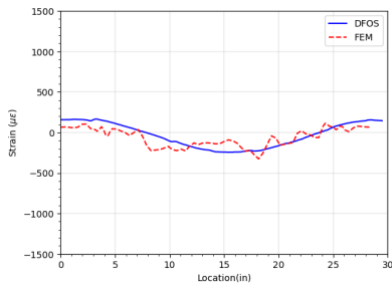
Strain distribution of S16
(pull)



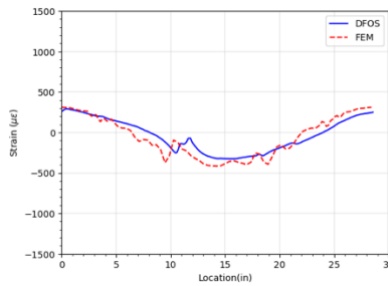
Strain distribution of S15
(pull)

Axial strain

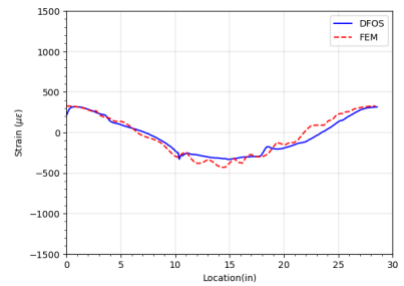
(d) Specimen 2



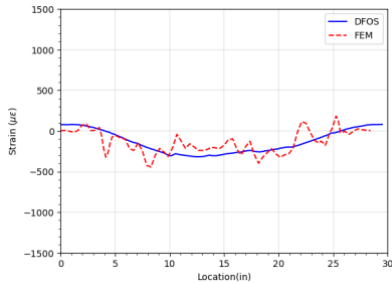
Strain distribution of S1
(push down)



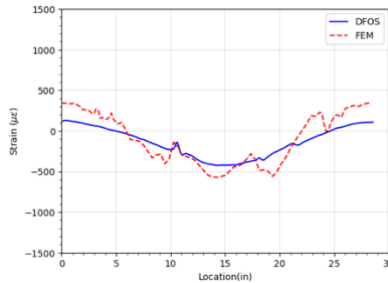
Strain distribution of S2
(push down)



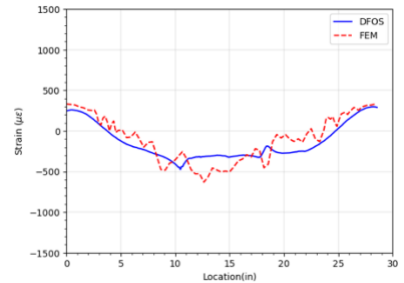
Strain distribution of S3
(push down)



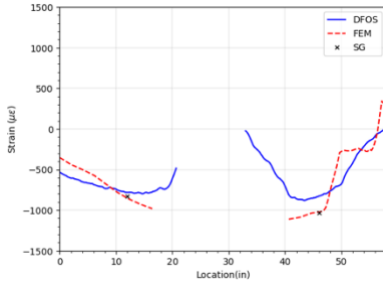
Strain distribution of S1
(pull)



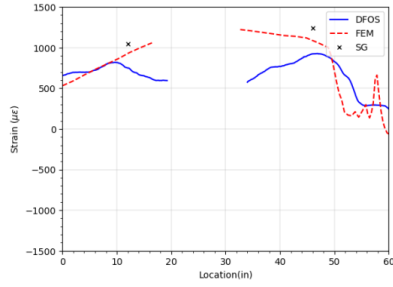
Strain distribution of S2
(pull)



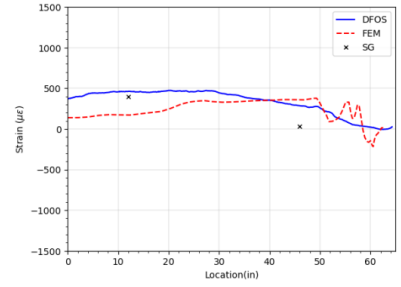
Strain distribution of S3
(pull)



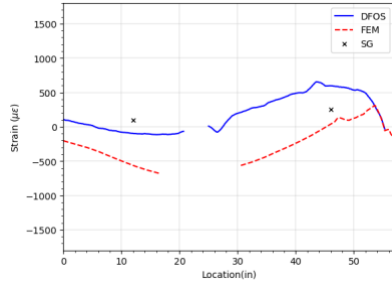
Strain distribution of S10
(push down)



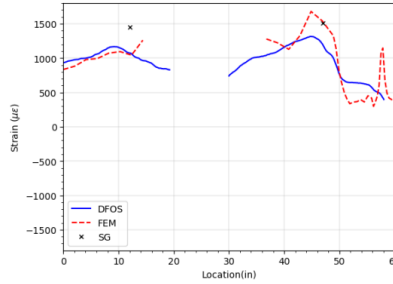
Strain distribution of S12
(push down)



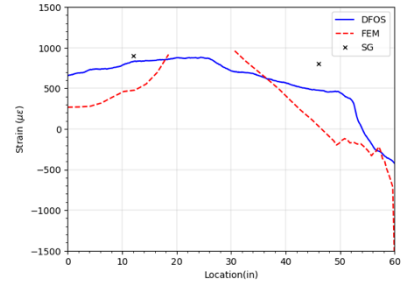
Strain distribution of S13
(push down)



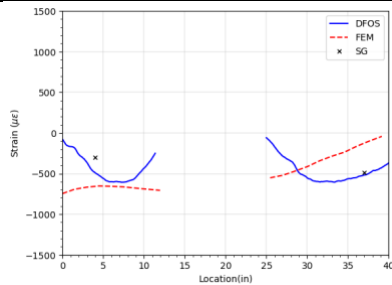
Strain distribution of S10
(pull)



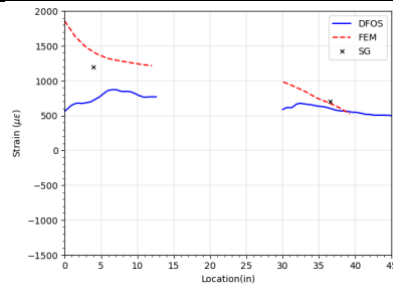
Strain distribution of S12
(pull)



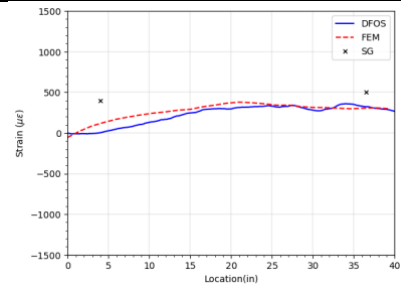
Strain distribution of S13
(pull)



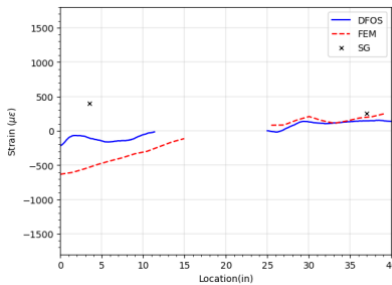
Strain distribution of S14
(push down)



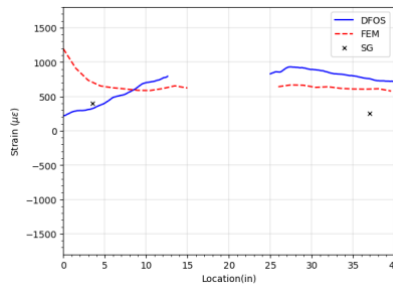
Strain distribution of S16
(push down)



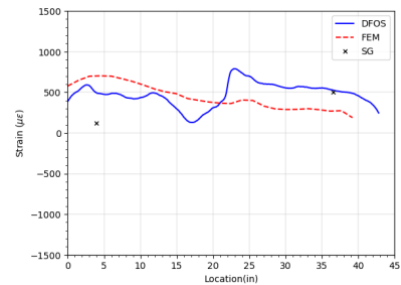
Strain distribution of S15
(push down)



Strain distribution of S14
(pull)



Strain distribution of S16
(pull)



Strain distribution of S15
(pull)

Axial strain